# Surface Water Detection using Sentinel Radar Imagery Compared with Flood modelling: a case study in Townsville, Australia

By

**Phongeun Thammavongsa**

*Thesis*
*Submitted to Flinders University*
*as partial fulfilment for the degree of*

**Master of Geospatial Information Science**

College of Science and Engineering
20 October 2019

# CONTENTS

# LIST OF ABBREVIATIONS

| | |
|---|---|
| AWEI | Automated Water Extraction Index |
| BOA | Bottom of Atmosphere |
| CPs | Control Points |
| DEM | Digital Elevation Model |
| ESA | European Space Agency |
| EW | Extra Wide swath |
| GIS | Geographical Information System |
| GCPs | Ground Control Points |
| GRD | Ground Range Detected |
| HH | Horizontal transmission and Horizontal receive |
| HV | Horizontal transmission and Vertical receive |
| IW | Interferometric Wide swath |
| ISODATA | Iterative Self-Organizing DATA |
| LiDAR | Light Detection And Ranging |
| MNDWI | Modified Normalized Difference Water Index |
| MSI | Multispectral Instrument |
| NIR | Near infrared |
| NN | Nearest Neighbour |
| NDVI | Normalised Difference Vegetation Index |
| NDWI | Normalized Difference Water Index |
| PCA | Principal Component Analysis |
| Radar | Radio Detection And Ranging |

| | |
|---|---|
| RMS | Root Mean Square |
| SLC | Single Look Complex |
| SWAT | Soil and Water Assessment Tool |
| SWIR | Shortwave infrared |
| SD | Standard Deviation |
| SAR | Synthetic Aperture Radar |
| TOA | Top of Atmosphere |
| TWI | Topographic Wetness Index |
| UV | Ultraviolet |
| VH | Vertical transmission and Horizontal receive |
| VV | Vertical transmission and Vertical receive |
| WV | Wave mode |
| WOfS | Water Observation from Space |

# LIST OF EQUATIONS

# LIST OF FIGURES

# LIST OF TABLES

# ABSTRACT

Flooding is a natural disaster that brings about undeniable impacts on the environment and human property. Traditional methods like hydrological and hydraulic models have been developed to provide information regarding flood predictions. The advanced technology of satellite sensors has been used to provide related information to help improve flood predictions, especially in situations of limited ground data. Utilising such technology, this research aimed to explore the usefulness of freely available spaceborne imaging (Sentinel 1 Radar-Radio Detection And Ranging) in providing satellite information that can be compared to flood predictions produced by a hydrological flood model. The research focused on mapping the flood extent that occurred in the urban area of Townsville city, Australia at the end of January to early February 2019, by using both multispectral and Radar images (Sentinel 2 and Sentinel 1 respectively).

The satellite imagery was acquired from Sentinel 1 (C band Synthetic Aperture Radar – SAR) and Sentinel 2 (Multispectral Vis-NIR-MIR wavelengths) which were used for pre-flood (dry state), during and post-flood event (wet states). Pre-processing of the multispectral imagery included geometric and radiometric corrections. Classification of the multispectral images was performed by utilising the Normalised Difference Water Index and a grey scale thresholding. After geometric and radiometric calibration and speckle reduction, the classification of the Radar images was performed using density slicing of the average of VV and VH polarizations, in conjunction with a change detection method.

The overall accuracy of the classification of the two multispectral images, when validated with the map of surface water extent (Landsat Water Observations from Space), was 94.7% and 91.9%, with kappa values of 0.94 and 0.90 (for dry and wet conditions respectively). The overall accuracy of the classification of the Radar image (post-flood event), when validated against the classification of the multispectral image, was 90.0% with a kappa value of 0.87. The qualitative comparison of the classification of flood extent (during flood event) with the map of potential flood depth of Townsville from hydrologic modelling resulted in partial similarities along the river and open water bodies, particularly for areas predicted by the flood modelling to be greater than two metres in depth. The Radar classification showed areas of flooding to the west and north of the area, to which flood modelling was applied. However, differences between the Radar classification and flood modelling were evident in residential areas and these differences are attributed to confusion associated with Radar double bounce from buildings and water, backscatter from objects within the water and from wind-induced rough water surfaces. Longer wavelength SAR, for example, S or L band, could address some of these issues to some extent.

*Keywords: Flood, Flood extent, Radar, Sentinel 1, Sentinel 2, Change detection, Threshold, Polarization.*

# DECLARATION

I, Phongeun Thammavongsa, certify that this thesis does not incorporate without acknowledgment any material previously submitted for a degree or diploma in any university; and that to the best of my knowledge and belief it does not contain any material previously published or written by another person except where due reference is made in the text.

Signature: Date: 20 October 2019

Phongeun Thammavongsa

# ACKNOWLEDGEMENTS

I would like to wholeheartedly express my acknowledgement to all the individuals and institutions who contributed to and supported me throughout my enjoyable yet difficult research period. My highest respect goes to Professor David Bruce at Flinders University whose insights and guidance are precious. I thank him for he is a great supervisor who always shares his valuable knowledge and supports me continuously, not only regarding technical issues but also regarding communication issues. Thank you for always having my back!

With much gratitude, I also thank Dr Margaret Shanafield, a researcher at Flinders University and my supervisor who always provides support. Her words are very cheerful and enlighten me; thereby helping me to complete my work. Thank you for your encouragement. I also wish to express my gratitude to Robert Kean, GIS specialist at Flinders University and my supervisor who always lends a hand to help me solve any technical issues I face. Thank you for sharing your knowledge and advising me to have a day off once a week so that I can always have the energy to work. Thank you both also.

I humbly acknowledge Flinders University for all the student support provided. My appreciation goes to all the staff at Flinders, the International Student Service Team, and the Australian Government: Department of Foreign Affairs and Trade, who always support my study both at Flinders University and outside of the University. Thank you for everything.

Furthermore, I would also like to express my enormous gratitude to my parents who are always by my side, who are my light when there is darkness, who direct me when I was about to get lost, and who always lift me up when I feel like I want to give up. I also thank my sister and my nephew who constantly said something nonsensical but cheerful to make me smile. I love you all.

I would like to thank my beloved PJ who always takes care of me and makes my favourite dishes. Thanks for all your support, encouragement, and listening to me. I would not have come this far without you by my side, especially during those times when I had to stay back late in the lab, during those freezing nights. My love is for you.

Lastly, I would like to express my gratitude to all my friends here and back home who have provided support, encouragement, and who have shared their knowledge along the way during my research. I cannot finish this journey without saying thanks to you all.

# CHAPTER ONE: INTRODUCTION

## 1.1 Problem statement/background

Flooding is recognised as one of the most devastating natural disasters that frequently occurs throughout the world. The characteristics and types of this phenomena that have been variously described in literature, such as flash floods and storm floods, are commonly caused by a number of factors, including excessive rainfall, sea level rises, or dam failures (Few 2003; Kron 2005; Raaijmakers, Krywkow & van der Veen 2008). Globally, the occurrence of flood events is considered to be the most severe disaster regarding its contribution to the impacts on the environment and human property when compared to other types of natural disasters (Adhikari Pradeep et al. 2010). From 1995 to 2015, among all weather-related disasters, (including earthquakes, landslides, droughts, wildfires, and volcanic activity), flooding accounted for 43% of the total number of damage-event occurrences (CRED/UNISDR 2016). Australia, for example, is one of the countries that frequently experiences flood events, especially in Queensland, which is located in a tropical climate zone with low-lying geography along its coastal areas, making it vulnerable to floods (Apan et al. 2010; Coates 1999). Despite the country's development in terms of advanced technology and techniques used for analysing natural disasters, unstoppable disasters such as flooding still have significant regional impacts (Ishikawa et al. 2013; Watson et al. 1998).

The potential effects of flood events have been studied extensively and international organisations have recognised the need to integrate risk reduction strategies into sustainable development frameworks (Pelling et al. 2004). To create proper strategies and management plans to reduce the impacts of flooding events, an understanding of the impacts that will occur under a variety of expected conditions are required. Traditionally, this information has been provided by using hydrological and hydraulic models (Chatterjee, Förster & Bronstert 2008). There are many flood models which have been developed, including commercial, research, or freely available models (Patro et al. 2009). The models similarly require data collection of rainfall, soil data type, topography and temperature. Although some hydrological and hydraulic models may request less data input to run the models, some may require more data input such as infrastructure, structuring, and cadastral data, which poses challenges in terms of data fulfilment (Few 2003; Teng et al. 2017).

In recent decades, several alternative methods have been used to predict flood inundation as well as to provide data for flood models. This includes the combination of additional tools with the models and the use of spaceborne imagery (Houser et al. 1998). Satellite remote sensing can be incorporated into other methods, such as a geographical information system (GIS) tool and flood modelling, to overcome problems related to a lack of data (Houser et al. 1998; Schmugge et al. 2002). Satellite imagery, either optical and/or Radar imagery, can be processed to provide various types of information such as the amount of rainfall, soil moisture, landcover, and flood extent (Horritt,

Mason & Luckman 2001; Schmugge et al. 2002). The latter, especially, can be derived at the time the flood occurs without a requirement for various parameters such as rainfall, soil types, and other topographical data, unlike typical hydrological models. This advantage has proven useful for coupling satellite imagery analysis with hydrological and hydraulic models (Levy et al. 2007).

However, each type of satellite imagery provides both advantages and limitations. Various engineering and environmental limitations are inherent in the different types of satellite images due to their temporal/spatial resolution and their capacity to detect the information during flood events (Schumann et al. 2007; Teng et al. 2017). Optical satellite imagery has been proven to successfully provide reliable flood extent information, but it is useless to extract the flood information from the imagery when there are limitations to the acquisition of data during the night and during poor weather conditions, especially cloudy conditions (Grimaldi et al. 2016). Aerial imagery can provide highly accurate and real-time observations appropriate to the geographically smaller areas. However, using airborne platforms to capture images over large areas can be expensive and also difficult to implement, especially in poor weather conditions such as those often associated with a flood. The aeroplane used to capture the imagery may not be able to fly stably, which can negatively impact the resolution of the imagery (Biggin 1996; Schumann et al. 2011). Microwave Radar and Synthetic Aperture Radar (SAR) imagery have the capacity to detect information no matter the weather conditions or the time, while also providing a faster repeat cycle with a large coverage of surface area (Chini et al. 2019; Grimaldi et al. 2016; Marti et al. 2010). However, uncertainties and limitations when detecting water extent in urban areas are raised in literature (Giordan et al. 2018; Khan et al. 2011). Since countries without access to high-technology models often experience the greatest damage from flooding and also there have not been any universal solutions regarding the use of satellite imagery in cooperation with the models, this thesis explores the possibility of using freely available satellite imagery to understand flood inundation better and it also undertakes a comparison with the predicted flood extent versus flood modelling.

## 1.2 Research aim and objectives

The main aim of this research is to explore the usefulness of freely available spaceborne imaging (Radar Sentinel 1) in providing satellite information that can be compared with flood predictions produced by a hydrological flood model.

Specifically, the objectives of this study are:

- Extract flood water extent using Sentinel satellite products;
- Examine whether the results from Sentinel image processing agree with the results of flood predictions generated by using a flood model at the specific time;
- Provide suggestions regarding the usefulness of the freely available spaceborne imaging Radar for detecting water in urban areas.

## 1.3 Study area

The study area for this research covers two main catchments of the Bohle and Ross Rivers located in Townsville City, one of the largest regional cities in Queensland, Australia. Townsville has an estimated population of 194,072 people (Australian Bureau of Statistics 2019). The location of Townsville is in northern Queensland, approximately 1,300 kilometres north of Brisbane, the state's capital. The surface area of the local government is 3,738 $km^2$. Townsville borders on the Great Dividing Range to the west, the Mount Elliot area (or Bowling Green Bay National Park) to the south, and the Paluma Range to the north. The area is characterised by diverse landforms and ecosystems with several rivers and creeks running through it which supply fresh water to the region. The central area of Townsville is located along the coastal plain, with the Ross and the Bohle being the main rivers (Figure 1).

Townsville is further characterised by a tropical climate, with an average annual rainfall of 1,143 mm over an average of 91 rain days per annum (Bureau of Meteorology 2019a). Most of the average rainfall falls during the wet season from November to April, which is the vulnerable time for storm flooding. The region experiences thunderstorms, monsoonal rainfall, and tropical cyclones, putting the region at risk of flooding, especially flash floods. The city experienced extreme flash floods in January 1998, February 2007, January 2009, December 2010, March 2018, and the latest major flash flood was in February 2019 (City of Townsville 2019b; Townsville Bulletin 2019).

According to its vulnerability to flooding and the development of the city, Townsville city council has launched a detailed study and provided a flooding map service which includes detailed flood depth and flood extent all over the city (Townsville Bulletin 2019). The areas of the flood study have been divided into 23 sub-catchments: Eastern Alligator Creek, Gordon Creek, Horseshoe Bay, Little Bohle, Lower Stuart, North Ward, Ross Creek, Ross River, Upper Bohle Plains, Deeragun, Althaus Creek, Louisa Creek, Lower Bohle, Bluewater, Douglas Annandale, Upper Bohle, Alligator Creek, Middle Bohle, Black River, Captain Creek, Gumlow, CBD, and Inner West End (City of Townsville 2019a).

The extent of the study area (Figure1) focuses on the Bohle and Ross River catchments, with the total study area comprising of 1,230.287 square kilometres where the higher resolution map of the study area can be found in Appendix A. Along the Ross River, there is the Ross River Dam, which was constructed in 1971 to help reduce flooding events and to store water. Downstream of the dam, there are three weirs – Black Weir, Gleeson Weir, and Aplins Weir – which help maintain water within the river (City of Townsville 2019d). It is reported that within these catchments, the historic flood recurrence is lower for the Ross River catchment and higher for the Bohle River catchment. Flooding along the Ross River has mostly been due to overland flows, which have been reduced by the construction of the dam. However, the latest flooding of the city, which was caused by 10 days of consecutive rainfall, resulted in unexpected damage which went beyond the probability and assumptions of the flood study. A number of the low-lying suburbs were reported to be adversely

impacted by flooding, something which was predicted not to happen within the 100-year prediction cycle (ABC News 2019). This particular flood was of interest due to its high impact, including damage to hundreds of houses and public property, and even the loss of life. It was therefore chosen for analysis in the current study.

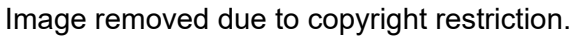


*Figure 1: Geographical location of Ross River and Bohle River catchments in Townsville, Queensland.*

## 1.4 Research questions

To conduct this research, the initial research questions were:

- Do flood prediction maps corresponding to extreme flows agree with the flood extents mapped via satellite imagery?
- How well can Sentinel 1 Radar imagery detect water bodies in the study area?
- What are the differences and similarities between the results from the satellite image analysis and the result of potential inundation from the Townsville Council flood model?

## 1.5 Potential significance of the research

- Providing information about the use of advanced and free sources of information, such as satellite images, to detect water extent in urban areas. This could be significant, especially for countries that have less data to support flood predictions, and where this source of information can offer reliable alternative data to assist with floodwater management;
- Providing flood mapping at low cost;
- Contributing to the management and mitigation of future impacts caused by natural disasters;
- Contributing to the assessment of flood damage, thereby assisting relief organizations.

## 1.6 Outline of the thesis

The aim and objectives of the research will be investigated and presented using the following thesis structure. In chapter two, a review of related literature will address the matters regarding the differences in satellite sensors and their use in generating maps of surface water and flood extent as well as the use of hydrological-hydraulic modelling to produce flood prediction maps. Chapter three will introduce the datasets, software, and methods used to achieve the research aim and objectives. The experimental results of significant processes will be demonstrated in chapter four, whilst chapter five is devoted to the discussion of the results as well as the limitations related to this overall research. Finally, the conclusions and recommendations will be reported in the last chapter.

# CHAPTER TWO: LITERATURE REVIEW

## 2.1 Significance of flooding phenomenon

Flooding is recognised as one of the most devastating natural disasters. This includes storm floods, flash floods, riverine floods, overflow floods, dam break floods, and tsunamis (Few 2003; Hammond et al. 2015; Kron 2005; Teng et al. 2017). Excessive amounts of precipitation during the wet season is the most common cause of flooding, especially in low-lying and monsoonal regions. Such is the case for many countries in Asia including, but not limited to, China, Bangladesh, Indonesia, India, and Laos (Levy et al. 2007).

The increase in the global population has been linked to climate change, including a shift in the seasonal timeline, the environmental-global rainfall pattern, and the intense amount of rainfall which sometimes not only brings about flooding events but also droughts in some areas (Few 2003; Kron 2005). Apart from influences on the natural environment, the increase in population also causes new urban development, thus impacting the hydrological cycle, and changing water flow and storage patterns (Hammond et al. 2015; Kron 2005). Floodplains and impervious urban areas are especially vulnerable to flooding when prolonged rainfall occurs (Hammond et al. 2015).

Although flooding is a part of the natural hydrological cycle of river systems and it can provide both ecological and anthropogenic benefits, particularly in terms of alleviating drought conditions (Teng et al. 2017), flooding can also impact cultural, economic, ecological, educational, and/or human life, no matter how minimal or severe the size of the flood is (Godschalk 2003; Levy et al. 2007). A 2001 review of the global loss of human life which can be directly contributed to flooding showed that there were 25,000 human deaths with billions of US dollars in economic losses (Godschalk 2003). Severe cases of flooding – such as that caused by hurricanes or tropical monsoonal storms, mudslides, violent winds, and lightning – can lead to additional short or long term destruction (Few 2003).

Since it is undeniable that flooding contributes to losses, and because floods have become more frequent and intense in recent decades, engineering and technical sectors have been pushed to study the phenomenon and provide predictions of flood extents, flood levels and the velocity of water flows (Levy et al. 2007; Patro et al. 2009; Zhu, Zhenduo et al. 2016). However, one of the most difficult challenges to provide an accurate prediction is related to a lack of data as well as the cost of data acquisition. Hence, various hydrological models have been developed and combined with the use of satellite imagery, to generate flood extents in near-real-time and aid in the reliability of information about flooding (Levy et al. 2007; Quirogaa et al. 2016).

## 2.2 Remote sensing sensor

The mode of sensors used (Figure 2), such as passive (multispectral sensor) and active (Radar: Radio Detection And Ranging; and LiDAR: Light Detection And Ranging), play a pivotal role in deriving information from the Earth's surface. Since the sensors function via measuring electromagnetic radiation, different sensors exhibit information in different ways.

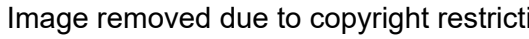


*Figure 2: Electromagnetic Radiation and its relation to passive and active remote sensors.* (Muller 2017).

### 2.2.1 Passive remote sensor

The sun is the main source of energy for passive sensors, which means that the sensor does not have its own source of energy. Most passive sensors use solar radiation to illuminate the object (Campbell & Wynne 2011). Most of the time, the sensor detects objects based on the electromagnetic wavelength which ranges from ultraviolet (UV) through visible wavelengths to near-infrared (NIR) and sometimes to thermal infrared. The spectral resolution of the imagery accounts for how many bands there are as well as the width of the wavelength each band senses (Boettinger et al. 2008). For example, the QuickBird sensor system provides three visible bands (red, green, blue) and near-infrared centred at 485 nm (450 to 520 nm), 560 nm (520 to 600 nm), 660 nm (630 to 690 nm), and 775 nm (760 to 790 nm), which can be used for shallow water applications (Mishra et al. 2006). Spectral resolution is closely linked to spatial resolution in an inverse way where, in general, the higher the spectral resolution, the lower the spatial resolution. The spatial resolution of spaceborne instruments varies from sensor to sensor, ranging from less than a metre to a kilometre in length. In the case of temporal resolution, passive sensors can provide information about land surface with relatively high repeat times from multiple weeks to daily (Table 1). Together with these various resolutions and the uniqueness of the Earth's surface-reflectance of different land cover types (Figure 3), passive remote sensing is widely used in a number of applications including surface water mapping, land use cover mapping, environmental disaster mapping like landslides, and forest fire mapping.

| Satellite sensors | Spectral Bands | Central wavelength (µm) | Spatial resolution (m) | Temporal resolution (day) |
|---|---|---|---|---|
| MODIS | B1-B2<br>B3-B7 | 0.645; 0.858<br>0.469; 0.555; 1.240; 1.640; 2.130 | 250<br>500 | Daily |
| Landsat 8 | Pan<br>B1-B7, B9<br><br>B10-B11 (TIR) | 0.590<br>0.440;0.480;0.560;0.655;0.865;1.610; 2.150; 1.37<br>10.895; 12.005 | 15<br>30<br>100 | 16 |
| SPOT 6 | Pan<br>B1-B3<br>SW-IR | 0.600<br>0.490; 0.560; 0.660<br>0.825 | 2.5 or 5<br>10<br>20 | 26 |
| Sentinel 2 | B1, B9, B10<br>B2-B4, B8<br>B5-B7, B8A, B11, B12 | 0.443; 0.945; 1.375<br>0.490; 0.560; 0.665; 0.842<br>0.705; 0.740; 0.783; 0.865<br>1.610; 2.190 | 60<br>10<br>20 | 5 |
| Ikonos 2 | Pan<br>B1-B4 | 0.727<br>0.485; 0.560; 0.660; 0.830 | 0.82<br>3.2 | 3 |
| PLANETSCOPE | B1-B4 | 0.485; 0.545; 0.630; 0.820 | 3 | Daily |
| Quickbird | Pan<br>B1-B4 | 0.675<br>0.485; 0.560; 0.660; 0.830 | 0.61<br>2.44 | 1-3.5 |
| World view 1 | Pan<br>B1-B4 | 0.625<br>0.455; 0.545; 0.672; 0.850 | 0.31<br>1.24 | < 1 |

*Table 1: Basic characteristics of different sensors.*

Where B means Band, Pan means Panchromatic, SWIR means shortwave infrared. TIR means Thermal infrared. Modified from https://www.satimagingcorp.com/satellite-sensors/ (Boettinger et al. 2008; Muinonen 2018; Team 2018).

Image removed due to copyright restriction.

*Figure 3: Generic spectral signature of soil, vegetation, and water with overlaying spectral bands from LANDSAT 7.*

(Dianderas, Rojas & Kemper 2014)

### 2.2.2 Active remote sensor

Active remote sensors, such as Radar imagery in particular, work differently from passive remote sensors in that they produce their own energy to illuminate objects on the Earth and, hence, they can operate day and night (Campbell & Wynne 2011). Although the active sensor can function in UV, visible and infrared wavelengths, Radar mainly focuses its function within Microwave wavelengths (Figure 2). These latter wavelengths are utilised in the Synthetic Aperture Radar (SAR) sensors that generate multipurpose radar images. Commonly, the sensor will create surface illumination by sending a wavelength within the electromagnetic spectrum to a target and then measuring the energy that returns to the sensor, which is called the backscatter. The sensor is characterised by two main components including the polarisation modes and the band frequency functioning in the sensor. The polarisation modes refer to the direction of the vibration of the electoral component of the radiation of either the transmitted or the received signal and these are common in the vertical or horizontal directions (Joseph 2005). Some SAR sensors offer results which are presented as like-polarisation, others as cross-polarisation, and others again as quad-polarisation. Like-polarisation includes either vertical transmission and vertical receive (VV) or horizontal transmission and horizontal receive (HH). Cross-polarisation is represented in either vertical transmission and horizontal receive (VH) or vice versa (HV). With different polarisations, significant information about the various properties of objects on the Earth's surface can be derived in different ways (Van Zyl, Zebker & Elachi 1987). The band frequency used in active sensors varies depending on the sensor and the band ranges (Table 2). Normally, the band range demonstrates the ability of the wavelength to penetrate through cloud and other obstacles like tree canopies and dry snow.

Radar wavelengths range from 0.75 cm to 130 cm with the latter, the longest wavelength, indicating the greatest penetration (Figure 4).

| Radar Bands | Frequency Range (GHz) | Corresponding Wavelength Range (cm) |
|---|---|---|
| P | 0.230-1 | 30-130 |
| L | 1-2 | 15-30 |
| S | 2-4 | 7.5-15 |
| C | 4-8 | 3.75-7.5 |
| X | 8-12.5 | 2.40-3.75 |
| Ku | 12.5-18 | 1.67-2.40 |
| K | 18-26.5 | 1.13-1.67 |
| Ka | 26.5-40 | 0.75-1.13 |

*Table 2: SAR Radar Frequency Bands.*

Source:https://www.usgs.gov/media/images/definition-sar-radar-frequency-bands-evans-1995.

Image removed due to copyright restriction.

*Figure 4: Different backscatters of short and long Radar wavelengths from various surface objects under different conditions.*

(Schumann et al. 2007).

## 2.3 Remote sensing for urban flood detection

Satellite images have been used extensively to provide information to calibrate, improve, and constrain some parameters in hydrological and hydraulic models (Barneveld et al. 2008; Bates 2012;

Mason et al. 2008). In terms of hydrological variables, satellite observations from optical, multispectral and SAR sensors can contribute important input such as soil moisture, precipitation, land cover mapping, and mapping water extent as well as water levels when it is used in conjunction with the Digital Elevation Model (DEM) (Alsdorf, Rodríguez & Lettenmaier 2007; Anderson 1976; Rast, Johannessen & Mauser 2014). Both active and passive satellite platforms, as well as the sensors, have been improved over time. This has led to higher resolutions both temporally and spatially, particularly with regard to the latter. However, there are advantages and limitations in the uses of each data type and, hence, many researchers have combined the use of optical/multispectral imagery with SAR imagery in order to bridge these limitations and also to provide better results (Markert et al. 2018).

## 2.4 Optical imagery for surface water detection

Optical/multispectral imagery is recognised as a powerful data source to extract land cover and water extent due to its high spatial resolution, and it is best suited to visual interpretation (Giordan et al. 2018). Because most sensors operate in the visible and NIR wavelengths, approximately from 400 to 700 nm and 720 to 950 nm respectively (Joseph 2005), this makes it easy for the users to visually interpret the objects in the images. Moreover, the imagery is accessible via several sources including Landsat and Sentinel mission with a spatial resolution at the 10-30 m level. Therefore, optical imagery is widely used. However, because of its reliance on light from the sun to illuminate the objects on the Earth, the constraint of optical/multispectral imagery used for specific events like flooding is mostly caused by cloud and the time of acquisition, particularly when the flood occurs at night (Drusch et al. 2012; Loveland & Dwyer 2012). Aside from optical/multispectral imagery derived from satellites, images derived from airborne platforms have now become recognised as the best remote sensing imagery available as they provide accurate high-resolution and real-time information, which can also be used as a validation for satellite image classifications (Mason et al. 2008; Musa, Popescu & Mynett 2015). However, this source of imagery experiences drawbacks when applied to large land areas due to the cost of flight, technical issues and weather-related issues, particularly when dealing with storm-induced flood events. Furthermore, when users require updates about the extent of flooding, the cost of flying to retrieve this information increases proportionately whilst the cost for images from an orbiting satellite generally remains stable.

Regarding the mapping of flood extents, research has demonstrated the successfulness of mapping surface water using multispectral imagery (Notti et al. 2018; Pekel et al. 2016). Feyisa et al (2014) present a new automated method to detect water and improve the accuracy of surface water mapping. The research used Landsat 5 TM images as the data source together with the Automated Water Extraction Index (AWEI). This method was developed to yield a better contrast between water and other dark objects like asphalt. Unlike the Normalized Difference Water Index (NDWI) where only two bands are used, this method uses all related bands like blue, green, near-infrared, and

shortwave infrared bands, as well as adding and applying different coefficients (Feyisa et al. 2014). The AWEI is an effective tool for the detection of water bodies, especially with regard to minimising the ambiguity of water versus other dark surfaces such as shadow, for example. However, since AWEI does not consider or factor in differences about the volume of water in different seasons or varying atmospheric compositions, this might result in over-classification for some surface areas. Although other methods like supervised classification, Normalised Difference Vegetation Index (NDVI), Normalized Difference Water Index (NDWI), and Modified Normalized Difference Water Index (MNDWI) have been widely proposed through literature as having high degrees of accuracy (especially the latter) (Du et al. 2016; Lu, D & Weng 2007; Lu, S et al. 2011; Yang et al. 2017), it has not been proven that these methods can be applied uniquely to every region. Since water-related index-based methods rely upon only two main bands in their algorithms (green and either near-infrared or shortwave infrared), the other bands are ignored. With imagery that offers a few or several different bands, there will not be any such complications. However, with multispectral imagery that caters to two or three bands in closed wavelengths like the Advanced Land Imager where there are two NIR bands and three Shortwave infrared (SWIR) bands, selecting the optimal water-related bands is vital and this can contribute to greater accuracy in the classification of objects or flooding (Li et al. 2013).. Although using only water-related index methods can be challenging to delineate water from non-water, water-related index methods are still accepted as the most common approach to classifying water from non-water objects.

## 2.5 Radar for urban flood detection

Although water extent acquired from optical imagery, either airborne or spaceborne, has been proven to be successful, it experiences limitations when mapping water extent during flood events and, thus, SAR imagery has been used extensively for mapping flood extent (Liu et al. 2019; Musa, Popescu & Mynett 2015; Ouled et al. 2018). Despite the advanced nature of its penetration capacity and its lack of time limitations, some research has presented a limitation in the use of SAR imagery. Hence, considerations of sensor characteristics like spatial resolution, wavelength, polarisation, incidence angle, the availability of the imagery at the time needed, methodology and algorithm to extract information are all significant factors to consider.

When dealing with flooding, a selection of Radar wavelength is particularly significant. L band is claimed to be less sensitive to the roughness of the water's surface plus it has the ability to penetrate tree canopies, while C and X bands are deemed to provide less penetration of tree canopies and even precipitation in the air (Liu et al. 2019; Xue et al. 2008). Above all, P band, which is the longest wavelength, presents the greatest penetration through tree canopies and even small branches, with the only detected matter being the trunks of the trees (Santos et al. 2003). S band (as used by NovaSAR1, for example) is another advanced SAR band that can perform better in severe weather conditions like heavy rainfall. It penetrates better down to the ground level when compared to X and

C bands (Dutch 2019). However, in comparison to X, C, and L bands, S band is still less common in the field of using spaceborne Radar for flood detection. With regard to the associated factors of this technology, such as advances in, the limitations of, and the availability (that is, cost, time, and resolution) of optical versus SAR satellite images, the free source of Sentinel 1 SAR imagery at C band wavelength is currently being used more broadly and has been providing reliable results (Giordan et al. 2018; Marti et al. 2010; Twele et al. 2016; Westerhoff et al. 2013).

Various techniques have been applied to mapping water and non-water objects using SAR imagery, which have proven suitable for detecting water extent. Histogram thresholding is one of the common methods that is used to classify water from other objects (Pun 1980). When applying the condition that the image is derived on a non-windy day, water bodies will appear as smooth surfaces with low backscatter to the sensor, thereby appearing as dark tones in the image. Under such conditions, the image will present high distinctions between smooth objects versus rough objects, which aids in yielding better results (Pun 1980). However, the fact remains that mapping water extent during flood events is nearly always faced with challenges like heavy rainfall and windy conditions, which causes surface roughness and this, in turn, contributes to misclassifications (Henry et al. 2006; Pierdicca, Pulvirenti & Chini 2018).

To overcome this ambiguity of water classification from SAR images, the use of multipolarisation has been considered. The different polarisations of HH, HV, and VV derived from Envisat ASAR images, combined together with threshold techniques, was used by Henry et al. (2006) to detect flooded areas and these demonstrated the influence of the polarisation mode on extracting flood extent, where HH polarization produced better results compared to the other two polarisation modes. Together with threshold techniques, change detection is also used to delineate flood extent (Long, Fatoyinbo & Policelli 2014). A method like thresholding imagery can be applied with a single image to detect rough objects. However, by applying a change detection method, multitemporal imagery provides better detection and comparisons in the change of water extent over time – especially before, during and after flooding (Clement, Kilsby & Moore 2018; Long, Fatoyinbo & Policelli 2014).

Although thresholding and change detection methods are commonly used in combination with one another to provide flood extent maps, different methods like image segmentation using a pixel-based method and a statistical active contour model have been applied with European Remote Sensing Satellite SAR (ERS-1 SAR) to map flooding of the River Thames in the United Kingdom (Horritt, Mason & Luckman 2001; Martinis, Twele & Voigt 2009). This method provides a successful result of detecting flood extent in rural areas, but it proves less effective when applied to urban flood conditions due to the complexity of the vertical structures as well as the other effects of invisible flood under the Radar layover and shadow (Mason et al. 2008). To increase the effectiveness and accuracy of mapping flood extent using SAR images, particularly in heterogeneous environments, other topographical data like high-resolution Digital Elevation Model (DEM) and land use land cover

map have been integrated (Matgen et al. 2007). By integrating high-precision topographical data, it has been proven that the classification from SAR images can produce a realistic flood extent, especially with near-real-time events (Brivio et al. 2002; Matgen et al. 2007). Although there are a number of challenges and uncertainties for using SAR imagery in detecting flood extent, there are several methods that have been developed so that errors can be reduced and the accuracy of classification can be improved (Musa, Popescu & Mynett 2015).

## 2.6 Hydrological and hydraulic modelling for urban flood mapping

A hydrological model is an approximation of the real-world hydrological cycle to make it easy to understand, predict, and manage the resources, flow, and even the quality of the water (Moradkhani & Sorooshian 2009; Wheater, Sorooshian & Sharma 2007). The concept of the hydrology is a study about all kinds of aspects related to water on the Earth, whether it be its occurrence, circulation, distribution, or interaction with the environment (Devia, Ganasri & Dwarakish 2015). Hence, there are many types of models that are used for different purposes, including conceptual, analytical, statistical, and numerical models (Devia, Ganasri & Dwarakish 2015; Jain & Singh 2003). These models are mainly applied for studying system behaviour as well as hydrological processes.

In general, to run a hydrological model there is a parameter requirement, with different models requiring different set parameters. There is some obvious data that is used as the input for almost all models such as rainfall, drainage area, landcover, air temperature, soil characteristics, soil moisture content, topography, vegetation, hydrogeology, and other such physical parameters (Devia, Ganasri & Dwarakish 2015). The requirement for a large amount of data input contributes to arising uncertainties and difficulties due to the lack of available data in some instances (Few 2003; Teng et al. 2017). The greatest uncertainty is generally in the quantity of the floodwater and the water extent, particularly in urban areas (Brown, Spencer & Moeller 2007; Jung & Merwade 2011).

Due to the lack of input data or uncertainties regarding the input data, the reliability of the hydrological models is widely studied (Kauffeldt et al. 2016). However, it is not only the parameters that have been questioned but also the structure and the model tools. In general, when applying a hydrological model over a large scale of catchments together with a relatively broad range of time, the complexity is always significant and hence, calibration and parameter optimisation are vital (Yu et al. 2015).

There are several hydrological modelling tools available and selecting the most appropriate tools are always a challenge. This requires the user identify the appropriate tool which matches the requirements of the project together with the tool's capacity, the equation used as well as the availability of input data. The Soil and Water Assessment Tool (SWAT) model, for example, is a complex physical-based model which requires numerical input data including daily precipitation, air temperature, solar radiation, humidity value, wind speed, and a specific water balance equation to simulate the hydrological circulation (Arnold et al. 2012). Various other complex physical-based

models range from the scale of the work to the purpose of the work. Models like SWAT simulate the flow of surface water and the transport process on a catchment scale (Abbaspour et al. 2007). This demonstrates a challenge in the use of the hydrological model.

Besides hydrological modelling, a comprehensive flood assessment requires a combination of hydraulic models. The combined application of hydrological and hydraulic models will allow analysists to conduct in-depth evaluation regarding the impacts of various flood scenarios (Grimaldi et al. 2016). MIKE Flood modelling, for example, has been developed for both river and floodplain modelling to analyse the behaviour of flooding and to identify the causes and effects of flooding while also providing a simulation of flood extent (Chatterjee, Förster & Bronstert 2008). This model has been applied to obtain simulations of flood extents, flood depths, and any other hydraulic-related matters in a number of studies such as a delta region in India and along the Elbe River in Germany (Chatterjee, Förster & Bronstert 2008; Patro et al. 2009). These studies presented a relatively satisfying result of the model in comparison to the observed data. However, other research reveals its limitations in terms of accuracy, time, and cost-effectiveness when compared with alternative models (Jamali et al. 2018). Different models have their own advantages and limitations either because of the systematic nature of the software, the requirement of data inputted, the uncertainty of the data inputted or the results outputted. Hence, additional tools and the use of information derived from satellite images are integrated with the models (Houser et al. 1998).

## 2.7 Townsville flooding Models

Townsville city's council has been undertaking a flood study for catchments throughout the council area. The studies are implemented under a city-wide Flood Constraints Project which aims to develop and provide up-to-date flood models for the city. The models have been developed from a number of previous hydrological and hydraulic studies (City of Townsville 2019b). For the studies, a comprehensive flood assessment of each catchment in Townsville is developed using MIKE FLOOD – a single-package, commercial model that was developed from Mike 11 and Mike 21 by the Danish Hydraulic Institute (Patro et al. 2009). MIKE 11 is a one-dimensional hydrological model which is used to analyse floods, the contribution of dams, water quality, sediment transport, reservoirs, river structure operations, and catchment characteristics (MIKE11 2015). MIKE 21, however, is a two-dimensional model applied for simulating hydraulics and other related events, proving especially practical for estuaries, coastal waters and seas (Warren & Bach 1992). MIKE 11 and MIKE 21 include information about floodplains such as elevation, precipitation, and Manning's n values.

MIKE FLOOD has been used for a recent flood study in the Townsville city council area. Specifically, the Ross and Bohle catchments, whose boundaries cover the city areas, were modelled using data that included historical rainfall records, stream gauging records, topographical data, cadastral data, and structure design data. The model was calibrated to three flood events which occurred in February 2007, January 2009, and December 2010. The Hydrologic Engineering Centre's River

Analysis System (HEC-RAS) was utilised for validating Townsville area's MIKE FLOOD Model's treatment of significant bridge structures. HEC-RAS is free hydrological software that has been widely used for simulating one-dimensional steady and unsteady river flow hydraulics and sediment transportation, calculating the water surface profile, and producing flood inundation maps (Brunner 2010; Buffin-Bélanger et al. 2015; D'Oria, Mignosa & Tanda 2015; Pearson & Pizzuto 2015). From the results of the verification, a reliable agreement between the two models was confirmed. Flood results from the hydraulic model contributed to base-line flood maps for the Townsville city council area, where the maps include water depths, flood levels, and flow velocities of two to 2,000-year average reoccurrence intervals (City of Townsville 2019b).

## 2.8 Summary

In summary, both optical and Radar satellite imagery are possible candidates for mapping water bodies as well as yielding water extent data, which can be compared to provide better information for flood prediction maps. Hydrological and hydraulic models are the most common methods of generating flood extent and flood depth prediction maps, but with the requirement of physical and actual measurements for simulation. Optical images provide promising results to map water bodies using water-related spectral bands. However, the poor weather and cloudy conditions which typically occur during most flood events often obstruct the usefulness of optical images. Since Radar sensors can penetrate through cloud and provide imagery during times of flooding, Radar images are recommended to avoid weather-related issues. While long wavelength SAR imagery can potentially provide better penetration through vertical features such as tree canopies, they are currently expensive and are sometimes not available at the time when a flood occurs. Hence, with a focus on the free and available satellite images as well as non-complex image processing methods, water-related histogram thresholding will be applied to extract flood extent data from Sentinel products for the urban area. These results will be compared to flood models so that the usefulness of the freely available Sentinel products in providing flood extent maps will be realised.

# CHAPTER THREE: DATA COLLECTION AND METHOD

Figure 5 demonstrates the overall workflow of the methods applied in this thesis. First, all data was obtained from various sources, including rainfall, GIS format of drainage sub-basins in Townsville, DEM, a map of the surface water from WOfS, a map of a potential flood from Townsville city council, and satellite imagery. Next, the DEM was processed to assist in defining the catchment boundaries and later for improving the satellite image classification. The freely available satellite images of Sentinel 2 and Sentinel 1 were processed, and the classifications of Sentinel 2 images were verified with the map of surface water from WOfS. Then, the classifications of Sentinel 2 images were used to justify the classification of Sentinel 1 images. The final classification of the flood extent derived from the Sentinel 1 images were compared with the potential inundation map from the flood modelling. Details of each step will be explained in the following sub-sections.

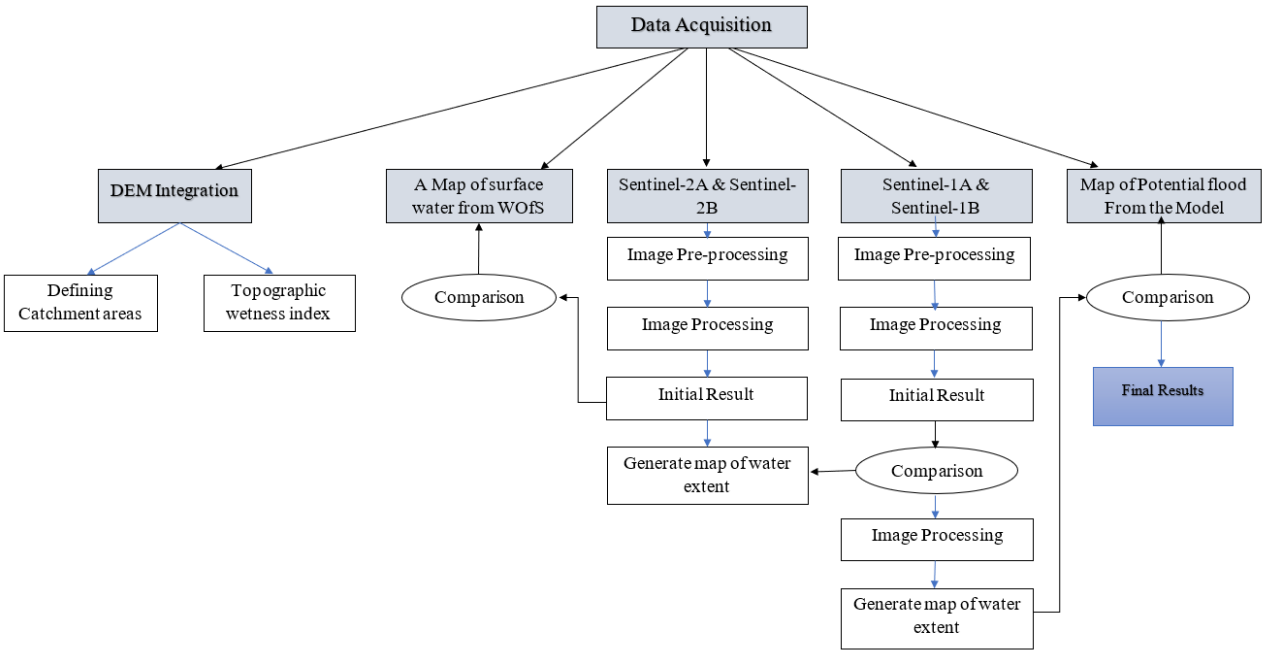


*Figure 5: The flowchart of the data collection and its method.*

## 3.1 Data collection

### 3.1.1 Townsville flood event

To understand more about the flood event relevant to this thesis, the dates that the flood occurred, the weather observations (rainfall, temperature, and wind speed), and the water release time and dates from the Ross River Dam were all investigated. According to the Bureau of Meteorology (2019b), persistent monsoonal rainfall had started affecting different parts of Townsville during the last week of January 2019 before starting to fade in the second week of February 2019. In the Ross and Bohle River catchments, the flood started to occur on Thursday 31 January with persistent rainfall. The Ross River Dam spillway gate had to be fully opened on the evening of Sunday 3 February (Bureau of Meteorology 2019b). The rainfall, temperature, and wind speed data at

Townsville Aero Station (station number 032040) between 1 January to 28 February 2019 (Appendix B) were collected to support the investigation of the flood event and also to support the selection of the satellite imagery. Regarding the rainfall data, a summary of historic cumulative rainfall from 1 January to 30 December in the years 2000, 2015, 2018, and 2019 yielded a difference in the amount of rainfall data in early 2019 compared with other historical data (Figure 6), including with regard to the split gate opening timeline (Figure 7). The cumulative rainfall from late January to early February 2019, which was at the time that the flood occurred, exceeded the previous highest readings in the year 2,000 by a considerable volume. A more detailed statement about the flood event and its related data is addressed in the Bureau of Meteorology (2019b) and in the BMT (2019).

Image removed due to copyright restriction.

*Figure 6: Cumulative rainfall at Townsville Aero Station: 032040.*
(Bureau of Meteorology 2019b)

Image removed due to copyright restriction.

*Figure 7: Rainfall and dam release timeline.*
(BMT 2019; Bureau of Meteorology 2019b*)*

### 3.1.2 Satellite imagery (Sentinel 2 and Sentinel 1)

Sentinel 2 and Sentinel 1 are part of the Earth Observation mission under the Copernicus Programme, which is supported by the European Space Agency (ESA). It provides imagery at a medium spatial and spectral resolution which is cost-free and is widely used for a number of applications such as land cover classification and flood monitoring (Malenovský et al. 2012; Yang et al. 2017; Zhu, Zhe, Wang & Woodcock 2015). Hence, predominantly relying on the free availability of Sentinel satellite imagery, this study used both Sentinel 2 and Sentinel 1 (Table 3 & Table 4) to detect water bodies and the water extent that occurred in Townsville city during this flash flood event. As a result of a near-simultaneous Sentinel 2 and Sentinel 1 imagery acquisition, a classification of Sentinel 2 imagery was used in particular as a baseline of "dry conditions" to verify the results of Sentinel 1 imagery classification. The acquisition dates of the images were decided upon by the availability of the images corresponding to the duration of the flood event and the rainfall data derived from rain gauge measurements at Townsville Aero Station. Both types of satellite images are derived from the Copernicus Open Access Hub (https://scihub.copernicus.eu/dhus/#/home).

#### *3.1.2.1 Sentinel 2*

Four different dates for the Sentinel 2A and Sentinel 2B images (Table 3 & Figure 8) categorised into dry and wet conditions were used to detect possibly permanent water and flood water extents. These were later used as a baseline for verifying the classification of the flood extent and, hence, the selection of the images for dry conditions were based on their temporal correspondence to the availability of the Sentinel 1 images (pre-flood event). Sentinel 2A and 2B are twin satellites under the Sentinel 2 mission that fly in the same polar sun-synchronous orbit providing 290 kilometres of the orbital swath width (Dutch 2019). These two satellites provide medium spatial resolution, multispectral imagery ranging from 10m through 20m to 60m based on 13 different spectral bands ranging from visible wavelengths through near-Infrared to shortwave Infrared wavelengths (Figure 9). The Multispectral Instrument (MSI) provides four of 13 bands at a spatial resolution of 10m and covers the visible wavelengths of red, green, blue, and near-infrared. At a spatial resolution of 20m, six of the 13 bands are derived from four regions of spectral wavelength ranging through infrared red edge, infrared and two bands of short-wave infrared. The lowest spatial resolution bands at 60m are derived from the three other bands which mainly detect atmospheric particles like aerosols, water vapour, and cirrus cloud. Apart from the spatial resolution, Sentinel 2 mission provides high- temporal resolution imagery with a revisit time of five days at the equator, which presents the potential to apply a time-series analysis. Two different product types freely accessible for users are the images that can be derived at levels 1C and 2A (Baillarin et al. 2012), although images at level 2A were only available over the European continent up until December 2018 and are currently in the stage of a gradual global roll-out through 2019. All the Sentinel 2 images used in this study (Table 3) were derived at the processing level 1C, with images containing reflectance at the Top Of Atmosphere

(TOA) and presenting cloud cover when there were no clear conditions. A graphical example of Sentinel 2 imagery of Townsville is shown in Figure 8.

| No | Satellite No | Acquisition date | Acquisition time (Local) | Instrument | Pass direction | Product type | Cloud cover (%) | Remark |
|---|---|---|---|---|---|---|---|---|
| 1 | S-2A | 26-Oct-18 | 10:27 | MSI | Descending | S2AMSIL 1C | 9.5 | Dry |
| 2 | S-2A | 25-Nov-18 | 10:27 | MSI | Descending | S2AMSIL 1C | 0.02 | Dry |
| 3 | S-2A | 13-Feb-19 | 10:26 | MSI | Descending | S2AMSIL 1C | 2.7 | Wet |

*Table 3: Summary of Sentinel 2 satellite images acquired for dry and wet conditions.*

*Figure 8: An example of MSI raw data from Sentinel 2 acquired on 26 October, 2018 with RGB bands 4, 3, 2.*

Image removed due to copyright restriction.

*Figure 9: MSI spectral bands and spatial resolution.*
(Gatti & Bertolini 2013).

#### *3.1.2.1 Sentinel 1*

Seven Sentinel 1 images acquired on different dates were used to detect water extent during the flood event (Table 4 & Figure 10). This set of images are categorised into pre-flood, during flood, and post flood conditions in order to derive water extent for this specific flood event. The Sentinel 1 mission (like the Sentinel 2 mission) is composed of a constellation of twin satellites – Sentinel 1A and Sentinel 1B – which move in the same orbit. These twin satellites were launched in September 2014 and April 2016 respectively, with a lifetime of 7 years and a consumables lifetime of 12 years (Torres et al. 2012). Sentinel 1 provides imagery with a revisiting time of 12 days with one satellite (with a high repeat frequency of six days for the final constellation) and high repetitiveness of three days at the equator (Torres et al. 2012). The Sentinel 1 mission provides a Radar image produced using the C band Synthetic Aperture Radar (SAR) instrument operating in the four different modes of Stripmap (SM), Interferometric Wide Swath (IW), Extra-Wide swath (EW), and Wave mode (WV), thereby resulting in different resolutions and swath widths (Figure 11). Sentinel 1 products are distributed in three processing levels which are level 0, level 1, and level 2, which represent raw products, single look complex (SLC) or Ground Range Detected (GRD) products, and Ocean (OCN) products respectively. The satellites acquire a dual polarisation of HH+HV, VV+VH with one transmitting chains of either H or V and the second receiving chains for H and V (Twele et al. 2016). According to the area of interest over land, the images used in this study were derived in the Interferometric Wide Swath with VV and VH polarisation, which provides geometric resolution up to 5 x 20m with a 250 km wide swath. The SLC mode was chosen so that the averaging of digital values, which occurs with multi-look products, did not occur.

| No | Satellite No. | Acquisition date | Acquisition time (local) | Instrument | Pass direction | Product type | Polarisation | Mode | Remark |
|---|---|---|---|---|---|---|---|---|---|
| 1 | S-1A | 27-Oct-18 | 5:44 | SAR-C | Descending | SLC | VV/VH | IW | Pre-Flood |
| 2 | S-1A | 31-Jan-19 | 05:44 | SAR-C | Descending | SLC | VV/VH | IW | Flood |
| 3 | S-1B | 6-Feb-19 | 05:43 | SAR-C | Ascending | SLC | VV/VH | IW | Flood |
| 4 | S-1A | 6-Feb-19 | 18:43 | SAR-C | Descending | SLC | VV/VH | IW | Flood |
| 5 | S-1A | 12-Feb-19 | 05:44 | SAR-C | Descending | SLC | VV/VH | IW | Post-flood |
| 6 | S-1B | 12-Feb-19 | 18:42 | SAR-C | Ascending | SLC | VV/VH | IW | Post-flood |

*Table 4: Summary of Sentinel 1 satellite images acquired for the flood event.*

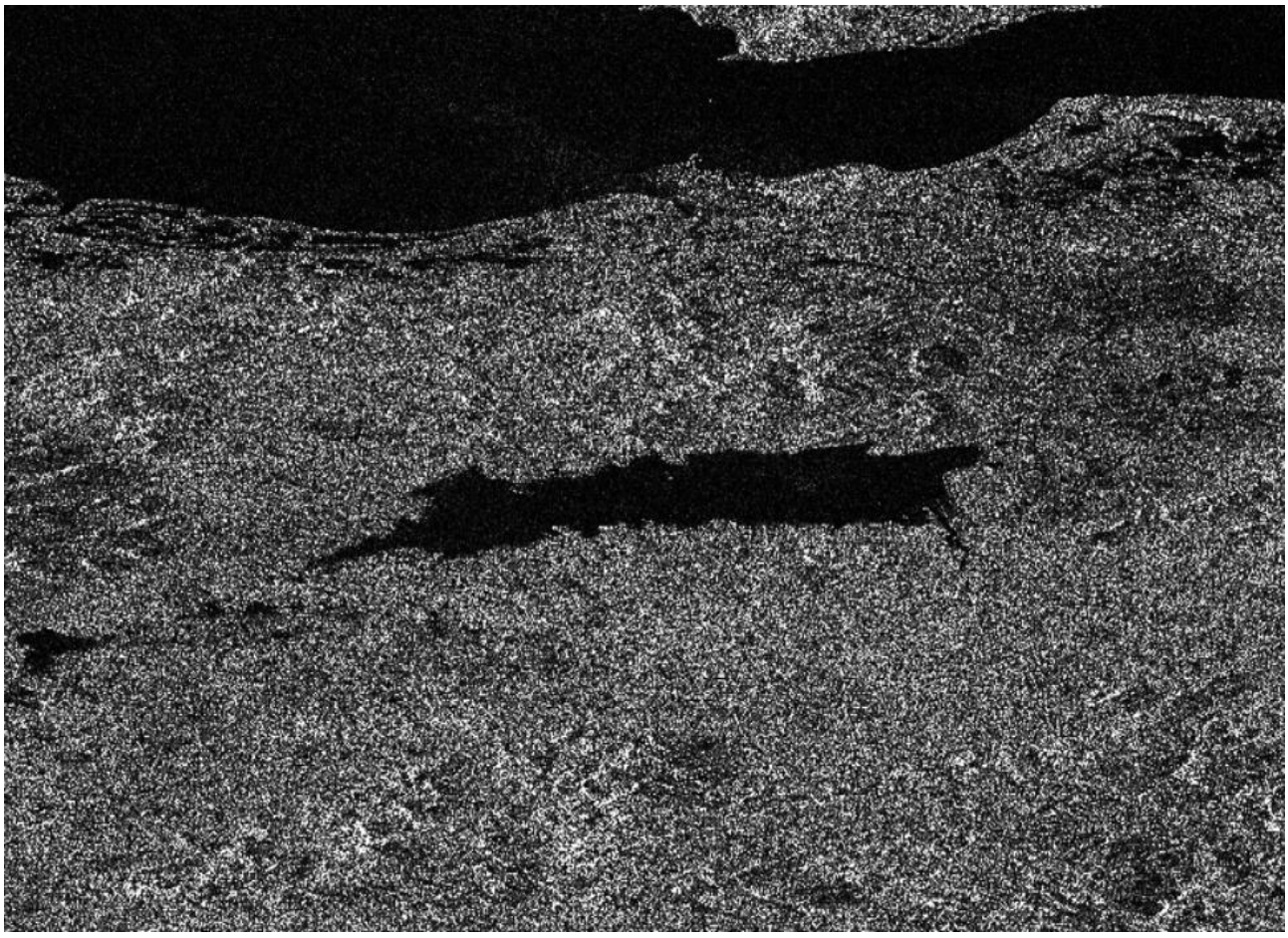

*Figure 10: An example of Radar data from Sentinel 1 acquired on 31 January, 2019 with VH polarisation (during flood event).*

*Note the lack of orientation and distorted geometry associated with this product.*

Image removed due to copyright restriction.

*Figure 11: Acquisition Modes for the Sentinel 1 mission.*
(Torres et al. 2012).

### 3.1.3 Map of surface water extent from water observation from space

A map of the extent of the surface water across the area of interest (Appendix C) was used to verify the accuracy of the image classification of the possible permanent water. This information about the occurrence of surface water is part of the Water Observation from Space (WOfS) product that covers the extent of surface water throughout Australia; it was developed by Geoscience Australia (Mueller et al. 2016). This product is a result of the classification of the Multidecadal archive of Landsat 5 and Landsat 7 satellite imagery acquired from 1987 to the present. The map of the extent of the surface water is presented with a pixel size of 61.5 x 61.5 metres. “Wet pixels” demonstrating water bodies were detected by applying a decision tree classifier method on every single-date image at each location. The result of each classification is summed and compared to every clear-sky observation at that location by using logistic regression (Mueller et al. 2016). More detail of the methodology is presented by (Mueller et al. 2016). The map of the surface water extent demonstrates a presence of water that is persistent through the time series (such as the water in reservoirs, lakes, rivers, and human-made ponds), with the pixels of surface water extent depicting where water is always present through to occasionally and then rarely present being represented with percentages ranging from a hundred to zero (Table 5). This geodata is freely downloadable via the Digital Earth Australia Website (http://www.ga.gov.au/dea/products#wofs).

| Range of the probability of water occurrence (%) | Description |
|---|---|
| 0 | No water detected |
| >1 | More than 1% of water occurrence in the observations (includes flooding and misclassified shadows). |
| >5 | More than 5% of water occurrence in the observations (includes intermittent water bodies). |
| >20 | More than 20% of water occurrence in the observations (includes water that often dries out). |
| >50 | More than 50% of water occurrence in the observations. |
| >80 | More Than 80% of water occurrence in the observations (permanent water). |
| 100 | Water that is always detected. |

*Table 5: Filtered water summary.*

(Geoscience Australian 2019).

### 3.1.4 Map of potential flood depth in Townsville

Ideally, a GIS layer derived from a flood model developed by Townsville City Council of potentially inundated areas could be compared with the flood extent mapped by satellite imagery. Despite ongoing efforts to obtain the flood model in GIS format from the Townsville City Council, the information was unable to be received in a timely manner. However, a published map of the potential flood depth of Townsville (in PDF format) was instead downloaded from the Townsville city council's website and compared with the satellite image classification for the Townsville flood event. The map was published on 3 February, 2019 by Townsville city council depicting the results of an analysis of the hypothetical scenario in which the water flow at Ross River reached 2,000 $m^3/s$ (City of Townsville 2019c). Although this map (Appendix D) had been produced merely to provide information with no consideration for any errors or omissions (City of Townsville 2019c), it was used to compare with the water classification from satellite imagery since it was the only available map on this subject.

### 3.1.5 Related spatial data

The GIS data for Queensland's coastline and catchment areas in Townsville were collected from the Queensland Government portal (https://wetlandinfo.des.qld.gov.au/wetlands/facts-maps/sub-basin-ross-river/). These were used to define the study area as well as to mask out the redundant areas from the satellite imagery. Apart from this, the 30 m and 1 m resolution DEM of the city of Townsville was used to support the classification. The DEM is freely provided by the Intergovernmental

Committee on Surveying and Mapping (ICSM), a standing committee of the Australian and New Zealand Spatial Information Council. Hence, the DEM was downloaded from ELVIS: Elevation and Depth Foundation Spatial Data website (https://elevation.fsdf.org.au/).

## 3.2 Software used

Several types of geospatial and image processing software including Sentinel Application Platform 6.0 (SNAP), Environment for Visualizing Images 5.4 (ENVI), Earth Resources Data Analysis System (ERDAS) Imagine 2018, and ArcGIS 10.6.1/ ArcGIS Pro 2.3 were used to pre-process and prepare data for processing and analysing tasks as well as producing maps of the water's extent. Since SNAP is a free Sentinel toolbox which fully supports Sentinel products, especially Sentinel 1, it was used mainly to pre-process the Sentinel Radar images before applying further image processing with the other software.

## 3.3 DEM integration

### 3.3.1 Topographic Wetness Index

The 1m resolution DEM was used to produce a Topographic Wetness Index (TWI). TWI is a method that makes use of high-resolution DEM to describe the topography, the location, and the possible saturated areas that are likely to be affected by overland flow (Ali et al. 2014). With such characteristics, TWI was aimed to help improve the classification from satellite images in further analysis. Despite numbers of the modified TWI methods which add more parameters like distance, soil transmissibility, and hydraulic conductivity coefficient to aid in more complex tasks (Pourali et al. 2016), this research relied upon the original formula of TWI due to its reduced dependence on the user's input and its ease of implementation. The TWI is generated based on the TWI formula proposed by Beven & Kirkby (1979), which can be applied in the ArcGIS 10.6.1/ ArcGIS Pro 2.3.

$$\mathrm{TWI} = \ln\left(\frac{a}{\tan\beta}\right) \quad (1)$$

*Equation 1: TWI.*

*Modified from (Beven & Kirkby 1979).*

Where $a$ represents the number of upslope pixels derived from the scale of flow accumulation; $\tan\beta$ represents the tangent of the steepest downslope at each pixel.

### 3.3.2 Defining catchment areas

The GIS file of the main catchment boundary and the sub-drainage boundary was used in conjunction with the sub-catchment generated to establish the areas of the Bohle River catchment, the Ross River (upper) catchment, and the Ross River (lower) catchment. These newly generated sub-catchments were created using an automatic watershed delineation of the 1m resolution DEM.

The pour point was created to support the delineation and the delineating process was accomplished using the spatial analysis tools provided in ArcGIS 10.6.1/ ArcGIS Pro 2.3. The final defining process for the catchments of Bohle River, Ross River (upper), and Ross River (lower) was based on the map of the Ross River Basin published by the Queensland government (Appendix E).

## 3.4 Image analysis

Since the data used in this research demonstrates two different types of satellite imagery, different classification methods were applied to extract water information within the study area. The classifier applied with the multispectral image is a spectral-based classification called Normalised Difference Water Index using a threshold. Unlike the multispectral image, the Radar image does not provide spectral information of objects but rather backscatter values at two polarisations and, hence, a different method of density slicing was applied to detect smooth versus rough surfaces. More detail of image processing stages is explained in this sub-section and the overall workflow is presented in the following flowcharts (Figure 12 & Figure 13).

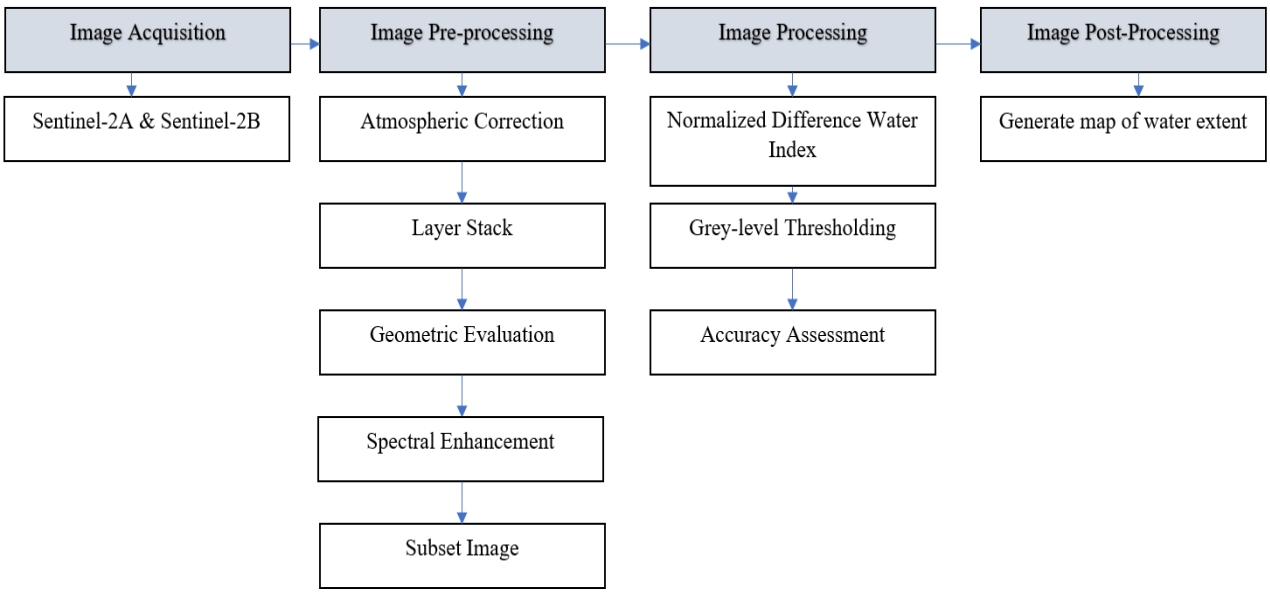


*Figure 12: Overall workflow of water-extent classification from a multispectral image.*

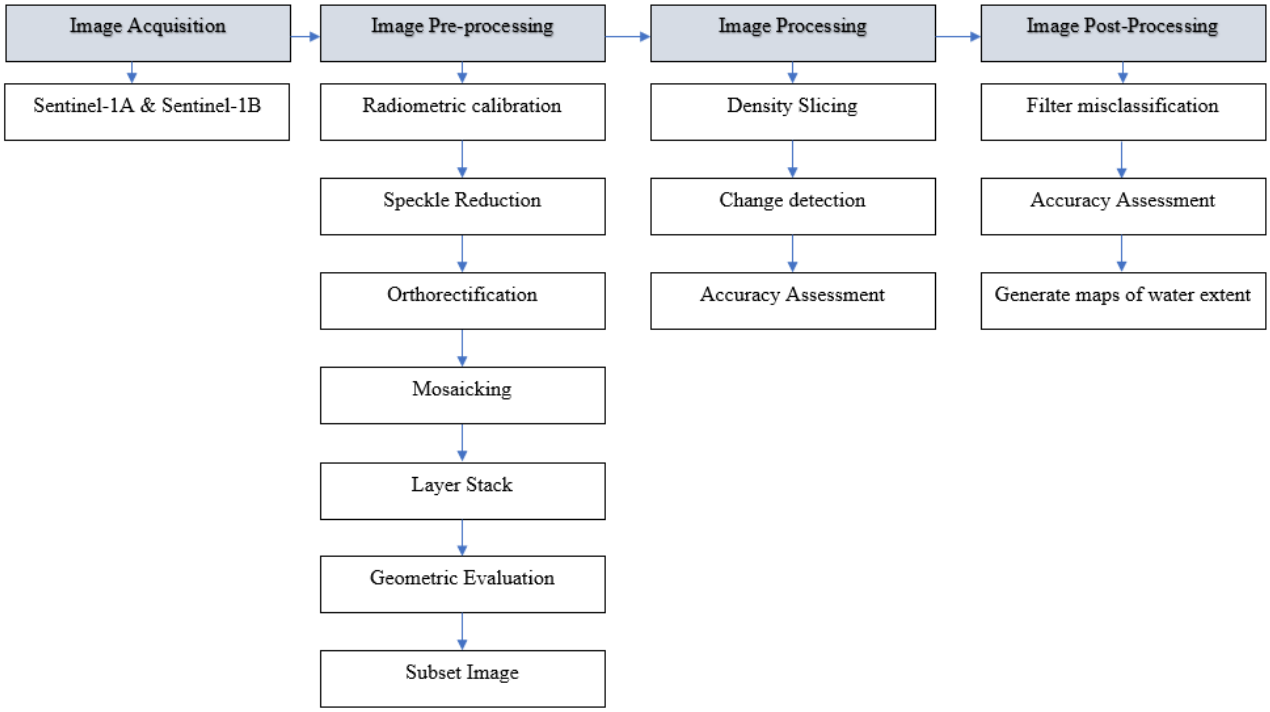


*Figure 13: Overall workflow of water-extent classification from a Radar image.*

## 3.5 Digital image pre-processing for Sentinel 2

### 3.5.1 Atmospheric correction

The Sentinel 2 level 1C product provides a Top of Atmospheric (TOA) scaled radiance image which means that the satellite image provides the atmospheric reflectance instead of Earth surface reflectance. Atmospheric particles can either absorb or scatter the radiance from both the sun and that which is reflected from the Earth's surface. Hence, to achieve the reflectance at the bottom of the atmosphere (BOA), an atmospheric correction was applied (Matthew et al. 2002). There are a number of algorithms and methods for atmospheric correction which are available for this purpose, such as Fast Line-of-sight Atmospheric Analysis of Spectral Hypercubes (FLAASH), Quick Atmospheric Correction (QUAC), Dark Object Subtraction (DOS), Atmospheric and Topographic Correction (ATCOR), and Sen2Cor (Nazeer, Nichol & Yung 2014; Yusuf et al. 2018). These sophisticated methods have been developed to utilize proper atmospheric properties required for the correction (Ariza, Robredo Irizar & Bayer 2018). Since Sen2Cor is an atmospheric correction processor that is fully supported by the SNAP Software, this was applied to all Sentinel 2 imagery used in this research. The Sen2Core processor provides correction for atmosphere, terrain, and cirrus effects that are applied to the Top of Atmospheric level 1C product (Figure 14). As a result, this processor produces an Earth surface reflectance image, which is especially necessary when the comparisons are made among images acquired on different dates or using different sensors (Louis et al. 2016; Müller-Wilm, Devignot & Pessiot 2016).

Image removed due to copyright restriction.

*Figure 14: Sen2cor processing workflow.*
(Gascon et al. 2017).

### 3.5.2 Layer stack

The original image file derived from sentinel 2A and 2B contains 13 unique bands. Each band presented as a greyscale imagery and hence, to derive a multispectral image file, every single band needed to be fused together. Although Sentinel 2 mission provides 13 different bands that are derived from different wavelengths, some bands such as the three bands that indicate atmospheric particles (aerosol, water vapour, and cirrus) do not contain much useful information for classifying water. Hence, to ignore redundant data that only adds to processing time, these three bands were not combined with the others.

### 3.5.3 Geometric evaluation

Geometric correction is a significant step in remote sensing image processing, particularly when there is a requirement for multi-source data integration (Toutin 2004). Usually, the image that is derived directly from the remote sensing satellite will contain geometric distortions (Toutin 2004), which results in a constraint when relating this data to other mapping products with a specific map projection and datum (Toutin 2004). Geometric distortion of the imagery can be caused by different factors such as the error from acquisition systems like the platform and measuring instruments (Toutin 2004). A number of geometric correction models, both physical and empirical, have been proposed in literature (Gonçalves, Gonçalves & Corte-Real 2009; Wang et al. 2012). Specifically, empirical models, which rely upon a bundled mathematical function and do not require any physical or sensor information, are commonly used for the geometric correction of remote sensing imagery (Wang et al. 2012). More detail about Empirical models and other geometric correction models can be found in Toutin (2004). To geometrically correct the Sentinel 2 imagery used in this research, empirical models based on a 2D polynomial model were used. This is appropriate because ESA has already corrected the imagery for 3D errors such as relief displacement in their level 1C products. Toutin (2004) recommends using at least 12 Ground Control Points (GCPs) that are evenly spread

across the image (Figure 15). This research collected 25 Control Points (CPs) over the imagery as well as from a reference image. Instead of using reference GCPs from a field measurement (due to the lack of data), Bing Aerial Base Map (provided in ERDAS Imagine with a higher spatial resolution than that of Sentinel products) was used as the reference image. Despite there being a number of methods for validation, the traditional root mean square (RMS) of residuals was applied to quantitatively evaluate the confidence of the geometric correction. To derive the final resulting geometric correction, the image was resampled using the Nearest Neighbour (NN) method so that the original pixel values were preserved.

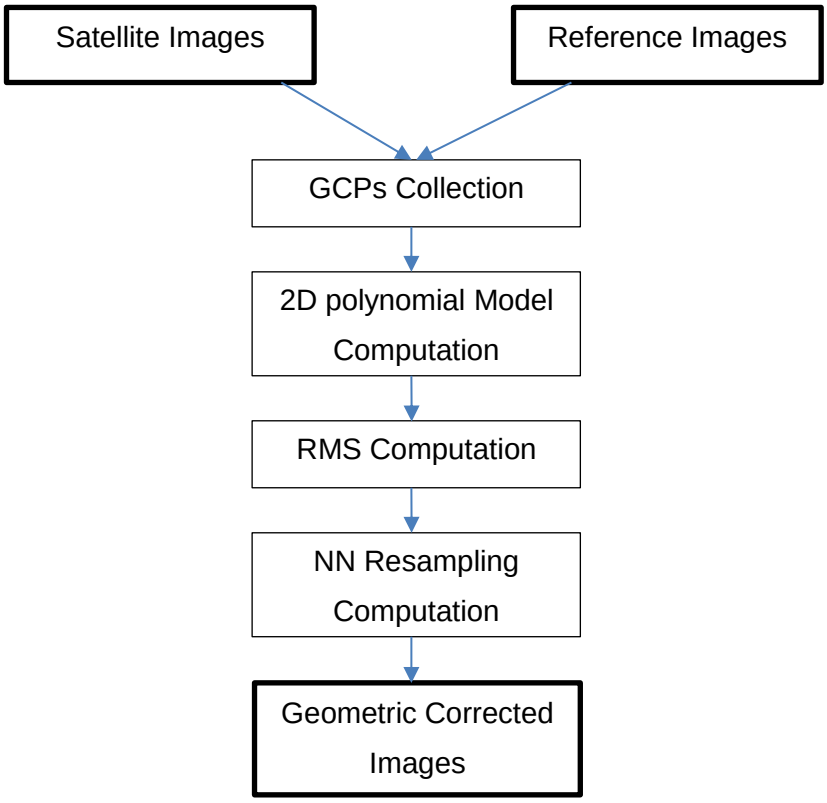


*Figure 15: Workflow for geometric correction.*

### 3.5.4 Noise removal

Although the multispectral Sentinel 2 images have been radiometrically corrected from TOA to Bottom of Atmospheric (BOA) reflectance, the images still contain some degree of noise from either the sensor or the atmosphere (Loughlin 1991). To reduce such noise from the images used in this research, Principal Component Analysis (PCA), a common spectral enhancement technique, was applied. This technique started with deriving the variance-covariance matrix of all the multispectral bands of an image, and this was followed by computing the eigenvalues and eigenvectors of the dataset, before finally performing a linear transformation from the dataset into principal component bands. In the transformation, the first component band will account for the most variance of the original dataset while the variance in the other remaining components will decrease depending on the differences among the spectral regions in each band (Loughlin 1991). Eventually, the noise can

be reduced in the image by removing the principal component bands that contain low variance and only preserving the bands that contain related information through an inverse PCA. Further information about the PCA can be found in ERDAS (1999).

### 3.5.5 Subset image

To reduce the size of the image, which can contribute to the processing time, the image was clipped (subset) to the extent of the study area as described in section 3.2.2. The boundary that was used to subset the image was derived from the combining of the Bohle and Ross River catchments.

## 3.6 Digital image processing for Sentinel 2

Understanding the characteristics of the image is as important as the selection of algorithms to classify the image and, hence, the spectral signatures of different features were investigated and various methods were experimented with.

### 3.6.1 Spectral signature investigation

The spectral characteristics of materials on the Earth's surface are important for digital image classifications. To identify the proper method for classifying water apart from non-water features, particularly in this urban area where there are complex objects, different spectral-based methods have been applied. Fundamental to this approach is the collection of spectral profiles of different landcover types and unsupervised classification. The collection of each spectral signature allows for visual inspection of the reflectance spectrum through all spectral bands, while an unsupervised classifier provides initial inspection for the discrimination of various features including water and other features, including for dark objects in particular.

Firstly, the spectral signatures of five main features (water, vegetation, the airport runway, rooftops, and bare soil) within the area of interest were collected. Five samples of each type of signature were collected to ensure the consistency of its signature. The spectral profile of each feature was visually and numerically compared to one another as to whether there were any similarities in terms of reflectance value, focusing on the comparison of water surface with the other surfaces.

Fifty random classes were set in an unsupervised classification. In ERDAS IMAGINE, the Iterative Self-Organizing DATA (ISODATA) analysis technique was utilised to perform the classification, which means that this technique will repeatedly perform pixel assignment to the random 50 classes before recalculating the statistics until the defined criteria are met (Dhodhi et al. 1999). The ISODATA technique uses spectral Euclidean distance formula to form a cluster of pixels with similar spectral characteristics which will eventually provide different classes of landcover type (Dhodhi et al. 1999), showing the ambiguity of the classification among landcover types within a class.

### 3.6.2 Water-related index base method

The use of the water-related index is a common method to classify surface water and non-water in imagery due to the differences in spectral reflectance of different landcover types (especially for water which mostly absorbs radiance in NIR and SWIR wavelengths), the ease of using such a method, and the efficiency of computation in terms of the time required (Feyisa et al. 2014; McFeeters 1996; Xu 2006). A number of studies have classified surface water using different water-related indexes including NDWI, MNDWI, and AWEI, all of which show different results (Campos, Sillero & Brito 2012; Fisher, Flood & Danaher 2016; Yang et al. 2017). To determine the most suitable method to delineate surface water within the area used for this research, all the above-mentioned methods were applied.

McFeeters (1996) proposed the NDWI method to differentiate water from other objects by using the green and NIR wavebands (Equation 2).

$$NDWI_{McFeeters} = \frac{\rho_{(Gree\ n)} - \rho_{(NIR)}}{\rho_{(Green)} + \rho_{(NIR)}} \quad (2)$$

*Equation 2: $NDWI_{McFeeters.}$*

Where $\rho$ represents the reflectance value of the spectral bands (Green and NIR) for optical imagery.

Xu (2006) suggested the MNDWI approach to delineate surface water by replacing the NIR waveband in the NDWI method with the SWIR waveband (Equation 3).

$$MNDWI_{Xu} = \frac{\rho_{(Green)} - \rho_{(SWIR)}}{\rho_{(Green)} + \rho_{(SWIR)}} \quad (3)$$

*Equation 3: $MNDWI_{Xu.}$*

Where $\rho$ represents the reflectance value of the spectral bands (Green and SWIR) in an optical image.

Recently, a new water-related index method AEWI has been proposed by Feyisa et al. (2014) where more components than two different wavelength bands have been added to improve the classification (Equation 4 & Equation 5).

$$AWEI_{nsh} = 4 * (\rho_{(Green)} + \rho_{(SWIR)}) - (0.25 * \rho_{(NIR)} + 2.75 * \rho_{(SWIR)}) \quad (4)$$

*Equation 4: $AWEI_{nsh.}$*

$$AWEI_{sh} = \rho_{(Blue)} + 2.5 * \rho_{(Green)} - 1.5 * (\rho_{(NIR)} + \rho_{(SWIR)}) - 0.25 * \rho_{(SWIR)} \quad (5)$$

*Equation 5: $AWEI_{sh.}$*

Where, $\rho$ represents the reflectance value of the spectral bands (green, blue, NIR, and SWIR) of an optical image; $AWEI_{nsh}$ indicates the equation is suitable for the area where there is no significant shadow effect; and $AWEI_{sh}$ demonstrates the equation is suitable for an area where there is shadow effect.

### 3.6.3 Thresholding classification

After applying the water-related index, using a binary threshold is the common method to extract surface water extent from its background (Yang et al. 2017). Although the most common suggestion is that a threshold value greater than 0 is the most likely value to be classified as water and negative values as non-water, different studies propose different threshold values for a normalised difference water-related index image (Feyisa et al. 2014; Xu 2006). In this research, a threshold of 0 was initially selected to extract water surfaces and the result was visually compared to the multispectral image. Different threshold values were compared for the classification and, hence, a threshold value greater than -0.01 was eventually applied with every normalised difference water-related index image. However, it is suggested that a normalised difference water-related index image is still affected by the reflectance from built-up surfaces in urban environments (Xu 2006). A proposed combined thresholding is recommended by Yang et al. (2017). By taking advantage of the unique spectral signature of water and its low reflectance value of SWIR band, this study combines the threshold of a value greater than -0.01 from the normalised difference water-related index image together with a threshold of reflectance value at the second SWIR of the Sentinel 2 image which is smaller than 1,000 (BOA reflectance multiplies by 10, 000). As a consequence, any confusion between water and non-water surfaces will be eliminated.

### 3.6.4 Accuracy assessment

To provide confidence regarding the image classification, an accuracy assessment of the classification against the reference data was applied. The most common and acceptable technique is based on the confusion or error matrix (Foody 2002) and, hence, it was applied in this project. Commonly, this accuracy assessment will provide overall accuracy of the image classification as well as the kappa coefficient (k) of the accuracy where a higher the value of k demonstrates a better agreement of the classification and the reference (Foody 2002). By relying solely on the error matrix method, the extent of water and non-water classifications were compared to the map of surface water extent from WOfS as reference data. The overall accuracy was derived from the proportion of the total agreement of water and non-water area over the whole study area. The set of equations, which are modified from (Yang et al. 2017), and which demonstrate the derivation of the overall

accuracy (OA), the producer's accuracy (the error of Omission), and the user's accuracy (the error of commission) are:

$$\text{Omission Error} = \frac{OE}{OE+AP}; \quad (6)$$

*Equation 6: Omission error.*

$$\text{Commission Error} = \frac{CE}{OE+AP}; \quad (7)$$

*Equation 7: Commission error.*

$$\text{Overall Accuracy} = \frac{AP}{OE+AP}; \quad (8)$$

*Equation 8: Overall accuracy.*

$$\text{Kappa} = \frac{TP*(AP+NP)-\sum}{TP*TP-\sum} \quad (9)$$

*Equation 9: Kappa coefficient.*

$$\sum = (AP * OE) + (AP * CE) + (NP * NP) \quad (10)$$

*Equation 10: Sum of indicators.*

Where TP (Total pixels) represents the total number of pixels in the experimental area; AP (Agree pixels) represents the number of pixels that agree as water; CE (Commission Error) represents the number of pixels that show as water in the classified image but not in Reference image; OE (Omission Error) represents the number of pixels that show as water in the reference image but not in the classified image; and NP (Non-agree pixels) represents the pixels that disagree as water.

## 3.7 Radar image pre-processing for Sentinel 1

### 3.7.1 Radiometric calibration

The raw Sentinel 1 SAR imagery provides digital numbers which indirectly relate to the value of the Radar backscatter. Radiometric calibration was applied to convert the pixel value of the image to the true Radar backscatter of the surface. In order to compare the different images, it is necessary to derive the true value of the backscatter. To convert the digital pixel values to the value of the Radar backscatter of surface reflectance, the radiometric calibration tool available in SNAP was used (Equation 11). Since the software fully supports Sentinel 1 products, it is able to use the annotations provided within the image metadata.

$$\sigma^0 = \frac{< DN >^2}{A_\sigma^2} \quad (11)$$

*Equation 11: Sentinel 1 Radiometric Calibration.*

$$DN = \sqrt{(I^2 + Q^2)} \quad (12)$$

*Equation 12: Pixel digital number.*

Where DN represents the pixel's digital numbers of the square root of the combination to the power of two of each value from the measurement file, which account for the real value (I) and the imaginary value (Q); and $A_\sigma$represents the Radar cross-section sigma naught.

### 3.7.2 Image de-speckle

The Radar image will normally provide bright and dark pixels which are called speckle. This speckle, often incorrectly termed "noise", is caused by the inconsistency of the phase when the Radar signal returns to the sensor. Speckle causes a change in the intensity values of the image which leads to a decrease in the image's appearance as well as the quality of the image. Hence, to undertake the Radar image analysis, speckle removal is one of the important steps in the process before further analysis. Since reducing speckle in the image can also lead to a change in the image, several de-speckle models have been developed for different applications and sensors. Adaptive filters like Gamma-map and Lee-sigma are some of the most popular filters to better preserve the radiometric and textural information of the image (Baraldi & Parmiggiani 1995; Lee 1980). Hence, after applying different filters and comparing the quality and the appearance of the images, this research eventually applied the Lee-sigma filter, with the moving windows of 5 x 5 pixels corresponding to the pixel size of 8 x 8 metres.

### 3.7.3 Image orthorectification

Unlike optical/multispectral imagery, SAR imagery is derived from a side-looking sensor and experiences significant distortion from the topographical variation within a scene. Image orthorectification has been a common process to correct the imaged terrain, with this initially reducing the distortion and representing the geometry of the image as being close to real-world geometry (Small & Schubert 2008). The SNAP application provides a range doppler terrain correction operator to automatically rectify the image and, hence, it is used for this research. The operator allows the geometric correction from the slanted image to the actual position on the Earth's surface by making use of the available information in the image's metadata, the DEM in the online library (SRTM 1Sec HGT), and by applying the orthorectification algorithm provided by Small (2008). Since a group of Ground Control Points (GCPs) were not simultaneously used in this orthorectification, a second minor adjustment to the 2D ortho-rectified image was subsequently required.

### 3.7.4 Geometric evaluation

Following the image orthorectification, another step of geometric correction was required to improve the accuracy of the position of the image (Blacknell et al. 1989). Similar to the multispectral image where the automatic method can provide initial geometric correction, a geometric model like a 2D polynomial model to enhance accuracy was applied in this research. Traditionally, the proper numbers and distribution of GCPs collected from the fields are required to generate geometric correction (Zhou et al. 2012). Due to the lack of the GCPs, the multi-geometric correction tool provided in ERDAS Imagine was used to collect GCPs from Bing Aerial Base Map, which has a higher spatial resolution than Sentinel products. Although the collection of Control Points (CPs) from SAR imagery is far more difficult than for multispectral images due to the distortion of images as presented to human eyes, 20 out of 30 CPs could be used for the correction. Essentially, the principle of 2D polynomial model applied for this correction is similar to the one applied to the Sentinel 2 imagery.

### 3.7.5 Subset image

Similar to section 3.5.5, the image should be subset to an area of interest before starting the image processing so as to enhance the processing time and avoid storage limitations.

## 3.8 Digital image processing for Sentinel 1

In this subsection, all experimental techniques such as polarisation investigation, a selection of density slicing, verification of the density slicing, and detection of the change in a potentially smooth surface through the time-series of the flood event will be addressed.

### 3.8.1 Polarisation investigation

Sentinel 1 SAR imagery provides two polarisation modes, with one being VV and the other VH. To detect surface water from SAR imagery, the application of polarisation is important. Several studies proposed that like-polarised images (VV/HH) will better identify water bodies when compared with cross-polarised images (VH) (Henry et al. 2006). However, it has also been proven that VV polarised data is more sensitive to surface roughness while cross-polarisation demonstrates higher resistance when applied to windy conditions, especially during a flood caused by local weather systems; but it is also sensitive to vegetation (Baghdadi et al. 2001; Shen et al. 2013). Hence, by consulting the backscatter variation of possibly constant smooth surfaces, such as water, as well as the trade-off of the like- and cross-polarisations, this research is considered an experiment in the combination of both polarisations to delineate the flood extent.

### 3.8.2 Density slicing

Density slicing (backscatter thresholding) is one of the most common methods to classify water from non-water surfaces (Martinis, Twele & Voigt 2009). Similar to the grey level threshold for a normalised difference water-related index, density slicing relies on assigning pixels of SAR imagery

that contain a scattering cross-section lower than a certain threshold value as smooth (water) class or greater than the value of the non-water class (Brivio et al. 2002; Martinis, Twele & Voigt 2009). For this research, density slicing was first applied to the single image of dry conditions and a single image of wet conditions, which were acquired on 27 October, 2018 and 12 February, 2019 respectively. These images were selected due to their correspondence to the dates of the dry and wet conditions of the Sentinel 2 multispectral images, which were used to validate data for SAR image processing. A threshold value was initially selected by observing the backscatter histogram and subtracting its Standard Deviation (SD) value from the mean of the backscatter of the image, where the SD of the image derived on 27 October was equivalent to 3 dB and the mean was -14.757 dB. Then, the sensitivity comparison varying amount of the SD (1 to 5 dB) were subtracted from the mean. The aim was to investigate the best threshold value. Regarding the minor backscatter variation of possibly constant smooth surfaces like the airport runway on different dates, similar threshold criteria were applied to the wet-conditions image derived on 12 February, 2019.

### 3.8.3 Verification of the classification

It is challenging to select the proper threshold value for the backscatter value to delineate water from non-water. An incorrect threshold value can lead to either a misclassification or an over-classification of the water extent and, hence, verification is required. Similar to the common accuracy assessment for raster classification, the results from different density slicing were compared to the water classification of Sentinel 2, which was proposed as the most accurate estimate of the water extent. The overall accuracy, commission and omission errors of such results were consulted for the selection of the best threshold value so that the same method could be applied to the other SAR images used in the research.

### 3.8.4 Change detection

To detect the flood extent, both single-image and multi-temporal image algorithms have been used. However, it is accepted that a multi-temporal algorithm approach produces better results than those of a single algorithm (Schlaffer et al. 2015). A change detection method is one of the most popular methods to delineate the flood extent from SAR data by making use of the change of the backscatter occurring before, during, and after a flood event. This method yields promising results (Lu, D et al. 2004) and, hence, it was applied to the set of images used in this research (Figure 16). When using SAR images, water bodies are potentially detected based on differences in backscatter between rough and smooth surfaces. The detection of the flood extent using the change detection method relies upon the possibility that land, generally a rough surface, will change to a smooth surface when it is flooded. This change detection method is used in combination with the thresholding method (Equation 13), where the thresholding of the dry-conditions image was subtracted from the thresholding of each of the wet-conditions images (images acquired during and after the flood event). Unlike single-date thresholding, change detection facilitates the removal of the over-detected pixels that represent smooth surfaces but are not necessarily flood water. By performing this step in the

process, only the thresholding pixels that demonstrate a change from a rough to a smooth surface, when compared to the threshold from dry conditions, were retained and classified as a change in the water extent.

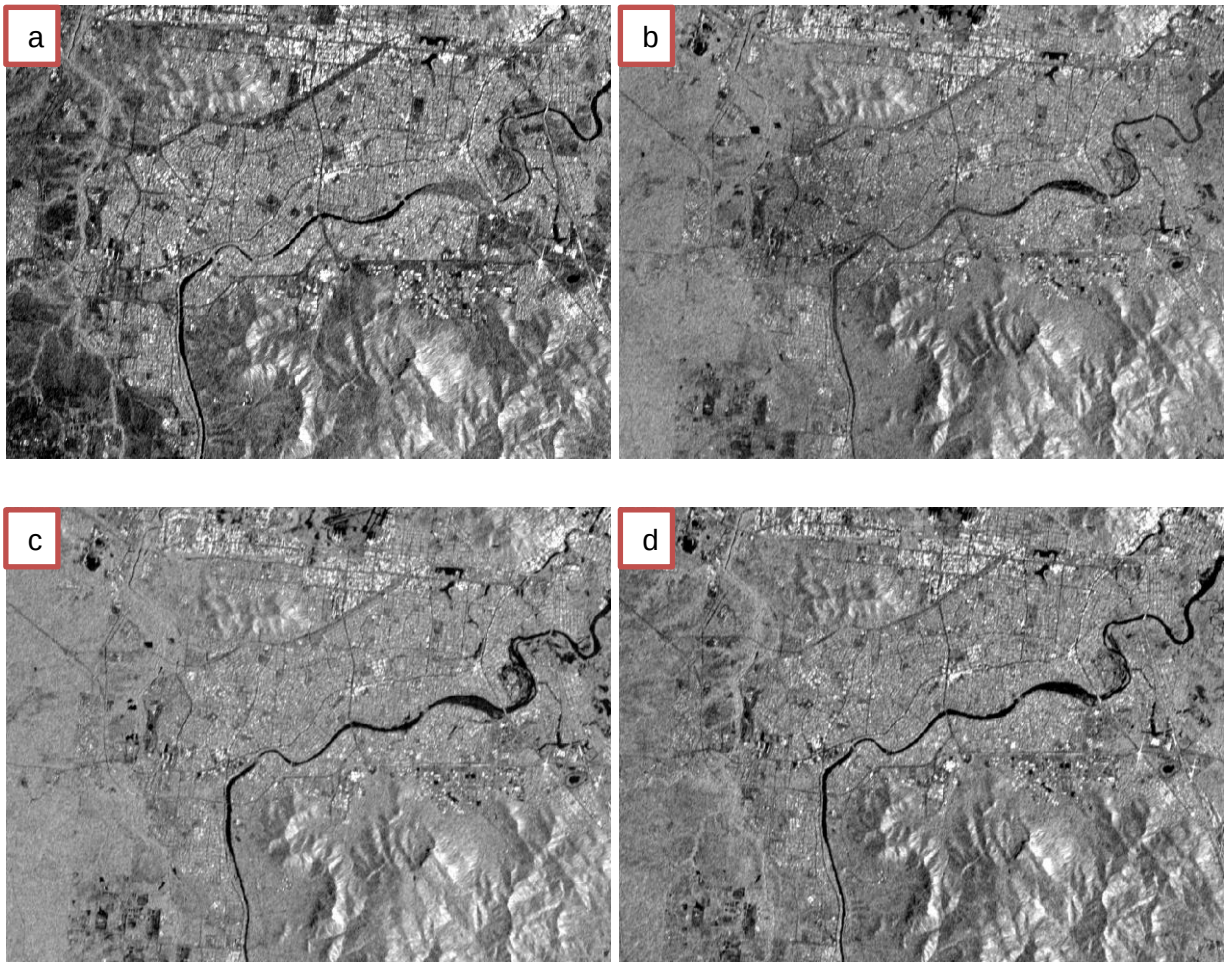


*Figure 16: An example of the change in the backscatter on the image; a) dry conditions on 27 October, 2018; b) & c) during the flood on 31 January, 2019 and 06 February, 2019; d) post flood on 12 February, 2019.*

$$Pf = T_f - T_{pw} \quad (13)$$

*Equation 13: Traditional Change Detection method.*

Where *Pf* represents possible change in water extent; $T_f$ represents thresholding classification for possible water on a specific day of flooding; and $T_{pw}$ represents thresholding classification for possible water from the dry-conditions image acquired before the flood event.

## 3.9 Image post-processing

To derive a total flood extent map which includes both permanent water and flood water, the classification of the flood extent acquired from the change detection method was used in combination

with the permanent water classification from the Sentinel 2 images (dry conditions). The following sub-section will explain the methods that were applied after the processing stage, which include a filter for misclassified pixels and the re-assessment of the accuracy of the classification.

### 3.9.1 Filtering misclassification from Sentinel 1 images

The over-classification of smooth (water) surfaces along the hilly areas was removed using the slope value derived from DEM. By numerically investigating the classification and the range of the slope values, the binary thresholding of a slope value of above 15 degrees was applied in conjunction with the classification image. The slope value above 15 degrees was assigned 0 while pixel values less than 15 degrees were assigned 1. When combining this binary threshold with the classification, any over-classification was minimised.

### 3.9.2 Re-assessing the accuracy of water extent classification from Sentinel 1 images

The results from section 3.9.1 were compared to the classification from Sentinel 2 images. This assessment followed the same principle as that described in section 3.8.3 with the purpose to investigate if applying such a filter can help improve the accuracy of the classification.

### 3.9.3 Generating maps of water classification

The final process was to create maps of pre-, during, and post flood events that were derived from the classification of the Sentinel 2 and Sentinel 1 images, with each map being individually generated using ArcGIS 10.6.1.

## 3.10 Comparison of potential flood extent maps

Due to the lack of a proper GIS file for an inundation map of flood modelling, the maps derived from the classification of Sentinel 1 images were qualitatively compared with the map of potential flood depths published by Townsville city council. This map was created based on the hypothetical scenario of water flowing at 2,000 $m^3/s$ at Ross River. This hypothetical scenario was dated the third of February, 2019 and, hence, only the maps of the images acquired on 31 January (described as pre-release water from the Ross River dam) and 6 February were used (described as post-release conditions).

# CHAPTER FOUR: RESULTS

In this chapter, the results of the processes described in the previous chapter will be reported.

## 4.1 Results from digital image pre-processing for Sentinel 2

### 4.1.1 Atmospheric correction

Since Sentinel 2 images were derived at level 1C, with TOA reflectance that could affect their classifications, atmospheric correction was applied and this resulted in derived Sentinel 2 images at level 2A with BOA reflectance. The results provided a marked change in the spectral reflectance value of each landcover type (Figures 17 and 18). For example, the spectral reflectance of band 1 (representing the Aerosols band) contains a relatively high pixel value above 1,000 for all landcover types but this was corrected to almost less than 1,000, except for the reflectance from built-up features which almost remained the same. The spectral reflectance in the visible bands improved, particularly for band 2. For instance, the spectral reflectance of vegetation after atmospheric correction presents low reflectance at band 2 yet high reflectance at band 3 (green) as well as at the red edge and NIR bands, which correspond to the generic spectral signature of vegetation presented by Dianderas (2014). This indicates that the effects of the atmosphere at these spectral bands have been corrected to the surface reflectance value.

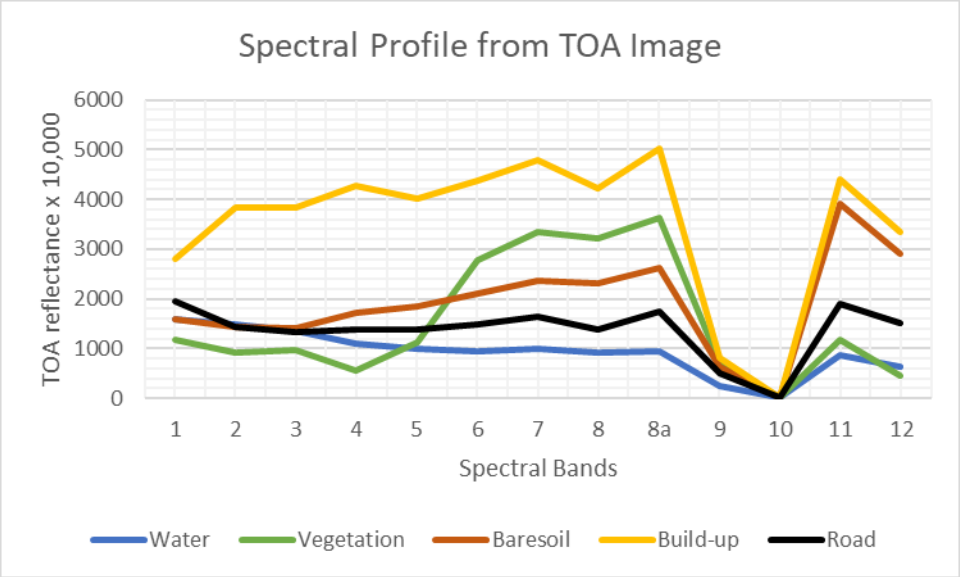


*Figure 17: The spectral profile of different landcover types from TOA reflectance of the Sentinel 2 image acquired on 26 October, 2018.*

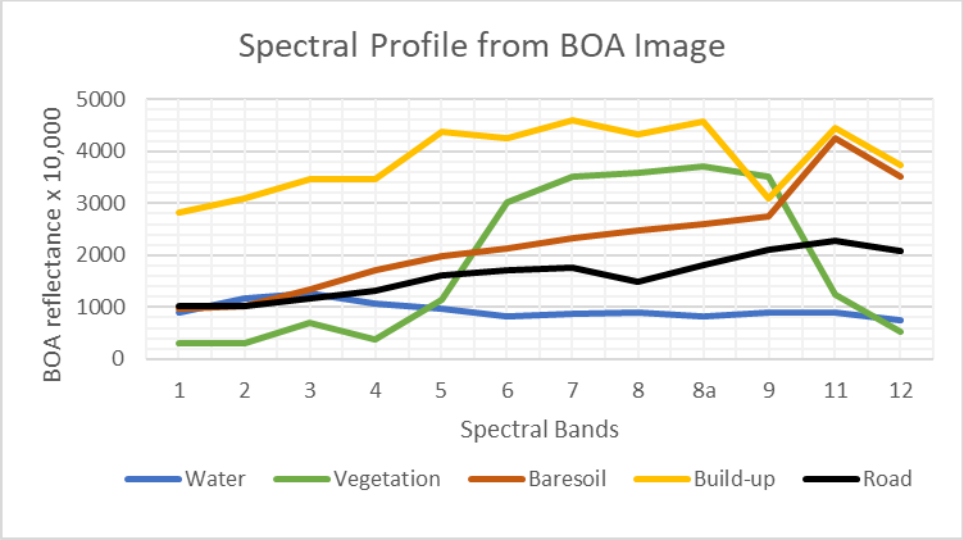


*Figure 18: The spectral profile of different landcover types from BOA reflectance of the Sentinel 2 image acquired on 26 October, 2018*

### 4.1.2 Layer stack

Layer stacking single-band images resulted in one multispectral image file (Figure 19). The single band image clearly provides only greyscale colour which visually presents less distinction in differences between objects when compared to the multispectral image (Figure 19).

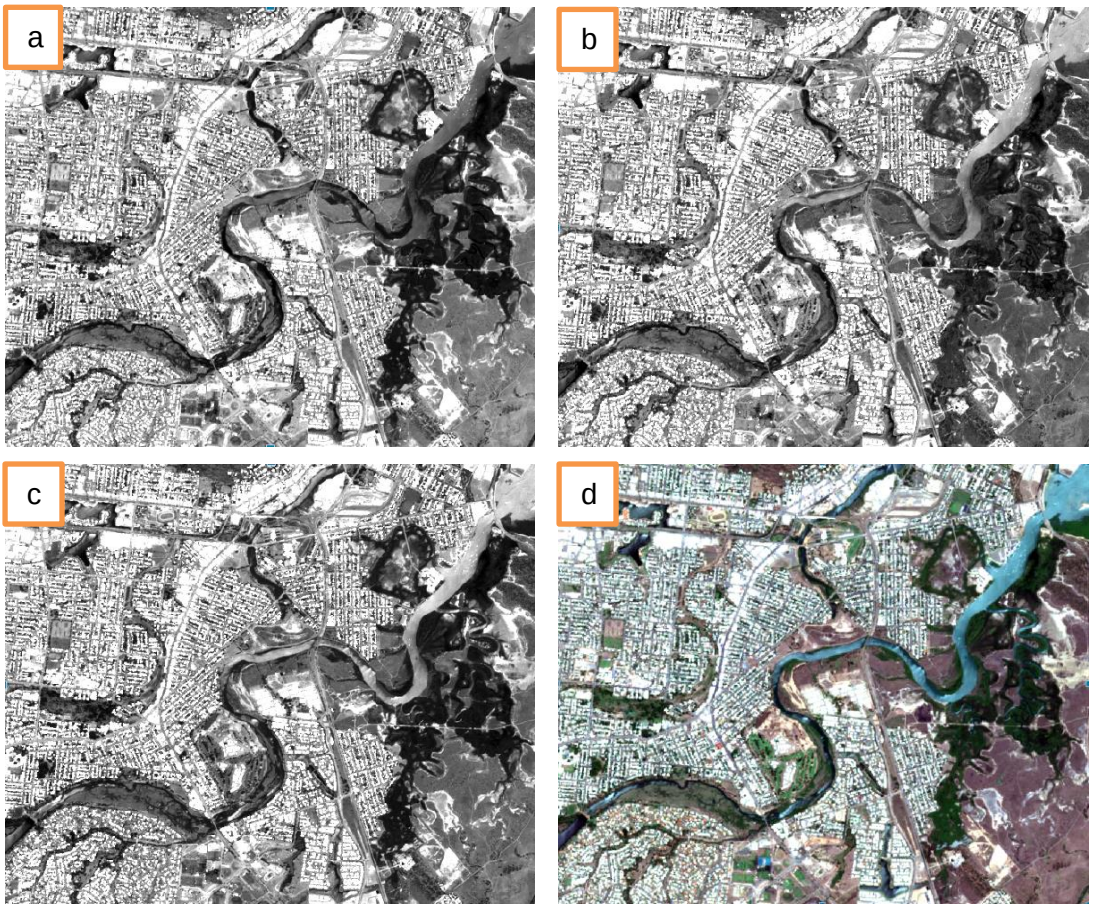


*Figure 19: The images of each spectral band and the multispectral bands; a) band 4; b) band 3; c) band 2; d) the colour composite of RGB bands 4,3,2.*

### 4.1.3 Geometric evaluation

Despite the auto-radiometric and geometric corrections of Sentinel 2 images at level 2A, further evaluation and calibration was able to provide improvements to the geometry of the images. The geometric correction produced more accurate geometry for the image with the indication of a small RMS error value. The overall RMS error for the Sentinel 2 image on 26 October (for instance) is 2.505 meters, which is less than the 10m spatial resolution of an image pixel (Table 6). Therefore, the geometry of the Sentinel image is acceptably co-registered with the reference image. The RMS values for the images were derived on 25 November, 2018 and 13 February, 2019 (Appendix F & Appendix G).

| Points | Xi (m) | Yi (m) | Xr (m) | Yr (m) | Rx (m) | Ry (m) | RMSE (m) |
|---|---|---|---|---|---|---|---|
| GCP1 | 465168.374 | 7848687.446 | 465168.994 | 7848687.903 | 0.62 | 0.457 | 0.770 |
| GCP2 | 484844.43 | 7844737.435 | 484843.423 | 7844736.433 | -1.007 | -1.002 | 1.421 |
| GCP3 | 468751.352 | 7870161.056 | 468758.336 | 7870169.445 | 6.984 | 8.389 | 10.916 |
| GCP4 | 482394.41 | 7870158.095 | 482394.203 | 7870160.012 | -0.207 | 1.917 | 1.928 |
| GCP5 | 485864.995 | 7859470.209 | 485867.502 | 7859469.468 | 2.507 | -0.741 | 2.614 |
| GCP6 | 468592.313 | 7859135.38 | 468591.877 | 7859133.419 | -0.436 | -1.961 | 2.009 |
| GCP7 | 479075.863 | 7852184.249 | 497079.085 | 7852186.283 | 3.222 | 2.034 | 3.810 |
| GCP8 | 471681.427 | 7856524.424 | 471683.5 | 7856525.394 | 2.073 | 0.97 | 2.289 |
| GCP9 | 479754.774 | 7856864.183 | 479456.341 | 7856864.246 | 1.567 | 0.063 | 1.568 |
| GCP10 | 472373.723 | 7871898.122 | 472374.71 | 7871896.259 | 0.987 | -1.863 | 2.108 |
| GCP11 | 474807.579 | 7869452.24 | 474806.296 | 7869451.275 | -1.283 | -0.965 | 1.605 |
| GCP12 | 474870.671 | 7870071.689 | 474871.594 | 7870072.84 | 0.923 | 1.151 | 1.475 |
| GCP13 | 475549.453 | 7869404.42 | 475549.918 | 7869402.384 | 0.465 | -2.036 | 2.088 |
| GCP14 | 477100.64 | 7869248.114 | 477101.02 | 7869248.176 | 0.38 | 0.062 | 0.385 |
| GCP15 | 477214.36 | 7869680.985 | 477214.616 | 7869681.041 | 0.256 | 0.056 | 0.262 |
| GCP16 | 472678.243 | 7864470.317 | 472676.112 | 7864472.59 | -2.131 | 2.273 | 3.116 |
| GCP17 | 483667.71 | 7862620.946 | 483668.845 | 7862621.06 | 1.135 | 0.114 | 1.141 |
| GCP18 | 482903.765 | 7859214.328 | 482903.566 | 7859216.654 | -0.199 | 2.326 | 2.334 |
| GCP19 | 484873.183 | 7848659.824 | 484870.5 | 7848659.165 | -2.683 | -0.659 | 2.763 |
| GCP20 | 467280.445 | 7862501.585 | 467275.736 | 7862500.19 | -4.709 | -1.395 | 4.911 |
| GCP21 | 474751.82 | 7868933.152 | 474750.528 | 7868932.451 | -1.292 | -0.701 | 1.470 |
| GCP22 | 478155.5 | 7868555.941 | 478150.302 | 7868552.282 | -5.198 | -3.659 | 6.357 |
| GCP23 | 477143.293 | 7868660.706 | 477143.196 | 7868660.675 | -0.097 | -0.031 | 0.102 |
| GCP24 | 478214.862 | 7869161.46 | 478214.701 | 7869161.3 | -0.161 | -0.16 | 0.227 |
| GCP25 | 468065.065 | 7867154.458 | 468063.353 | 7867149.821 | -1.712 | -4.637 | 4.943 |
| RMSE | | | | | | | 2.505 |

*Table 6: Geometric correction for Sentinel 2 imagery derived on 26 October, 2018.*

Where *Xi* and *Yi* represent the X and Y positions in coordinates derived from the Sentinel 2 imagery; *Xr* and *Yr* represent the X and Y positions in coordinates derived from the reference imagery; and

*Rx* and *Ry* represent the differences between each position in coordinates derived from the Sentinel 2 image and the actual value from the reference image.

### 4.1.4 Noise removal

Despite the atmospheric correction from TOA to BOA reflectance, the image still contained intercorrelated data and, hence, noise removal was applied to the Sentinel 2 images. In comparison to the image with noise, the image derived after noise removal presented a brighter, more colourful and more distinct contrast between objects such as roads, buildings, and water (Figure 20).

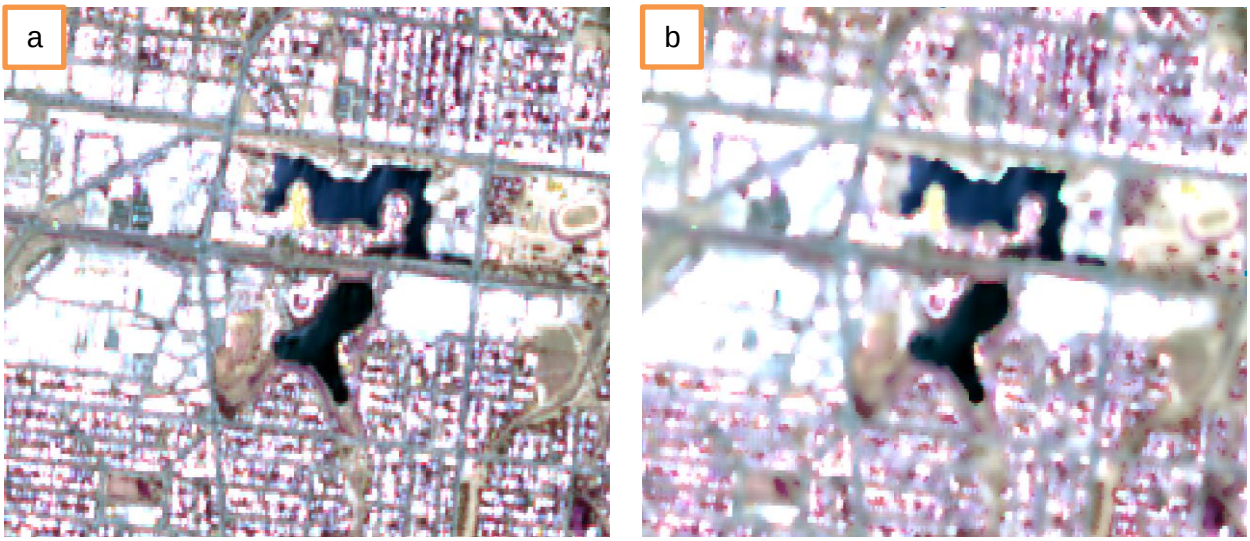


*Figure 20: A sample of Sentinel 2 image with noise and with noise removal derived on 26 October, 2018 with a colour composition of RGB bands 4, 3, 2; a) before noise removal; b) after noise removal.*

### 4.1.5 Subset image

The sub-setting image provided a satellite image of the extent of the Ross and Bohle River catchments (Figure 21). The area outside the target area of interest was cropped away and the size of the satellite image file was also reduced.

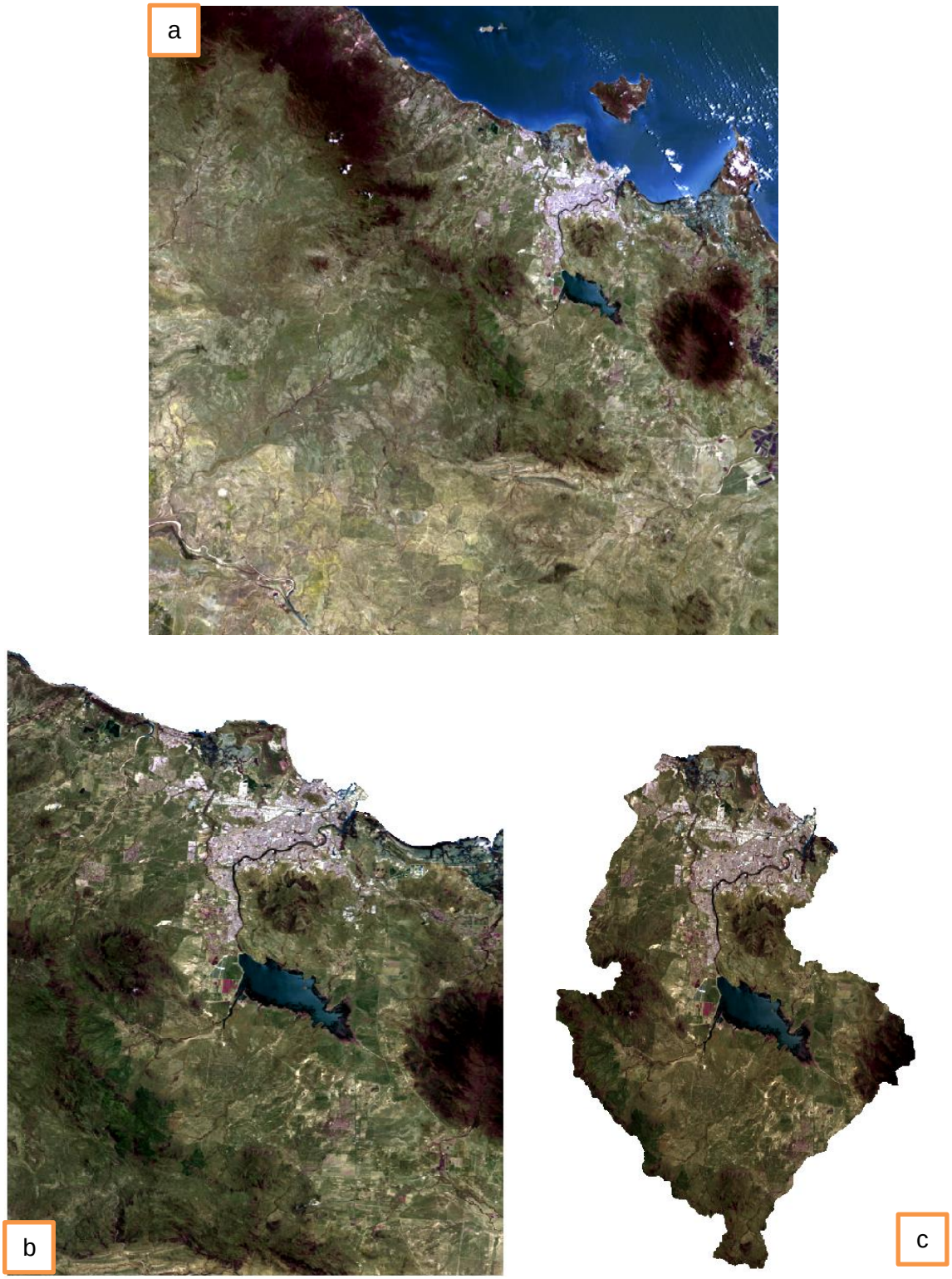


*Figure 21: Subset image; (a) whole area of the downloaded Sentinel 2 image; (b) sub-area subset for image processing after removal of the sea; (c) the subset image for the Ross and Bohle River catchments.*

## 4.2 Results from digital image processing for Sentinel 2

### 4.2.1 Spectral signature investigation

Investigating the spectral signature of water, vegetation, the airport runway, rooftops, and bare soil provided information regarding their differences and similarities (Figure 22 and 23). The spectral

reflectance of water showed a notable difference to that of rooftops, vegetation and bare soil, but was similar to the reflectance of the airport runway (Figure 22).

In the relationship between spectral reflectance of each landcover type at each spectral band, the reflectance of water indicates that the reflectance value at band 3 is higher than that at the other bands. This relationship clearly demonstrates the difference of water from other landcover types, except for the reflectance of some rooftops which present similarly to water.

This means that by relying on the spectral reflectance of all bands, this similarity can cause confusion between the water class and other landcover types, including the airport runway and some rooftops.


*Figure 22: The spectral profiles of five different landcover types derived from the Sentinel 2 image acquired on 26 October, 2018; a) spectral signature of water; b) spectral signature of vegetation; c) spectral signature of bare soil; d) spectral signature of the airport runway; e) spectral signature of rooftops.*

Apart from the spectral collection, applying an unsupervised classification with 50 different random classes presented accurately classified water bodies in classes 2, 4, and 5 (Figure 23). However, there was still some misclassification of the water class at the airport runway and in areas of shadow. This confusion corresponds to the preceding observations of the spectral profile, where there was some similarity in the spectral reflectance between the airport runway and water bodies.

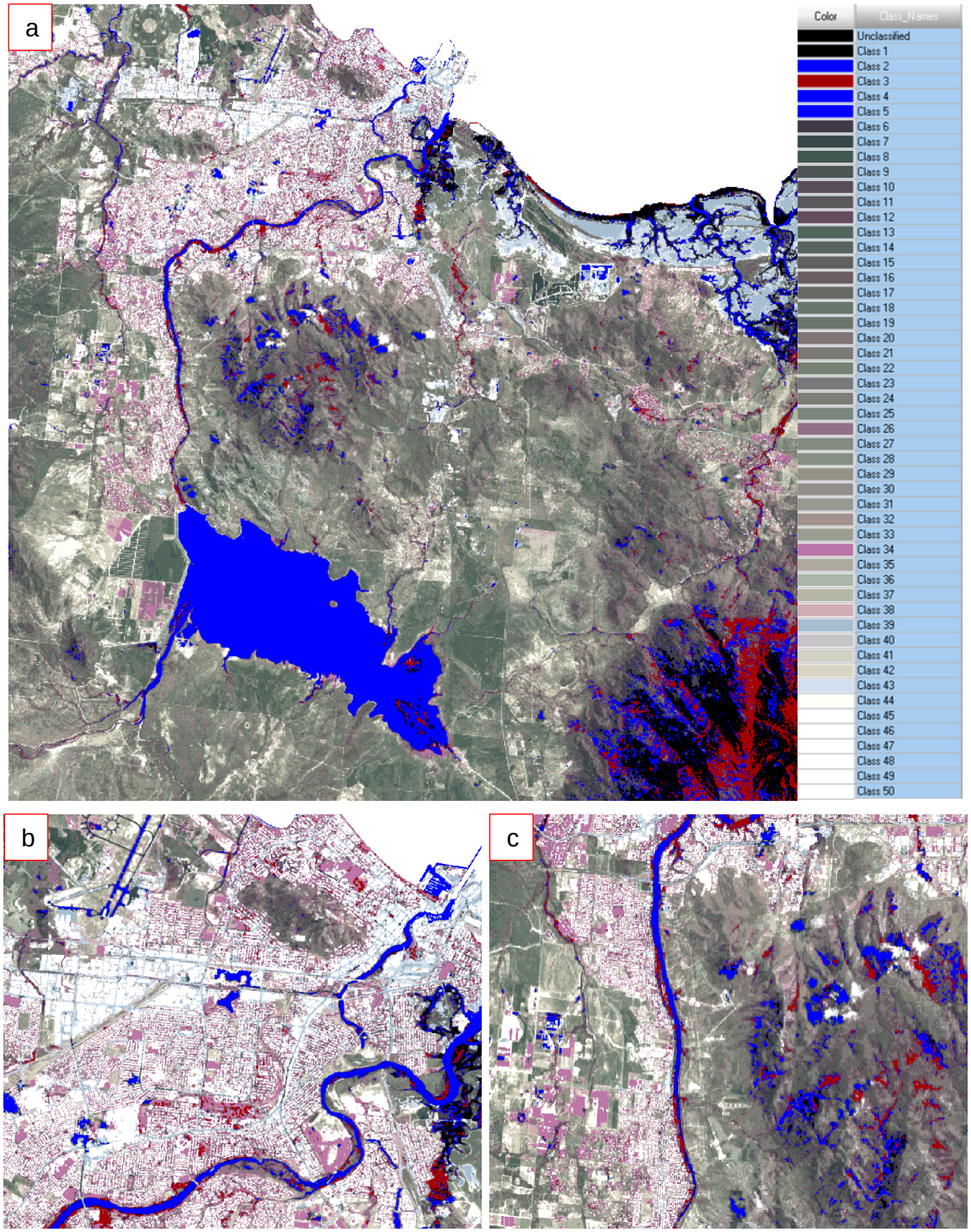


*Figure 23: An unsupervised classified image derived from Sentinel 2 image acquired on 26 October, 2018; (b) & (c) represent an enlargement of two surface areas from (a).*

### 4.2.2 Water-related index base method

The initial delineation of surface water from other landcover types was derived using different water-related index methods which included NDWI, MNDWI, and $AWEI_{nsh}$. Such methods provided greyscale images ranging from -1 to +1 (Figures 24 and 25) and approximately from -3 to +3 (Figure 26) where positive values possibly represent water bodies. As a whole, the results from the different water-related index methods indicated some misclassification of water over buildings (Figure 24, 25, 26). Applying the same threshold value with NDWI and MNDWI images demonstrated misclassification of water over other objects such as rooftops and increasingly on vegetation for the MNDWI image (Figures 24 and 25). Unlike the images from the NDWI and MNDWI methods, the $AWEI_{nsh}$ images indicated various results with different threshold values (Figure 26). While a threshold value of 0.001 yielded lower results in the classification of water, a threshold value of -0.5 provided miss- and over-classification results of water and this was even greater for a threshold value of -0.9.

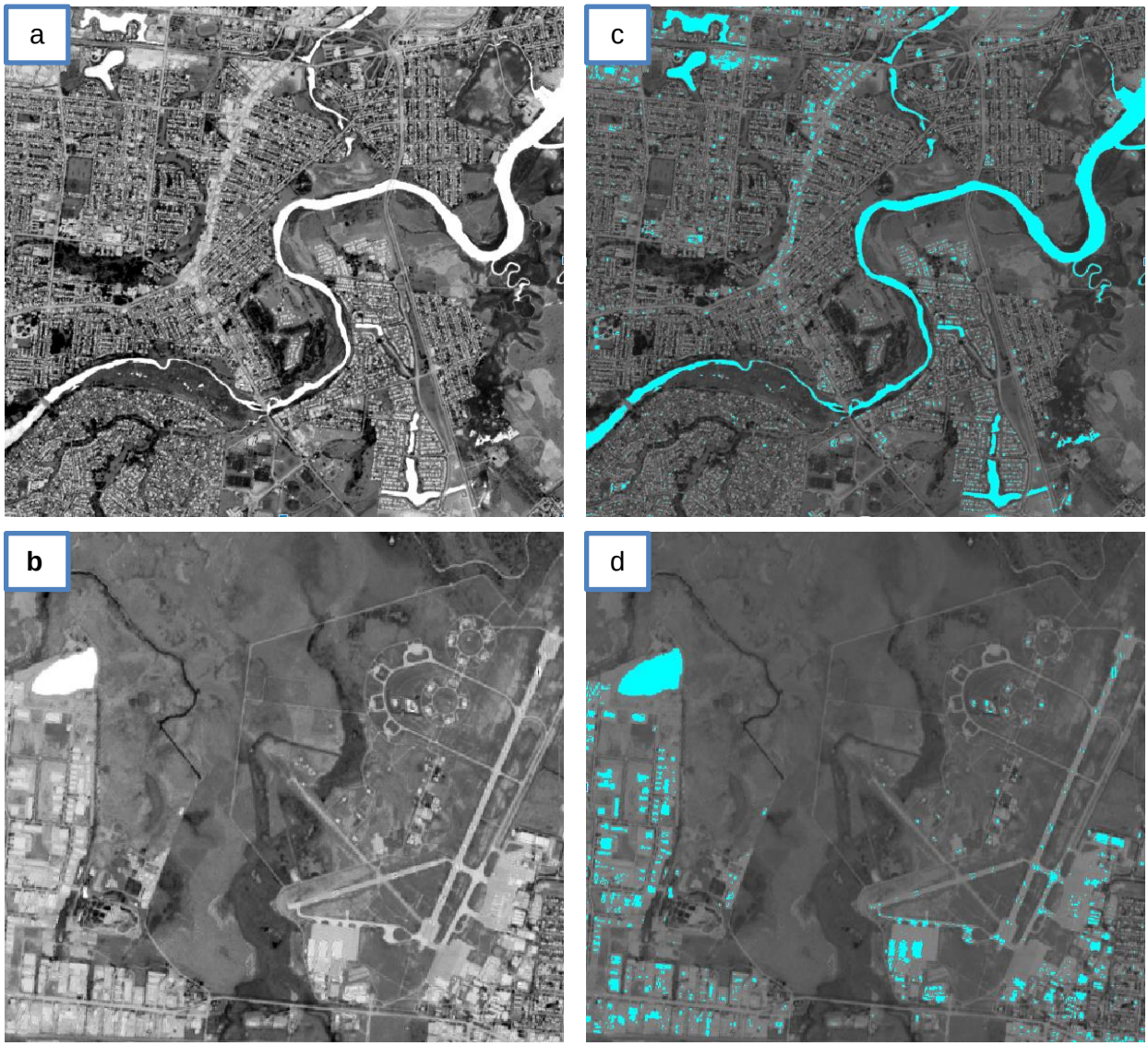


Figure 24: Results from the NDWI method; (a & b) sample of greyscale images from different areas; (c & d) sample of the threshold above 0.

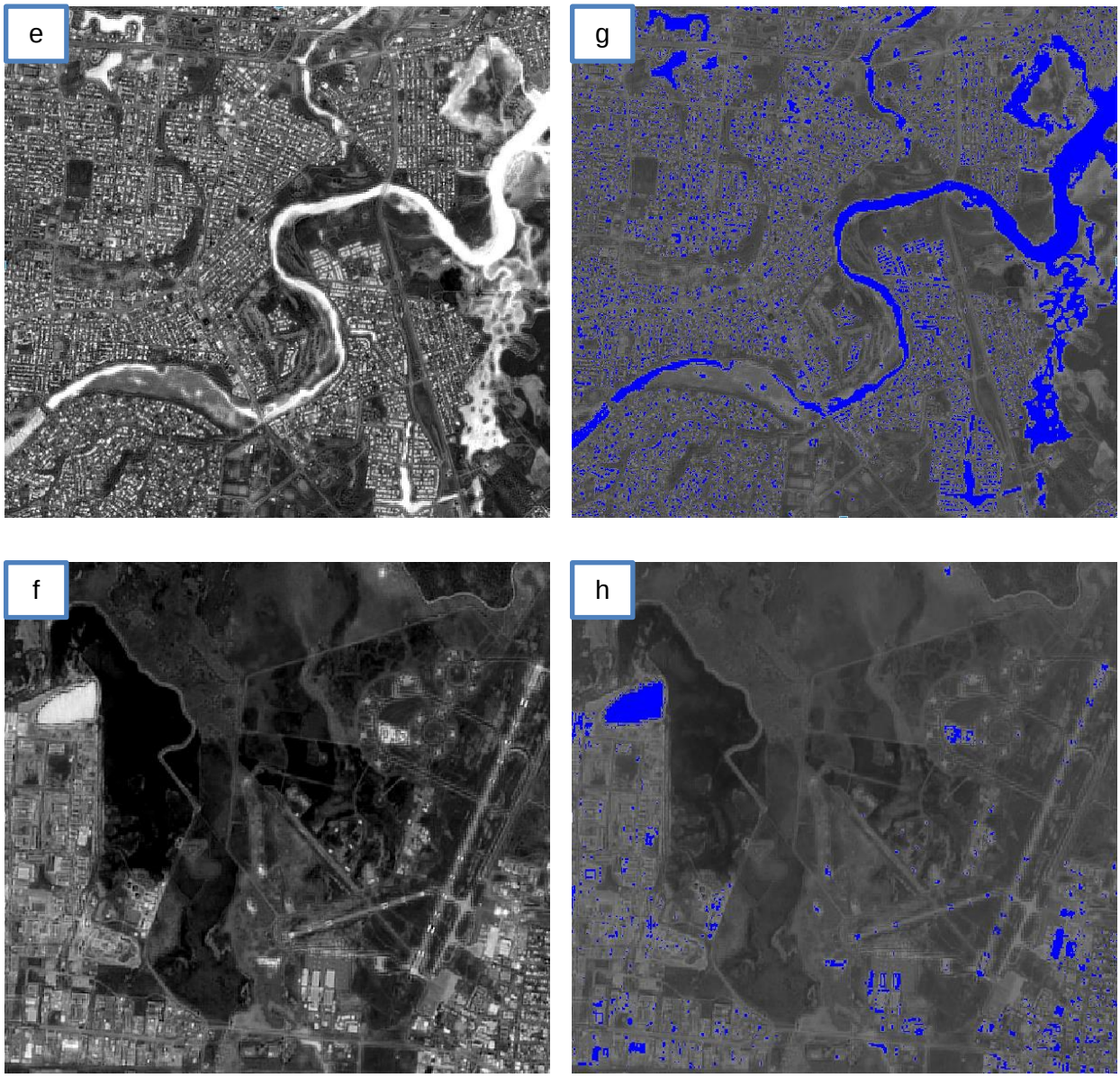


*Figure 25: Results from the MNDWI method; (e & f) sample of greyscale images from different areas; (g & h) sample of the threshold above 0.*

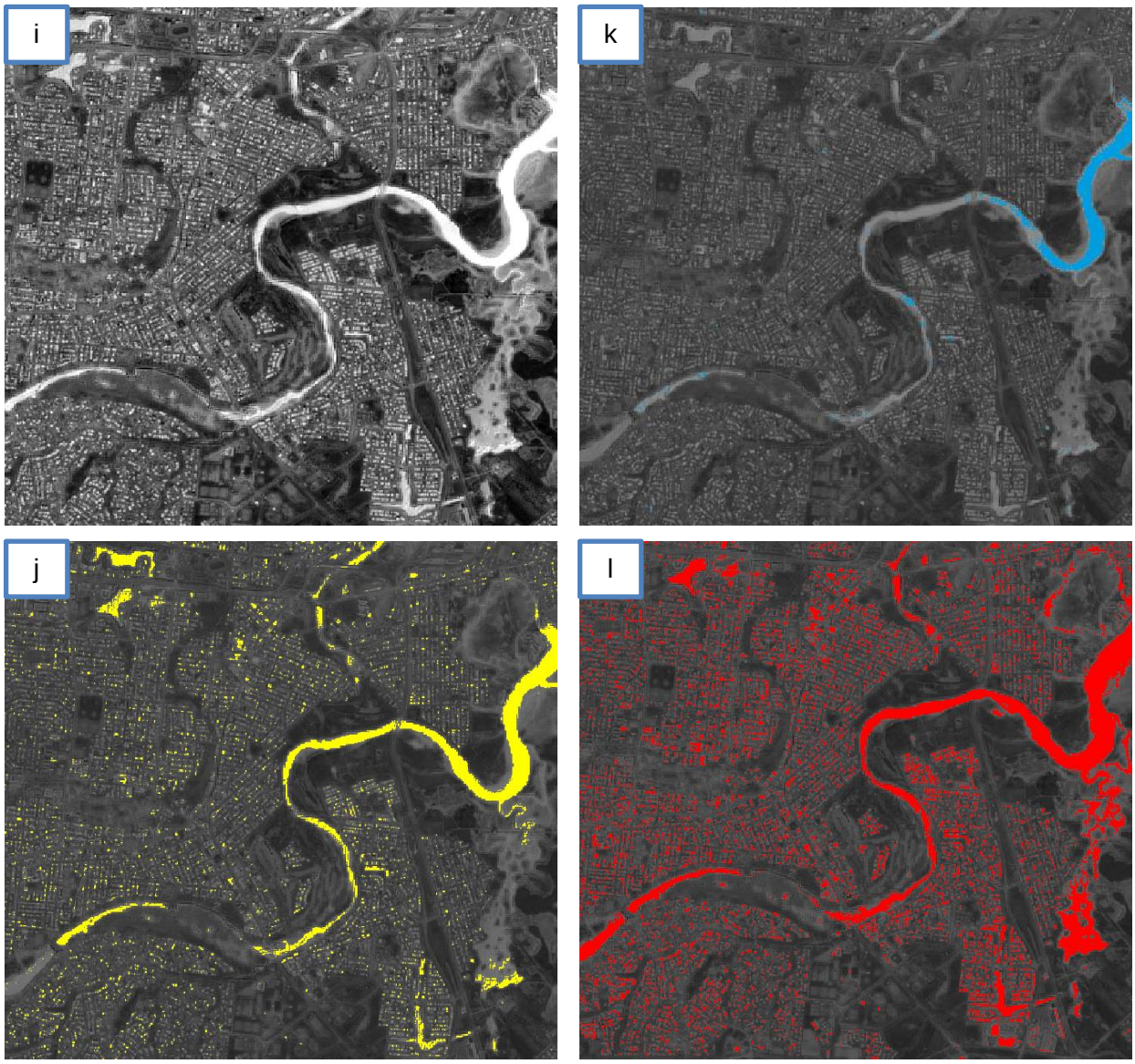


*Figure 26: Results from the $AWEI_{nsh}$ method; (i) sample of greyscale images; (j) sample of the threshold above 0.001; (k) sample of the threshold above -0.5; (l) sample of the threshold above -0.9.*

### 4.2.3 Thresholding classification

A combination of the threshold values of NDWI and $AWEI_{nsh}$ images and the threshold of the single SWIR band with a pixel value smaller than 1,000 (BOA reflectance multiplied by 10,000) provided two-class images of water and non-water with a more effective removal of any misclassifications (Figures 27 and 28). The thresholding of the NDWI image created no confusion between water bodies and non-water bodies but also presented no classification at some areas along the river and around the edges of ponds (Figure 27). The thresholding of the $AWEI_{nsh}$ image yielded better-classified results at the edges of ponds but no classification at some areas along the river and also some misclassification of water over vegetation (Figure 28).

*Figure 27: Results from the combination of the threshold of NDWI and the threshold of a single SWIR band.*

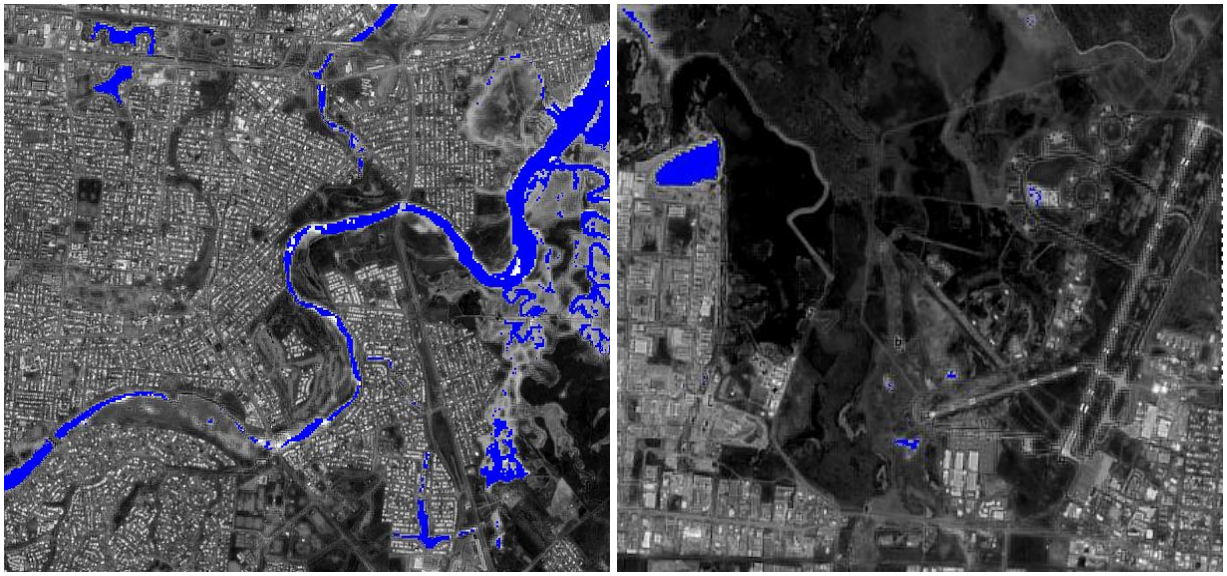

*Figure 28: Results from the combination of the threshold of $AWEI_{nsh}$ and the threshold of a single SWIR band.*

### 4.2.4 Accuracy assessment

The accuracy assessment of the water classification derived from the Sentinel 2 images, both pre- and post flood event, indicated effective correspondence with the map of surface water from WOfS (Tables 7 and 8). The classification for the pre-flood event image presented relatively high overall accuracy of 94.71% and a strong kappa value of 94.20% (Table 7). At the same time, the classification post flood event presented an acceptable rate of overall accuracy of 91.94% and a kappa value of 89.71% despite the high commission error of 14.76% (Table 8).

| | Result (%) |
|---|---|
| Overall accuracy | 94.71 |
| Omission Error | 5.29 |
| Commission Error | 6.83 |
| Kappa | 94.20 |

*Table 7: An accuracy assessment of the water classification from Sentinel 2 pre-flood conditions against the map of surface water from WOfS with a threshold of 40% water class occurring over time.*

| | Result (%) |
|---|---|
| Overall accuracy | 91.94 |
| Omission Error | 8.06 |
| Commission Error | 14.76 |
| Kappa | 89.71 |

*Table 8: An accuracy assessment of the water classification from Sentinel 2 post flood conditions against the map of surface water from WOfS with a threshold of 10% water class occurring over time.*

## 4.3 Results from Radar image pre-processing for Sentinel 1

### 4.3.1 Radiometric calibration

Radiometric correction provided a satellite image with a change in backscatter values from a physical value to a real backscatter value of the surface, in which the backscatter value of smooth surfaces was more distinguishable (Figure 30). For instance, the backscatter value of the radiometrically corrected image changed from a physical pixel value ranging from 0 to 80 to the real backscatter of the surface reflectance value ranging from -50 to 30 dB (Figure 30). The distribution of the backscatter value of the radiometrically corrected image presents a greater negative value, which means that the backscatter of smooth surfaces is more detectable.

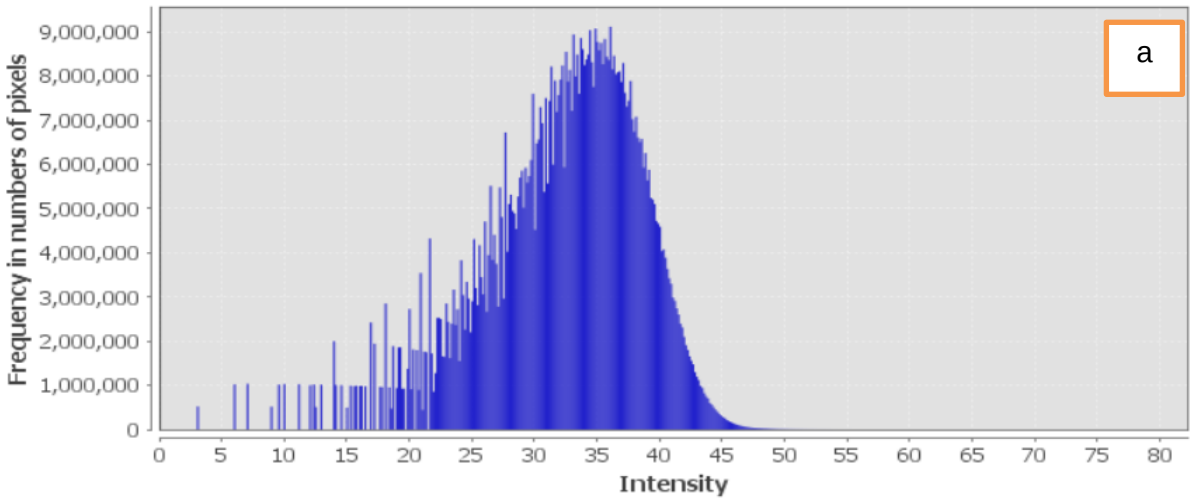

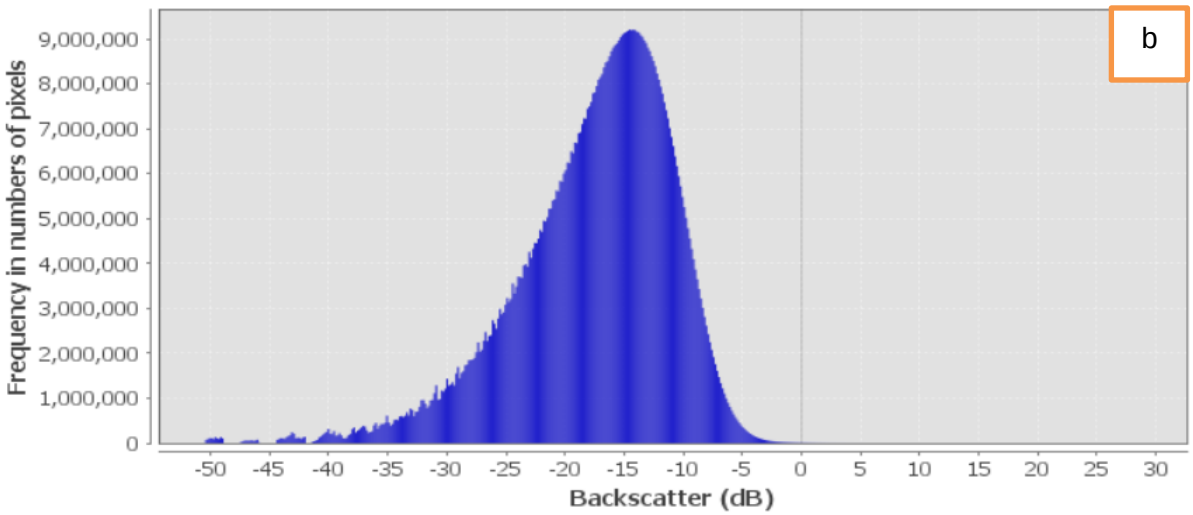


*Figure 29: A histogram for the backscatter value of the VH polarization of the image derived on 31 January, 2019; a) before radiometric calibration; b) after the calibration.*

### 4.3.2 Image de-speckle

Image de-speckling enhanced the image, revealing a better contrast between the backscatter of rough surfaces (bright colour) and that of smooth surfaces (dark colour) (Figure 30). The de-speckled image presented two distinct peaks of backscatter value - one representing smooth surfaces and the other representing rough surfaces (Figure 31).

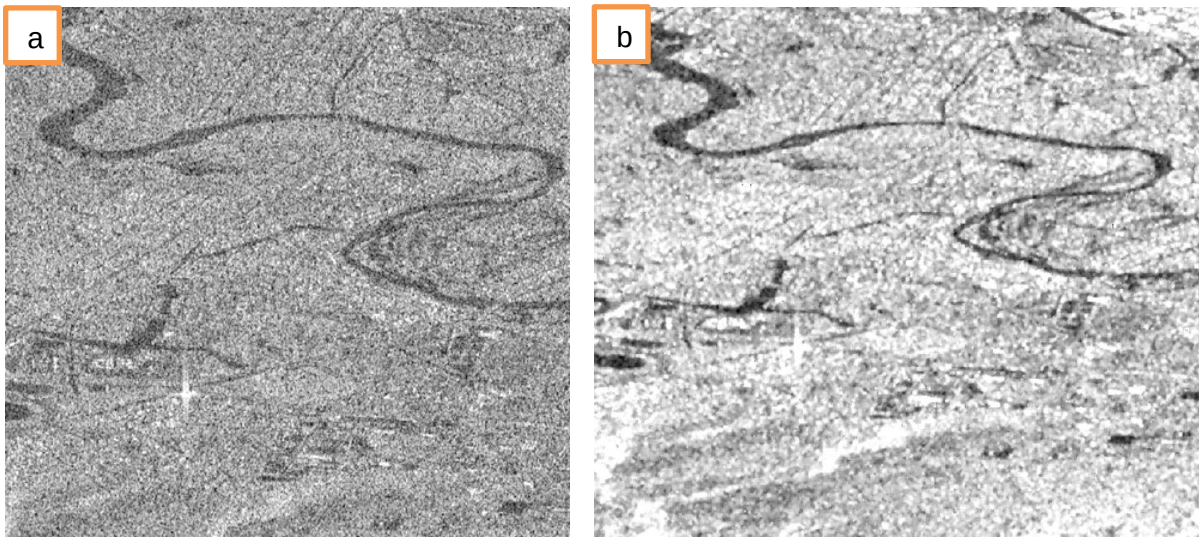


*Figure 30: A sample of image de-speckle for the VH polarization of the image derived on 31 January, 2019; a) before de-speckle; b) after de-speckle.*

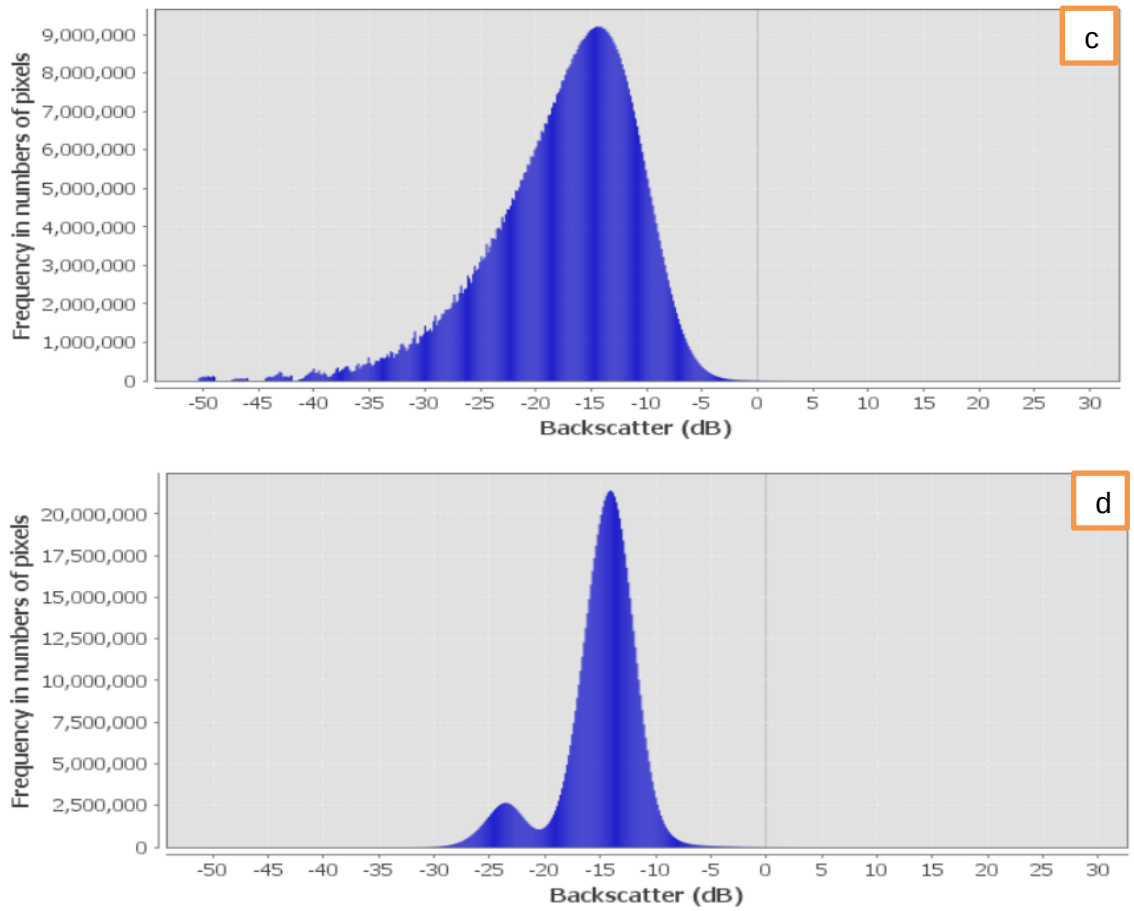


*Figure 31: A histogram for the backscatter value of the VH polarization of the image derived on 31 January, 2019; c) before speckle removal; d) after speckle removal.*

### 4.3.3 Image orthorectification

The orthorectified image reduced the geometric distortion, improving it from slant range geometry to ground range geometry (Figure 32).

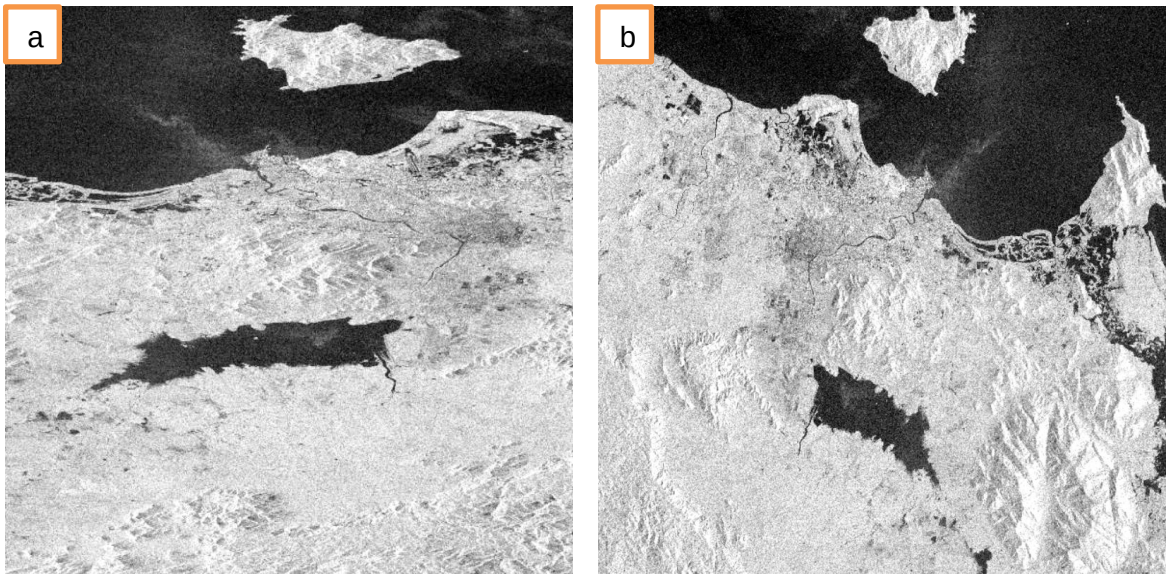


*Figure 32: Orthorectification of Sentinel 1 image acquired on 31 January, 2019 with VH polarization; a) before orthorectification; b) before orthorectification.*

### 4.3.4 Geometric evaluation

A further adjustment of the 2D ortho-rectification provided further correction of the image's geometry. For instance, the overall RMS error of the Sentinel 1 image derived on 27 October, 2018 was 4.740 m, which was less than a pixel size of the image.

| Points | Xi (m) | Yi (m) | Xr (m) | Yr (m) | Rx (m) | Ry (m) | RMSE (m) |
|---|---|---|---|---|---|---|---|
| GCP1 | 471824.059 | 7870257.206 | 471821.05 | 7870258.582 | 3.009 | -1.376 | 3.308 |
| GCP2 | 482048.628 | 7869464.004 | 482043.574 | 7869469.176 | 5.054 | -5.172 | 7.231 |
| GCP3 | 483680.783 | 7862604.354 | 483683.683 | 7862603.678 | -2.9 | 0.676 | 2.978 |
| GCP4 | 478152.832 | 7868569.793 | 478150.971 | 7868572.694 | 1.861 | -2.901 | 3.446 |
| GCP5 | 482093.432 | 7869209.631 | 482093.308 | 7869207.128 | 0.124 | 2.503 | 2.506 |
| GCP6 | 477037.563 | 7866494.689 | 477042.44 | 7866498.674 | -4.877 | -3.985 | 6.298 |
| GCP7 | 472396.522 | 7851654.063 | 472392.135 | 7851654.657 | 4.387 | -0.594 | 4.427 |
| GCP8 | 470572.61 | 7850966.133 | 470578.03 | 7850965.054 | -5.42 | 1.079 | 5.526 |
| GCP9 | 472671.411 | 7864472.639 | 472666.722 | 7864473.824 | 4.689 | -1.185 | 4.837 |
| GCP10 | 478213.072 | 7869168.078 | 478218.207 | 7869162.042 | -5.135 | 6.036 | 7.925 |
| GCP11 | 478559.576 | 7866958.191 | 478552.417 | 7866955.247 | 7.159 | 2.944 | 7.740 |
| GCP12 | 474939.192 | 7866157.146 | 474940.776 | 7866156.974 | -1.584 | 0.172 | 1.594 |
| GCP13 | 477152.904 | 7868662.653 | 477162.436 | 7868661.268 | -9.532 | 1.385 | 9.632 |
| GCP14 | 477103.279 | 7867219.542 | 477099.682 | 7867220.155 | 3.597 | -0.613 | 3.649 |
| GCP15 | 471958.612 | 7852619.144 | 471956.798 | 7852619.804 | 1.814 | -0.66 | 1.931 |
| GCP16 | 470680.201 | 7865698.968 | 470682.447 | 7865697.277 | -2.246 | 1.691 | 2.812 |
| RMSE | | | | | | | 4.740 |

*Table 9: Geometric correction for Sentinel 1 imagery derived on 27 October, 2018.*

## 4.4 Results for digital Image processing for Sentinel 1

### 4.4.1 Polarisation investigation

An investigation into polarisation yielded information regarding the difference in the backscatter value of smooth surfaces derived from the different dates. While the backscatter of the possibly constant smooth surface derived from the average-polarisations of the images acquired from different dates presented backscatter differences lying within +/- 1 dB, both VV and VH demonstrated backscatter differences ranging from one dB up to 3 dB (Table 10). This indicated that the backscatter derived from the average-polarisations is more constant than for other polarisations.

| Image Acquisition Date | Time | Pass Direction | VV (dB) | VH (dB) | Average VV&VH (dB) | Remark |
|---|---|---|---|---|---|---|
| 27-10-18 | 5:44 | Descending | -21.586 | -23.558 | -22.572 | Runway |
| 31-1-19 | 5:44 | Descending | -20.947 | -25.190 | -23.069 | Runway |
| 6-2-19 | 5:43 | Descending | -22.441 | -21.600 | -22.020 | Runway |

| | | | | | | |
|---|---|---|---|---|---|---|
| 6-2-19 | 18:43 | Ascending | -21.459 | -25.264 | -22.279 | Runway |
| 12-2-19 | 5:44 | Descending | -18.140 | -24.226 | -21.183 | Runway |
| 12-2-19 | 18:42 | Ascending | -19.911 | -22.415 | -21.163 | Runway |

*Table 10: Example of the variation of the backscatter value at the runway (a smooth surface) using different polarizations and the result from the average of both polarizations.*

### 4.4.2 Density slicing

Density slicing provided a classification of smooth and rough surfaces where smooth surfaces were considered to be potential water bodies (Figures 33, 34, and 35). Different density slicing (threshold) values resulted in more or fewer smooth surfaces being classified. The higher the threshold value, the more pixels were classified as smooth surfaces (Figure 33); and the lower the threshold value, the less pixels were classified as smooth surfaces (Figures 34 and 35).

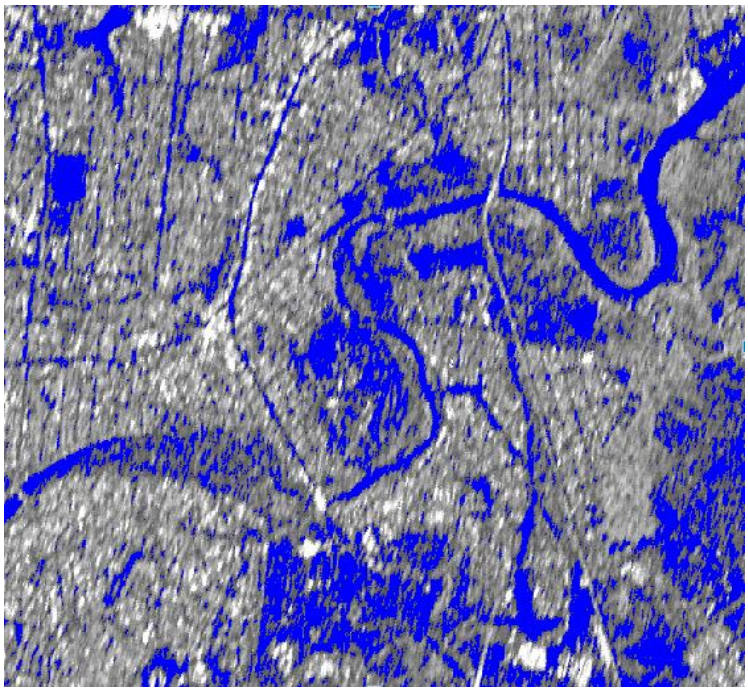

*Figure 33: The threshold value of -1dB from the mean value of the backscatter derived from the average-polarization image acquired on 27 October, 2018.*

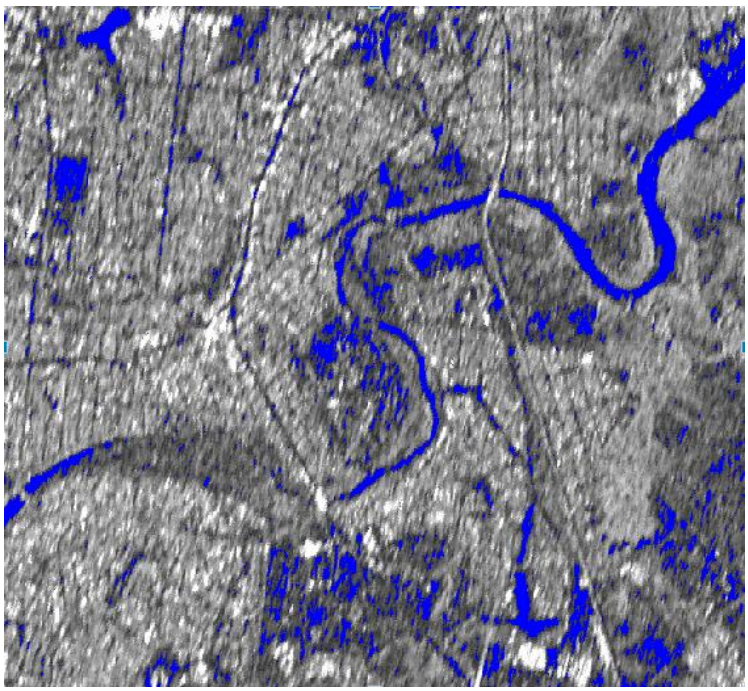

*Figure 34: The threshold value of -3dB from the mean value of the backscatter derived from the average-polarization image acquired on 27 October, 2018.*

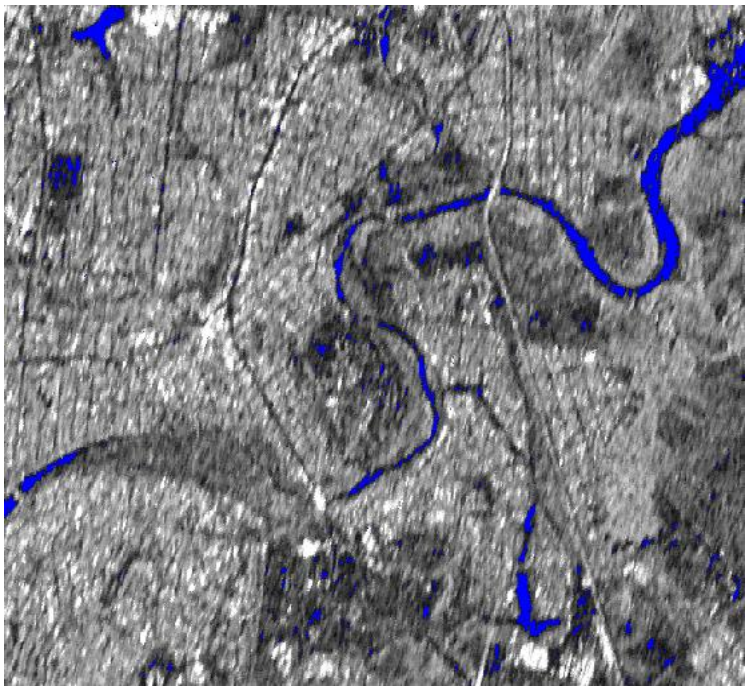

*Figure 35: The threshold value of -5dB from the mean value of the backscatter derived from the average-polarization image acquired on 27 October, 2018.*

### 4.4.3 Verification of the classification

The verification of the classification provided numerical results of classification accuracy in reference to the base-line data (Tables 11 and 12). The results of the classification of both pre-flood and post flood events demonstrated the best overall accuracy is at a threshold value of -1dB, but this presented significant commission error. While the accuracy assessment of the threshold value of -5dB from the mean presented the best commission error, it still offered acceptable overall accuracy.

The overall accuracy of both pre-flood and post flood events at the threshold value of -5dB is 0.90 and the kappa value higher than 0.7 indicated high confidence in the accuracy of the data when compared to the other values.

| | -1dB | -2dB | -3dB | -4dB | -5dB |
|---|---|---|---|---|---|
| Overall accuracy | 0.98 | 0.97 | 0.96 | 0.94 | 0.90 |
| Omission Error | 0.02 | 0.03 | 0.04 | 0.06 | 0.10 |
| Commission Error | 10.26 | 6.69 | 3.89 | 1.99 | 0.86 |
| Kappa | 0.41 | 0.48 | 0.55 | 0.63 | 0.73 |

*Table 11: An accuracy assessment of the water classification from the Sentinel 1 image derived on 27 October, 2018 (pre-flood event) against the classification from the corresponding Sentinel 2 image derived on 26 October, 2018 (dry conditions).*

| | -1dB | -2dB | -3dB | -4dB | -5dB |
|---|---|---|---|---|---|
| Overall accuracy | 0.97 | 0.95 | 0.94 | 0.92 | 0.90 |
| Omission Error | 0.03 | 0.05 | 0.06 | 0.08 | 0.10 |
| Commission Error | 5.26 | 2.76 | 1.31 | 0.60 | 0.28 |
| Kappa | 0.48 | 0.58 | 0.68 | 0.78 | 0.84 |

*Table 12: An accuracy assessment of the water classification from the Sentinel 1 image derived on 12 February, 2019 (post-flood event) against the classification from the corresponding Sentinel 2 image derived on 13 February, 2019 (wet conditions).*

Where the numbers of -1dB through to -5dB represents a range of dB negatively from the mean.

### 4.4.4 Change detection

Change detection revealed the extent of classified pixels which changed from a rough surface to a smooth surface. For example, the mapped area in blue depicts a change which occurred at the Ross River Dam, accounting for the change in land that was flooded (Figure 36).

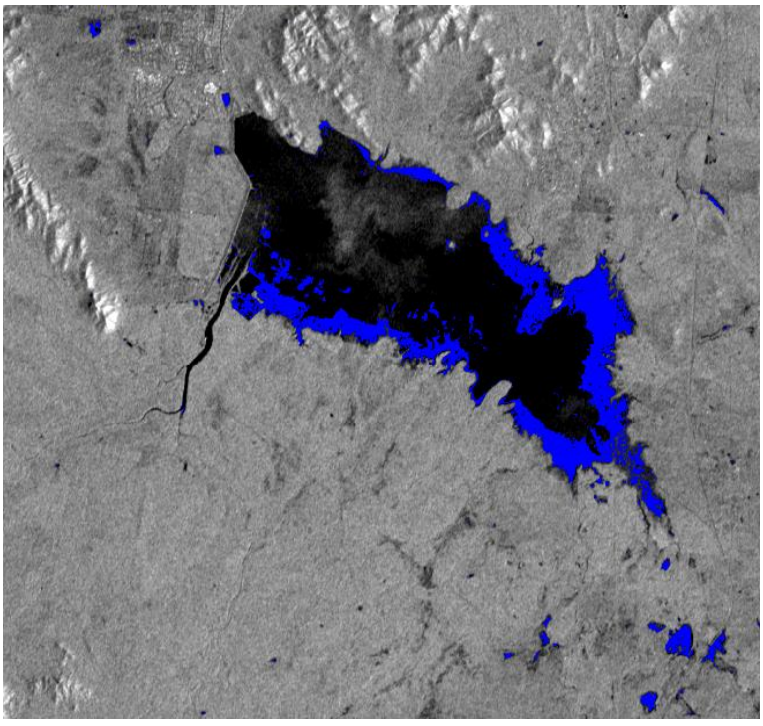

*Figure 36: Change detection overlays on the Radar image derived on 31 January, 2019.*

## 4.5 Results for image post processing

### 4.5.1 Filtering misclassification from Sentinel 1 images

By using data such as a slope raster value, the misclassification over hilly areas was removed from the classified image resulting in a more accurate classification (Figure 37).

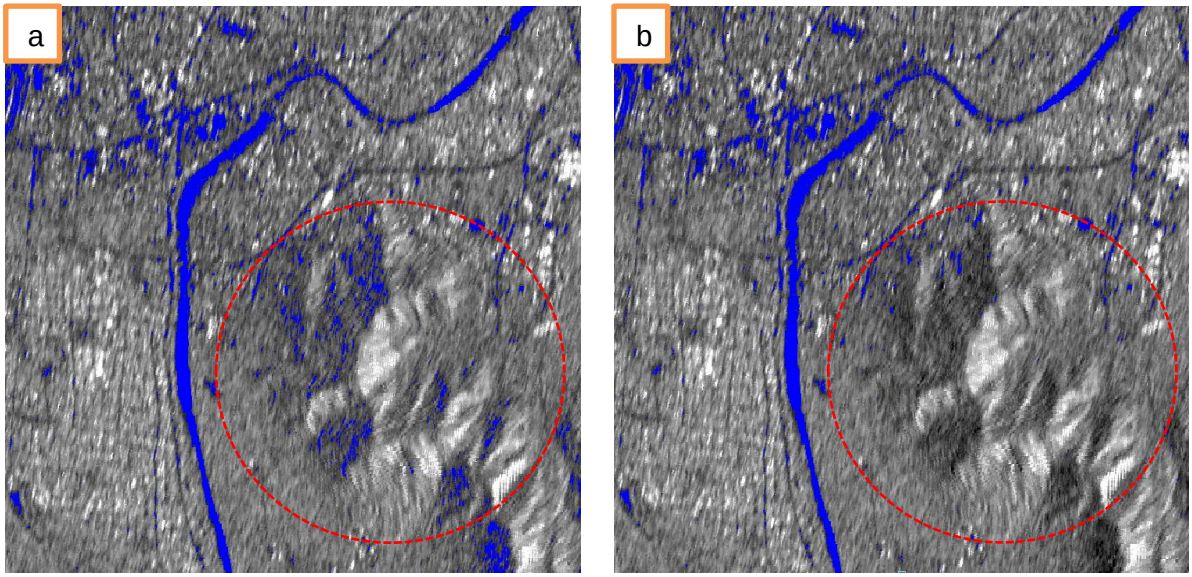


*Figure 37: Filtered classification of flood extent overlays on the Radar image derived on 31 January, 2019; a) before filter; b) after filter.*

*Note: the red circle was added to focus attention on the misclassification over hilly areas before the filter was applied.*

### 4.5.2 Re-assessing the accuracy of water extent classification from Sentinel 1 images

After filtering out the misclassifications, a re-assessment of the accuracy provided numerical evidence indicating greater confidence for the classification derived from a threshold value of -5dB from the mean (Table 13). In comparison to the information provided in section 4.4.3, the results of the re-assessment indicated the filtered misclassification results (Table 13) were slightly better than the first classification (section 4.4.3, Table 12), especially for the decrease in the commission error and the increase in the kappa value.

| | Result |
|---|---|
| Overall accuracy | 0.90 |
| Omission Error | 0.10 |
| Commission Error | 0.21 |
| Kappa | 0.87 |

*Table 13: An accuracy assessment of the water classification from the Sentinel 1 image derived on 12 February, 2019 (post-flood event) after filtering against the classification from the corresponding Sentinel 2 image derived on 13 February, 2019 (wet conditions).*

### 4.5.3 Generating maps of water classification

The map of the water extent in dry conditions (pre-flood) derived from the Sentinel 2 images (Appendix H) demonstrates where there is no water and where there are possibly permanent bodies of water, including the Ross River Dam area, along the natural rivers, and at manmade ponds. The map of the water extent during wet conditions (post flood) derived from the Sentinel 2 images (Appendix I) presented the existing water bodies which were detected in the images of dry conditions, the occurrence of new bodies of water as well as the expansion of the water extent at some areas such as the Ross River Dam, downstream of the Ross River Dam, and in the wetlands in the North-West area of the image. Similarly, the maps of the flood extent (during the flood) derived from the Sentinel 1 images (Appendixes J, K, and L) indicate a possible increase in the occurrence of water bodies at the Ross River Dam area, along creeks and rivers, in the wetland and at residential areas. The maps of the extent of water for the post flood event (Appendixes M and N) show a decrease in the water extent along the rivers and its disappearance around residential areas. These maps presented a change in the occurrence of water bodies over the specific time period, across the Ross and Bohle River catchments.

## 4.6 Comparison of potential flood extent maps

Within the areas of the map of potential inundation published by Townsville City Council, which covers mostly the Ross River (lower) catchment (Appendix D), the comparison with the flood extent derived from Sentinel 1 images (Appendixes J, K, and L) presented a high correspondence of water occurrence along Ross River. While the inundation map presented a large water extent downstream from Apline Weir with flooding spreading around Gordon and Ross Creeks, the maps of the flood extent partially agree with a number of the pixels, showing there was indeed the occurrence of surface water in such areas. At the same time, the maps of the flood extent derived from Sentinel 1 indicated some differences of the occurrence of water extent along the foothills of the hilly area (further south of the inundated map) and the non-existence of water extent around the central east area (based on the inundated map).

# CHAPTER FIVE: DISCUSSIONS AND LIMITATIONS

This study was guided by the research questions and objectives presented on page 4. This Chapter focuses on observations of the key findings in relation to the research questions and the stated aim.

## 5.1 Possibility of Sentinel 2 MSI imagery for providing water extent maps for urban areas

### 5.1.1 Promising points for classification

The results from the processing of the Sentinel 2 image clearly demonstrate that Sentinel 2 MSI imagery provides a satisfactory opportunity to separate water class from other types of landcover. Sentinel 2 imagery contains relatively rich spectral information about objects which provides an advantage in delineating water. The spectral reflectance of water is low in the NIR and SWIR wavelengths, especially for the latter as shown in Figure 22 (section 4.2.1). In contrast, most objects present higher reflectance in such wavelengths (Xie et al. 2016). The unique spectral reflectance characteristic of water makes the water-related index, when used in conjunction with grey scale thresholding methods, more efficient to classify water extent in clear and deep water. Furthermore, this is done using less complex and inexpensive procedures than with multi-spectral image classification methods, even though water-related index methods use fewer spectral bands to distinguish between land and water classes when compared to other classifier methods, like supervised and unsupervised. Floodwater with significant sediment loads can lead to some difficulties when using water indices (Doxaran et al. 2002; Shi & Wang 2014). However, based upon the accuracy assessment, a single date Sentinel 2 image contains enough spectral information to provide surface water extent (permanent water) during dry conditions and wet conditions (post flood event), providing strong agreement with the map of surface water derived from WOfS (Table 7 and Table 8 in section 4.2.4 respectively).

However, despite the strong agreement with the map of surface water derived from WOfS, some omission and commission errors are noticeable. These differences help quantify the errors of under - and over - classification derived from the image in comparison to the reference data (as shown in section 4.2.4). Nevertheless, some commission error in Sentinel 2 imagery classification satisfactorily classified water bodies when compared visually to the higher spatial resolution of the Aerial Base Image provided by Google Earth Engine (2019). Although the map of surface water derived from WOfS used a large time-series of Landsat imagery that reliably depicted the surface water extent over a long time period (more than 40 years), the 30 m lower spatial resolution and 16-day, low-temporal resolution yielded some under-classification of water bodies whose sizes were smaller than that of the spatial resolution (Mueller et al. 2016). At the same time, the commission error for wet conditions may also be due to the temporal resolution of Landsat images, which might miss a number of flood events, thereby resulting in the omission of some pixels which rarely wet

(Mueller et al. 2016). Unlike Landsat imagery, the Sentinel 2 images provide a higher spatial resolution at 10 m which allowed for a classification of water that the Landsat imagery might not detect. For instance, while a classification of water extent in the Ross River (upper) catchment appeared in Sentinel 2 satellite imagery (as shown in Appendixes H and I), they did not appear in the map of surface water derived from WOfS (as shown in Appendix C). When visually compared with the higher spatial resolution of Aerial Base image (Appendix O), the classification of water derived from the Sentinel 2 satellite images in such areas was in strong agreement.

### 5.1.2 The challenging points for classification

The use of Sentinel 2 imagery together with the proper water-related index methods (NDWI, for instance) can offer acceptable water detection but still present some confounding issues, while the lack of clear sky observations during a flood event is the main challenge. It is common that weather conditions and complex landcover types often create some challenges for classification (Doxaran et al. 2002). Sentinel 2 MSI satellite imagery has no ability to sense land surface during cloudy days, which results in the loss of necessary data (Xie et al. 2016). For the flood investigated in this research, five main observations on 1$^{st}$, 2$^{nd}$, 3$^{rd}$, 4$^{th}$ and 5$^{th}$ February 2019 were missed due to cloud cover. Complex landcover types in urban areas can contribute to spectral confusion with dark objects, for instance, by providing similar spectral reflectance to that of water bodies (Yang et al. 2017). In urban areas, Sentinel 2 imagery presents notable difficulty in delineating narrow channels and small ponds due to the lower spatial resolution when compared with the size of the water bodies and their surrounding objects such as buildings and vegetation. This can be seen in Appendix H where some water in small creeks was missed.

Apart from this, a selection of spectral bands used in the water-related index methods yield various trade-offs between the different methods (Li et al. 2013). When analysing shallow water with some vegetation and turbidity present, NIR bands can result in under-classified water bodies while increasing the infrared wavelength to SWIR wavelengths can result in the misclassification of vegetation as water bodies (Doxaran et al. 2002; Shi & Wang 2014). For instance, after setting an appropriate threshold value for NDWI (using green and NIR bands), some water pixels were not included in the classification as shown in Figure 24 where there was water in Ross River (downstream from Aplins Weir), but this water was not covered in the classification. At the same time, an appropriate threshold of MNDWI and $AWEI_{nsh}$ resulted in some vegetation being classified as water. This can be seen in Figures 25 and 26, where there was vegetation near the mouth of Ross River, but it was classified as water. This means that although the water-related index methods provided highly accurate results for surface water detection, selecting each of the water indices was challenging and depended on the characteristics of the study area.

## 5.2 Possibility of Sentinel 1 Radar imagery for providing flood extent maps for urban areas

### 5.2.1 Promising points for classification

The classification of Sentinel 1 Radar imagery provided reasonable results in delineating smooth from rough surfaces using the simple method of density slicing in conjunction with a change detection method. Similarly to the MSI imagery, the characteristic of open water backscatter is relatively low during calm, windless conditions which enables water, a distinctively smooth surface, to be classified in SAR imagery (Brisco et al. 2009). More importantly, Sentinel 1 SAR imagery experiences no restrictions due to weather conditions like cloud cover, permitting water to be classified even during severe weather conditions that cause flooding (Giustarini et al. 2013).

In the case of a flooding event, the change in medium backscatter values from rough surfaces to the lower backscatter values of flooded surfaces was addressed effectively as the land became inundated. The twin satellites of Sentinel 1A and 1B with the temporal resolution of a 6-day revisit time provided the opportunity to monitor the flood extent by using pre-, during, and post flood event images. Due to the availability of Sentinel 1 imagery that corresponded to the ten days of intense and continuous rainfall, which led to the flash flood of Townsville city, the classifications of the flood extent were reasonably generated with a 6-day gap and effectively described for all the pre-, during, and post flood events. However, a shorter time gap between images would have been preferable.

In terms of polarisation, Sentinel 1 Radar imagery provided the dual polarisation of VV and VH, which allowed for a better detection of the flood extent by using the average of both polarisations rather than just a single polarisation. During a flood event, especially one caused by heavy rainfall or storms, windy conditions can cause turbulence on the surface of the water and this can result in higher backscatter (Henry et al. 2006). While VV polarisation effectively detected the body of open water, it is sensitive to rough conditions on the water while VH polarisation presents less sensitivity to rough water surfaces (Baghdadi et al. 2001; Henry et al. 2006; Shen et al. 2013). Instead of limiting the results to those of just an individual polarisation to classify water, Sentinel 1 Radar imagery permits the opportunity to average the polarisations so that the sensitivity to surface roughness is minimised, thereby improving the final classification.

### 5.2.2 The challenging points for classification

While Sentinel 1 Radar imagery can provide data for water classification, smooth surfaces in complex urban environments result in over-classification, thereby reducing the delineation of the water class while also creating difficulties for setting the proper threshold (Martinis et al. 2019). In urban environments, roads, carparks, airport runways, and some flat rooftops present as smooth surfaces which perform similarly in specular scattering as calm water. At the same time, the areas that present as smooth surfaces like roads but are surrounded by tall buildings, can conversely

experience double-bounce scattering and this can cause the return of high energy to the Radar sensor, thereby being interpreted as a rough surface (Schlaffer et al. 2015).

Vegetation is another problem that can cause misclassification when using Sentinel 1's C band SAR. The flood extent in areas of vegetation remained unseen due to high backscatter that is caused by the tree canopy. The C band is a short Radar wavelength that offers a reduced ability to penetrate through tree canopies when compared to longer Radar wavelengths like the L and P bands (Liu et al. 2019; Xue et al. 2008) and, hence, the C band resulted in an under-classification of floodwater under trees or on the forest floor.

Apart from this, Sentinel 1 Radar medium spatial resolution (especially for 20m Azimuth resolution) yielded mixed backscatter values of objects within a pixel, which makes it challenging to delineate smooth from rough surfaces in residential areas. The medium spatial resolution of SAR imagery does not offer the ability to identify an individual backscatter, such as a double-bounce from smooth surfaces (roads) surrounded by buildings (Tsyganskaya et al. 2018). Such medium spatial resolution presents many difficulties for interpreting two different objects, especially when dealing with a complex environment such as an urban area (Grimaldi et al. 2016). Hence, a finer spatial resolution would be required in any further work of this nature (Mason et al. 2008).

More importantly, Sentinel 1 Radar imagery processing requires the integration of other topographical data and this requires significant time to implement the analysis. Shadow along the hilly areas presents a low backscatter value as in the case of smooth surfaces, which results in misclassification of the water extent. To improve the classification in such areas, the highly accurate DEM was integrated into the Radar image processing, otherwise such sloping areas would be classified as inundated with water. Moreover, image pre-processing in particular was very time-consuming and required a significant amount of effort to make these images ready for analysis.

The 6-day temporal resolution of twin Sentinel 1A and 1B Radar satellite imagery is insufficient to provide a satisfactory degree of information considering the time constraints. Although the temporal resolution of Sentinel 1 Radar imagery provided an opportunity to acquire satellite imagery for pre-, during, and post flood event every six days, some important dates were still missed. For example, the major flash flood that occurred in Townsville along Ross River started on the 2$^{nd}$ and continued through the 3$^{rd}$ and the 4$^{th}$ of February, 2019 (BMT 2019), but there were no satellite images available on these days. The lack of acquisition of such images resulted in the omission of significant information necessary for comparison with the map of the potential flood depths in Townsville.

## 5.3 Differences and similarities between flood extent maps from satellite images versus flood modelling

The comparison of the flood extent maps derived from Sentinel 1 satellite imagery with the map of potential flood depth in Townsville showed partial similarities along the river and bodies of open

water, particularly for areas predicted by the flood modelling to be greater than 2m in depth. Radar satellite imagery can provide an acceptable and reliable result of water classification, especially for open water bodies (Brisco et al. 2009). The imagery corresponded accurately with the predicted water depths and water extent along the channel, particularly downstream where the land is less steep (Peña & Nardi 2018).

Despite the similarities, there were still differences between the flood extent classification and the flood map for Townsville, with these differences occurring mostly in the residential areas and along the foot of the hilly areas. This could be due to a number of factors, including a type of scenario model simulation applied in the model and the challenges of the classifications themselves. Different scenarios of the flood modelling require different inputs which can result in different predictions (Bales & Wagner 2009). When generating flood maps, for instance, if the assumption of a steady flow rate used in a flood modelling is set at a low flow rate, the prediction of inundation will be less affected than the one modelled with high flows (Bales & Wagner 2009). While the map of potential flood depth of Townsville (Appendix D) was generated based on the assumption of water flowing at a rate of 2,000 $m^3/s$, the actual water flow rate on 31 January and 6 February 2019 (BMT 2019), the dates that the satellite imagery was used for classifying the flood extent was lower than that assumed for the map of potential flood depth for Townsville. Hence, it is possible that the areas showing inundation in the map of the potential flood depth of Townsville were not reflected in the flood extent maps. More importantly, the classifications of the flood extent derived on 31 January and 6 February, 2019 were not addressed as major flooding, since major flooding occurred along the Ross River throughout 2$^{nd}$, 3$^{rd}$, and 4$^{th}$ February, 2019. Hence, it is also possible that the areas showing inundation in the map of the potential flood depth of Townsville might be detected if there was satellite observation data during those days.

Regardless of the comparison between the flood extent maps derived from the satellite image and the map of potential flood depth for Townsville (for the Ross River lower catchment area), the flood extent maps derived from the Sentinel 1 Radar satellite images showed flooding ( Appendixes J, K, and L) in the upper Bohle River catchment (in the areas of Gumlow, Kelso, and Ras Mussen suburbs), the residential areas (in the areas of Condon, Thuringowa Central, and Kirwan suburbs), and the low lying areas north east of Townsville airport. However, because this research could not access GIS format of the flood modelling that covers the Bohle River catchment, and because there was no published map of the potential flood depth for the area, any further comparison could not be implemented.

Although it was challenging for the Radar image to detect smooth surfaces, as mentioned in the previous section (section 5.2.2), the image could contribute to identifying differences between the flood extent maps and the map of the potential flood depth for Townsville. Due to the lack of

appropriate data relating to flood modelling, a quantitative analysis and a more in-depth investigation was not conducted and, hence, future work is suggested for further comparisons.

## 5.4 Key limitations

Research requires time to analyse and understand the related issues. Due to time constraints, it was not possible to cover all the potential research experiments and some other limitations did occur in the research. Hence, the overall outcome of the research may be improved upon in future research.

### 5.4.1 Lack of free availability of high-resolution satellite imagery

Sentinel 2 imagery is currently the highest spatial and spectral resolution that is freely available. However, the classification still resulted in some water being misclassified. There are other satellite imagery that provide higher spatial and temporal resolutions (Planet, IKONOS, GeoEye etc) or a higher spectral resolution (World View 3, ASTER etc) which could contribute to more accurate classifications. However, such commercial sensors are expensive for large areas of coverage and are unaffordable for the researcher. Although, Planet satellite images may be freely available, for research purposes, it still costs money for non-research purposes.

### 5.4.2 Lack of free availability of longer wavelength Radar satellite imagery

Sentinel 1 provides the only dual polarisation VV and VH SAR imagery which is freely available. Although the average of these polarisations helped improve the sensitivity of water surface detection at a certain level, it does not provide fully adequate information to help distinguish different surface objects for a more satisfactory classification, unlike the full multi-polarisations available from Radar sensors such as Radarsat 2 and ALOS PALSAR 2. Apart from this, there was a lack of observation on the dates when the major flooding occurred due to the temporal resolution of Sentinel 1 imagery, which provided results only every six days.

### 5.4.3 Lack of ground truth data

The acquisition of ground truth data is an important requirement behind remote sensing image analysis. The uncertainty of the classification requires an assessment to ensure the accuracy of the analysis. In this research, the ground truth data of the surface water and the flood extent were not physically collected or provided. Therefore, the accuracy assessment of the classifications of surface water extent and the flood extent were not estimated from the actual information of the landscape. Deriving a GIS layer from a flood model developed by Townsville City Council would have allowed further quantitative analysis of how well the classification of the flood extent from Sentinel 1 images agreed with the flood model or vice versa.

# CHAPTER SIX: CONLUSIONS AND FUTURE RESEARCH

## 6.1 Conclusion

This research was primarily conducted with the need to use freely available technology to assist in managing and mitigating the impact of flood events - one of the world's most severe naturally occurring disasters. The main aim of the research was to explore the usefulness of freely available spaceborne images (Sentinel 1 Radar) in providing satellite information for comparison with flood predictions produced by a hydrological flood model. To achieve the aim, proposed objectives including the extraction of the flood water extent using Sentinel products and examining the results of the image analysis in comparison to the map of the potential flood depths for Townsville were covered in this research.

The research in part answered the questions set and met its aims. It is suggested that water-related methods for MSI imagery and the change detection methods for SAR imagery are computationally inexpensive, require less processing time (only for MSI imagery) and provide reliable results for the water extent and flood extent classification with a degree of accuracy. Surface water detection from Sentinel 2 MSI imagery provided highly accurate results when compared to the map of the surface water extent, which was derived from multi-temporal Landsat imagery over a long time period. At the same time, the results from Sentinel 1 Radar images indicated an acceptable level of accuracy when compared to the classification of Sentinel 2 MSI images. The expectation to use the high-resolution Digital Elevation Model to improve the classification presented satisfactory results only around the hilly areas but not on the relatively flat surfaces like the city and the central area of Townsville due to its least invariant topography. The results of the classification of the flood extent, used in conjunction with the map of the potential flood depths for Townsville, presented some similarities, especially along the river and the bodies of open water, while yielding some differences in residential areas.

Despite some challenges in the detection of flood extent in urban areas when using SAR imagery, Sentinel 1 C band SAR images presented as a possibly reliable source for detecting flooded areas, particularly for the rural and undeveloped areas. The results from the research indicated that the flood extent map derived from the classification are useful for addressing the possible areas that were inundated. Hence, as a free satellite resource with a relatively high spatial and temporal resolution, it is suggested as an acceptable alternative approach to flood modelling, especially for the areas which lack ground data and where cloud obscures optical imagery. Also, some of the challenges mentioned in Chapter 5 could be improved in further research.

## 6.2 Recommendations

From the challenges and limitations that occurred during this research, some recommendations are proposed as follows:

### 6.2.1 Utilising spatial and spectral resolution

The misclassification and over-classification of surface water in urban areas and along rivers where some vegetation and turbidity are present may be improved upon by increasing to higher spatial and spectral resolutions of MSI imagery. this may be achieved by using cost-bearing satellite sources such as World View 3 imagery, for example, which uses one panchromatic band, eight multispectral bands, eight SWIR bands, and 12 CAVIS bands at a spatial resolution of 30 m for CAVIS, 3.7 m for SWIR, 1.24m multispectral, and up to 31 cm for panchromatic. A higher spatial resolution will help reduce the volume of mixed spectral reflectance or the number of objects sensed within a pixel, which at the same time will help better identify objects. A higher spectral resolution will provide a more distinct spectral signature of objects and, hence, may help in reducing the confusion between the spectral reflectance of each object.

### 6.2.2 Utilising multi bands and multi polarizations

The use of cross polarisations and longer wavelength SAR, for example S or L band, could reduce classification confusion related to water surface roughness as induced by windy conditions while also improving the ability to penetrate through tree canopies (L Band) and, hence, better detect water under tree cover as is possible, for instance, with ALOS PALSAR-2 imagery. Moreover, these applications could provide better information that may help delineate surface features. An increase in information provided by multi bands and multi polarisations may lead to a better opportunity to classify not only water and non-water classes but also other classes. In 2022, there is a possibility that The NASA-ISRO Synthetic Aperture Radar or NISAR satellite (a mission under the cooperation between the National Aeronautics and Space Administration (NASA) and the Indian Space Research Organization) will freely provide L band and S band Synthetic Aperture Radar imagery (NASA 2019). The availability of these bands' frequencies and their multi-polarisations may provide better understanding about flood hazards, offering better classifications of flood extent in future research.

# APPENDICES

## Appendix A: Map of the study area

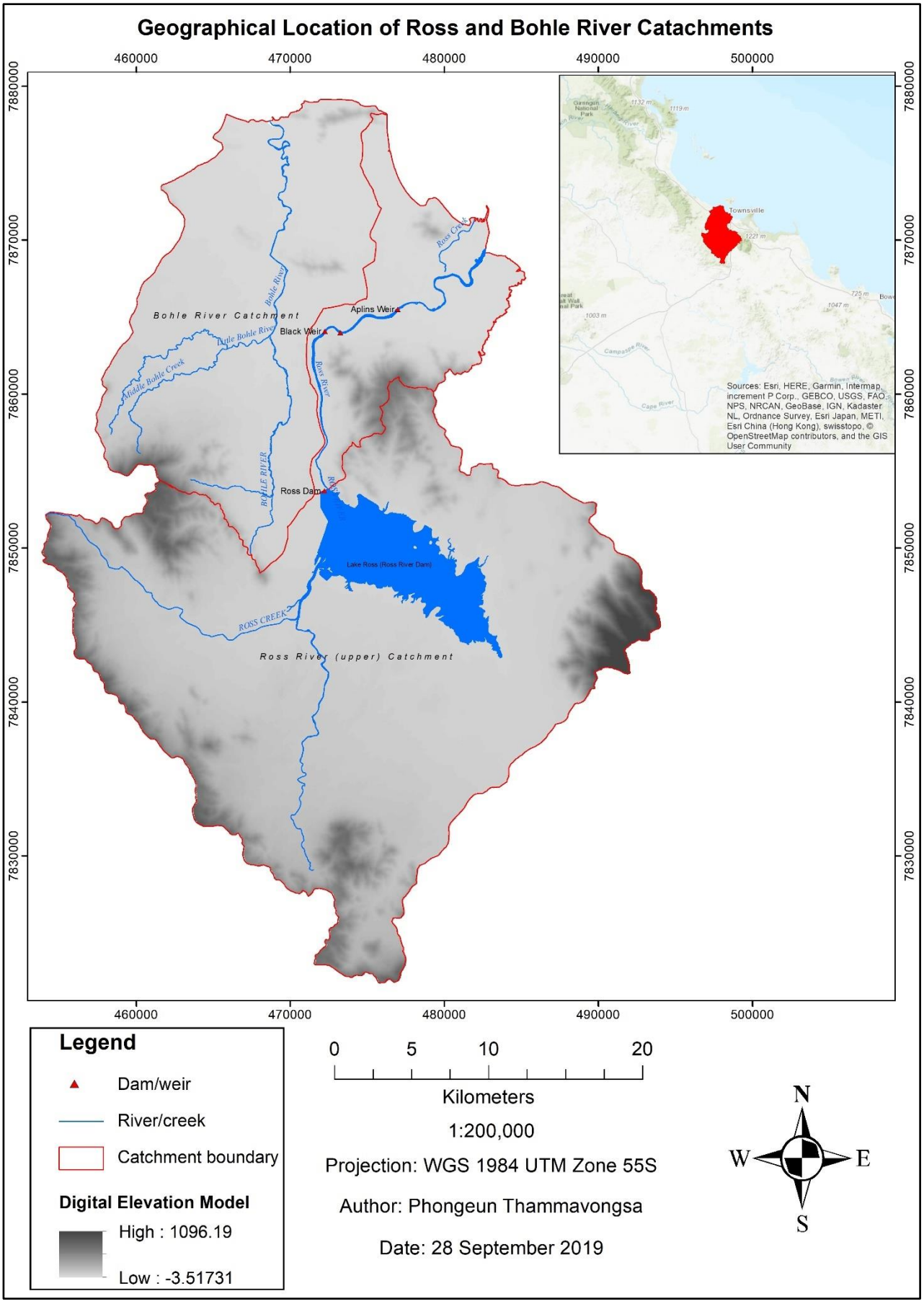

## Appendix B: Rainfall, temperature, and wind speed data at Townsville Aero Station (station number 032040)

| Date | Minimum temperature (DegreeC) | Maximum temperature (DegreeC) | Rainfall (mm) | Direction of maximum wind gust | Speed of maximum wind gust (km/h) | Time of maximum wind gust |
|---|---|---|---|---|---|---|
| 1/1/2019 | 22.7 | 32 | 1.8 | ENE | 48 | 12:36 |
| 1/2/2019 | 23.3 | 31.9 | 0 | ENE | 48 | 12:47 |
| 1/3/2019 | 22.6 | 32.9 | 0 | ENE | 33 | 16:43 |
| 1/4/2019 | 23.1 | 32.7 | 0 | ENE | 44 | 13:59 |
| 1/5/2019 | 23 | 31.8 | 0 | E | 31 | 9:49 |
| 1/6/2019 | 23.9 | 32.5 | 0 | NE | 41 | 15:08 |
| 1/7/2019 | 23.9 | 32.6 | 0 | ENE | 43 | 16:02 |
| 1/8/2019 | 23.9 | 33.8 | 0 | N | 31 | 13:14 |
| 1/9/2019 | 24.9 | 38.3 | 0 | SSW | 41 | 10:41 |
| 1/10/2019 | 24.6 | 29.5 | 12.2 | SE | 54 | 22:39 |
| 1/11/2019 | 25.4 | 31.4 | 4.2 | ENE | 41 | 8:09 |
| 1/12/2019 | 24.3 | 31.2 | 0.6 | ENE | 37 | 11:26 |
| 1/13/2019 | 22.3 | 32.4 | 0.2 | E | 46 | 12:51 |
| 1/14/2019 | 25.1 | 32.8 | 0 | ENE | 46 | 13:09 |
| 1/15/2019 | 25.3 | 31.6 | 0 | ENE | 44 | 16:02 |
| 1/16/2019 | 21.7 | 32.2 | 1.6 | ENE | 43 | 14:51 |
| 1/17/2019 | 24.5 | 31.4 | 0 | NE | 39 | 12:11 |
| 1/18/2019 | 24.9 | 31.4 | 0 | ENE | 43 | 12:00 |
| 1/19/2019 | 25.9 | 32.3 | 1 | ENE | 39 | 11:50 |
| 1/20/2019 | 22.9 | 32.4 | 0 | E | 52 | 13:21 |
| 1/21/2019 | 23.3 | 32.5 | 0 | E | 44 | 13:45 |
| 1/22/2019 | 23.8 | 32.5 | 1 | ENE | 46 | 15:25 |
| 1/23/2019 | 25.5 | 32 | 0 | E | 43 | 12:26 |
| 1/24/2019 | 25.4 | 32.8 | 0 | ENE | 43 | 14:32 |
| 1/25/2019 | 25.6 | 31 | 0 | ESE | 41 | 9:56 |
| 1/26/2019 | 25.7 | 31.4 | 0 | E | 48 | 15:44 |
| 1/27/2019 | 23.3 | 27.6 | 30 | ENE | 52 | 2:15 |
| 1/28/2019 | 24 | 26.7 | 51.6 | ESE | 72 | 3:04 |
| 1/29/2019 | 23.9 | 27.7 | 80 | ENE | 48 | 13:18 |
| 1/30/2019 | 24.1 | 27.1 | 108.6 | E | 61 | 10:33 |
| 1/31/2019 | 24.6 | 26.9 | 153 | ENE | 54 | 23:38 |
| 2/1/2019 | 24.4 | 26.5 | 216.4 | NE | 59 | 9:42 |
| 2/2/2019 | 24.6 | 25.3 | 141.8 | ESE | 63 | 23:20 |
| 2/3/2019 | 22.5 | 27.4 | 171.6 | ESE | 76 | 22:24 |
| 2/4/2019 | 22.8 | 26.9 | 181.4 | ESE | 59 | 2:48 |
| 2/5/2019 | 24.2 | 29.2 | 42.2 | ESE | 43 | 0:51 |
| 2/6/2019 | 24.8 | 29 | 110.4 | E | 54 | 9:45 |
| 2/7/2019 | 24 | 27.7 | 16.4 | SE | 44 | 16:11 |
| 2/8/2019 | 23 | 29 | 118 | SE | 39 | 1:47 |
| 2/9/2019 | 24.5 | 31.9 | 1 | SSE | 33 | 10:01 |
| 2/10/2019 | 24.7 | 34.1 | 0 | ESE | 26 | 21:55 |
| 2/11/2019 | 25.4 | 36.4 | 0 | ENE | 30 | 18:59 |
| 2/12/2019 | 25.2 | 37.6 | 0 | SSE | 35 | 13:53 |
| 2/13/2019 | 22.9 | 36.1 | 0 | NW | 26 | 16:07 |
| 2/14/2019 | 24.3 | 39.3 | 0 | ENE | 43 | 15:56 |
| 2/15/2019 | 27 | 31.9 | 0 | ENE | 39 | 13:51 |
| 2/16/2019 | 24.9 | 32.4 | 0 | NE | 35 | 11:52 |
| 2/17/2019 | 25.5 | 31.3 | 0 | NE | 31 | 14:07 |
| 2/18/2019 | 25.3 | 31.6 | 0.2 | NNE | 28 | 12:27 |
| 2/19/2019 | 27.1 | 34.4 | 0 | NE | 37 | 20:32 |
| 2/20/2019 | 26.3 | 40.3 | 0 | WSW | 39 | 14:17 |
| 2/21/2019 | 23.1 | 40.7 | 0 | S | 43 | 14:02 |
| 2/22/2019 | 24.2 | 33.6 | 0 | ENE | 39 | 13:03 |
| 2/23/2019 | 27 | 31.4 | 0 | E | 41 | 9:22 |
| 2/24/2019 | 23 | 30.7 | 7 | E | 48 | 4:50 |
| 2/25/2019 | 23.8 | 31.6 | 2.4 | E | 46 | 11:26 |
| 2/26/2019 | 22.4 | | 0.2 | | | |
| 2/27/2019 | 22.2 | 31.5 | | E | 52 | 19:21 |
| 2/28/2019 | 23.2 | 31.6 | 0 | ENE | 46 | 15:42 |

Source: (Bureau of Meteorology 2019c).

**Appendix C: Map of the occurrence of surface water derived from Water Observation from Space**

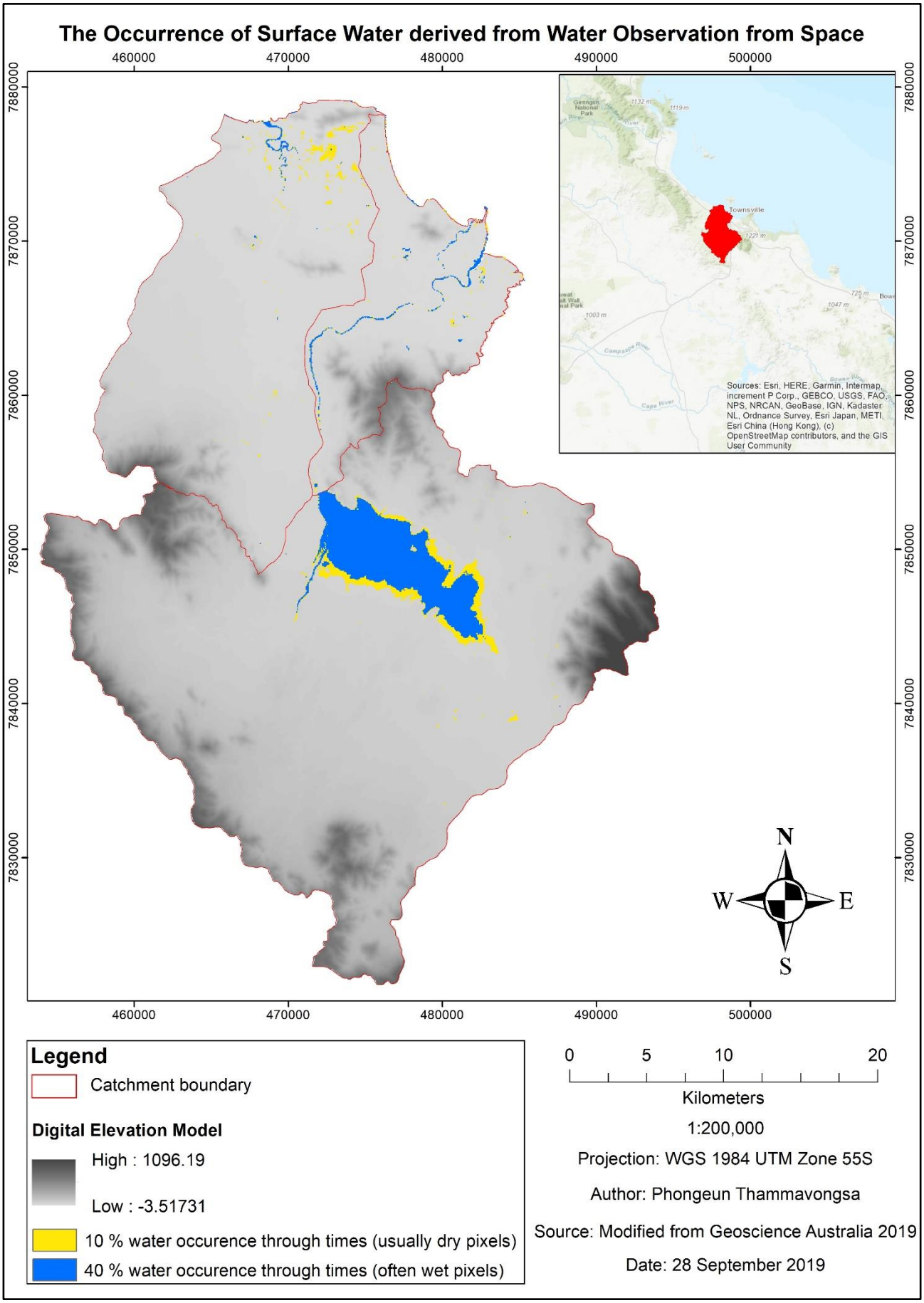

## Appendix D: Map of potentially inundated properties (Townsville)

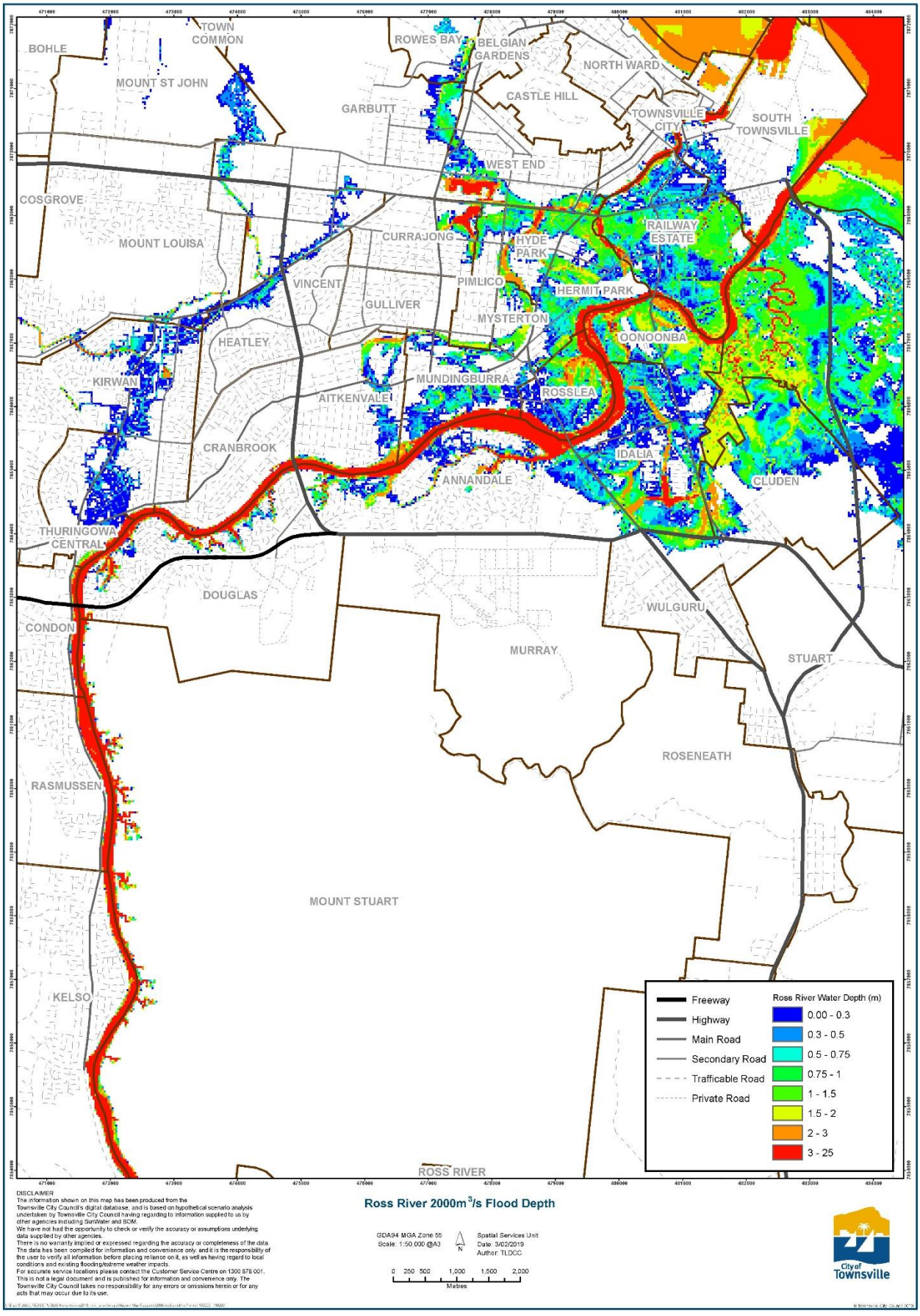


Source: (City of Townsville 2019c).

## Appendix E: Map of Ross River plan

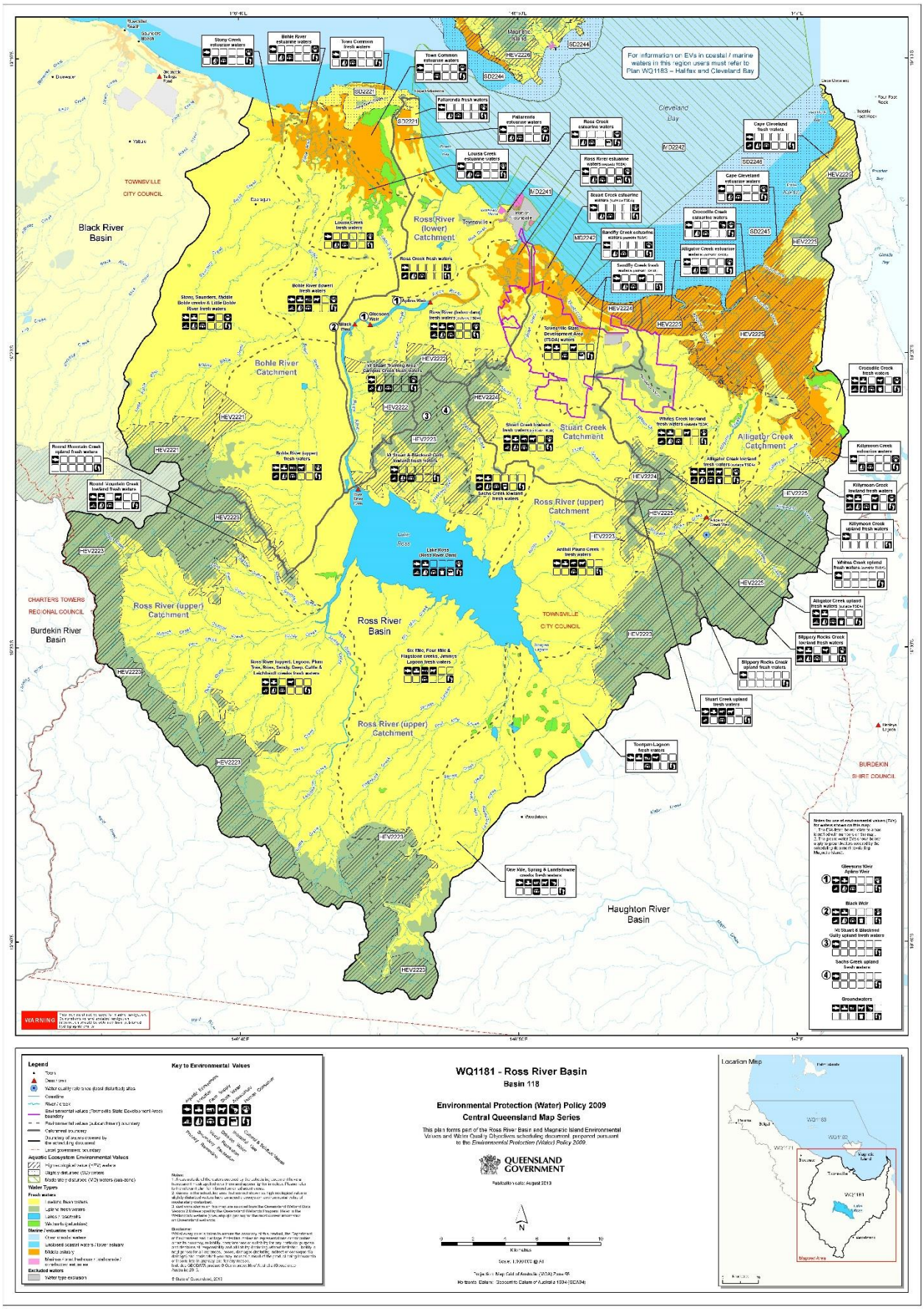


Source: Queensland Government 2013.

## Appendix F: Geometric correction for Sentinel 2 imagery derived on 25 November, 2018

| Points | Xi | Yi | Xr | Yr | Rx | Ry | RMSE |
|---|---|---|---|---|---|---|---|
| GCP1 | 465166.321 | 7848692.594 | 465166.808 | 7848694.766 | 0.487 | 2.172 | 2.226 |
| GCP2 | 484841.26 | 7844745.988 | 484840.752 | 7844743.352 | -0.508 | -2.636 | 2.684 |
| GCP3 | 468758.88 | 7870177.67 | 468761.806 | 7870180.075 | 2.926 | 2.405 | 3.788 |
| GCP4 | 482397.798 | 7870164.974 | 482396.581 | 7870161.844 | -1.217 | -3.13 | 3.358 |
| GCP5 | 485866.729 | 7859473.781 | 485868.082 | 7859475.32 | 1.353 | 1.539 | 2.049 |
| GCP6 | 468592.243 | 7859153.231 | 468593.383 | 7859143.22 | 1.14 | -10.011 | 10.076 |
| GCP7 | 479077.857 | 7852188.82 | 479077.883 | 7852193.595 | 0.026 | 4.775 | 4.775 |
| GCP8 | 471681.982 | 7856538.724 | 471682.489 | 7856537.784 | 0.507 | -0.94 | 1.068 |
| GCP9 | 479753.219 | 7856873.221 | 479752.121 | 7856872.686 | -1.098 | -0.535 | 1.222 |
| GCP10 | 474801.091 | 7869454.899 | 474801.035 | 7869456.191 | -0.056 | 1.292 | 1.294 |
| GCP11 | 474871.745 | 7870076.015 | 474871.598 | 7870076.322 | -0.147 | 0.307 | 0.341 |
| GCP12 | 475549.273 | 7869405.727 | 475549 | 7869406.033 | -0.273 | 0.306 | 0.41 |
| GCP13 | 477096.297 | 7869251.393 | 477095.687 | 7869251.854 | -0.61 | 0.461 | 0.765 |
| GCP14 | 477215.479 | 7869684.614 | 477214.734 | 7869685.226 | -0.745 | 0.612 | 0.964 |
| GCP15 | 472680.644 | 7864478.105 | 472681.302 | 7864477.35 | 0.658 | -0.755 | 1.001 |
| GCP16 | 483664.376 | 7862625.978 | 483664.458 | 7862625.156 | 0.082 | -0.822 | 0.826 |
| GCP17 | 482904.665 | 7859224.056 | 482905.12 | 7859226.223 | 0.455 | 2.167 | 2.214 |
| GCP18 | 467279.842 | 7862504.041 | 467277.15 | 7862509.051 | -2.692 | 5.01 | 5.687 |
| GCP19 | 474748.116 | 7868938.162 | 474750.665 | 7868937.229 | 2.549 | -0.933 | 2.715 |
| GCP20 | 478154.102 | 7868555.198 | 478153.969 | 7868555.178 | -0.133 | -0.02 | 0.135 |
| GCP21 | 477145.27 | 7868665.252 | 477145.207 | 7868665.288 | -0.063 | 0.036 | 0.072 |
| GCP22 | 478215.209 | 7869163.726 | 478215.086 | 7869163.728 | -0.123 | 0.002 | 0.123 |
| GCP23 | 468060.312 | 7867158.578 | 468057.793 | 7867157.277 | -2.519 | -1.301 | 2.835 |
| Average RMSE | | | | | | | 2.201217391 |

## Appendix G: Geometric correction for Sentinel 2 imagery derived on 13 February, 2019

| Points | Xi | Yi | Xr | Yr | Rx | Ry | RMSE |
|---|---|---|---|---|---|---|---|
| GCP1 | 465169.721 | 7848693.295 | 465171.314 | 7848692.33 | 1.593 | -0.965 | 1.862 |
| GCP2 | 484864.871 | 7844743.512 | 484862.767 | 7844743.075 | -2.104 | -0.437 | 2.149 |
| GCP3 | 468767.468 | 7870170.212 | 468765.174 | 7870170.912 | -2.294 | 0.7 | 2.398 |
| GCP4 | 482396.517 | 7870158.552 | 482394.221 | 7870166.339 | -2.296 | 7.787 | 8.118 |
| GCP5 | 485870.468 | 7859473.056 | 485871.655 | 7859473.931 | 1.187 | 0.875 | 1.475 |
| GCP6 | 468597.178 | 7859143.847 | 468598.122 | 7859141.559 | 0.944 | -2.288 | 2.475 |
| GCP7 | 479083.927 | 7852190.728 | 479083.761 | 7852192.634 | -0.166 | 1.906 | 1.913 |
| GCP8 | 471682.993 | 7856535.488 | 471678.994 | 7856538.419 | -3.999 | 2.931 | 4.959 |
| GCP9 | 479754.388 | 7856864.178 | 479761.888 | 7856864.235 | 7.5 | 0.057 | 7.5 |
| GCP10 | 472384.445 | 7871905.853 | 472386.772 | 7871905.356 | 2.327 | -0.497 | 2.38 |
| GCP11 | 474808.635 | 7869455.163 | 474812.527 | 7869456.143 | 3.892 | 0.98 | 4.014 |
| GCP12 | 474878.417 | 7870078.388 | 474878.666 | 7870075.67 | 0.249 | -2.718 | 2.729 |
| GCP13 | 475551.855 | 7869408.695 | 475556.74 | 7869409.339 | 4.885 | 0.644 | 4.927 |
| GCP14 | 477101.902 | 7869255.689 | 477100.677 | 7869256.728 | -1.225 | 1.039 | 1.606 |
| GCP15 | 477219.254 | 7869688.207 | 477217.075 | 7869691.56 | -2.179 | 3.353 | 3.998 |
| GCP16 | 472690.575 | 7864477.07 | 472679.942 | 7864482.123 | -10.633 | 5.053 | 11.773 |
| GCP17 | 483669.883 | 7862626.606 | 483666.933 | 7862623.883 | -2.95 | -2.723 | 4.015 |
| GCP18 | 482907.507 | 7859223.216 | 482910.318 | 7859221.804 | 2.811 | -1.412 | 3.145 |
| GCP19 | 467284.694 | 7862507.624 | 467284.53 | 7862505.875 | -0.164 | -1.749 | 1.757 |
| GCP20 | 474756.257 | 7868939.904 | 474759.749 | 7868939.599 | 3.492 | -0.305 | 3.505 |
| GCP21 | 478159.016 | 7868559.784 | 478155.547 | 7868558.181 | -3.469 | -1.603 | 3.821 |
| GCP22 | 477145.783 | 7868669.342 | 477148.586 | 7868664.939 | 2.803 | -4.403 | 5.219 |
| GCP23 | 478222.021 | 7869170.718 | 478219.771 | 7869162.05 | -2.25 | -8.668 | 8.955 |
| GCP24 | 468067.028 | 7867159.693 | 468069.072 | 7867162.136 | 2.044 | 2.443 | 3.186 |
| Average RMSE | | | | | | | 4.078291667 |

**Appendix H: Map of water extent in dry conditions (pre-flood) derived from Sentinel 2 images (26 October, 2018)**

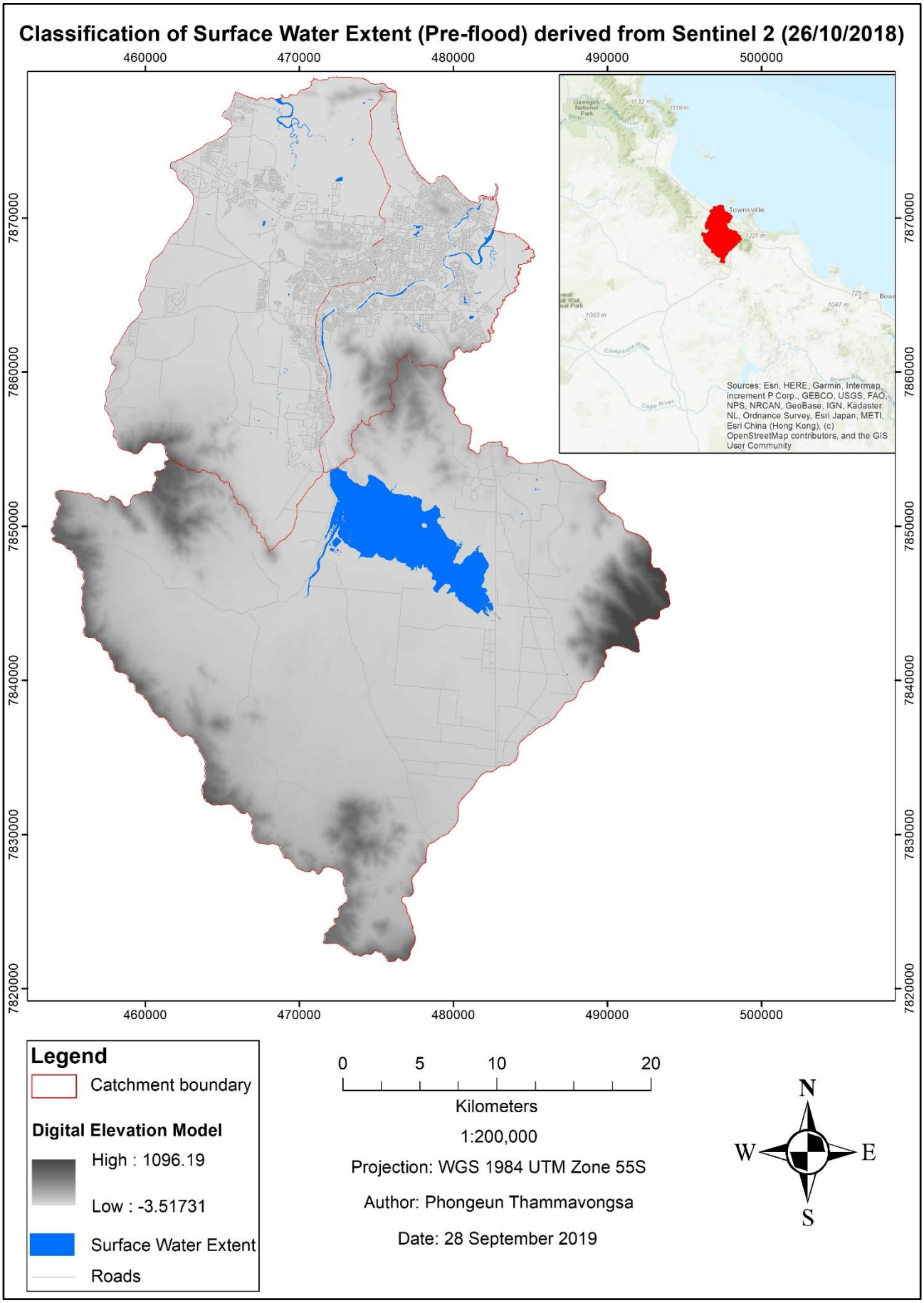

**Appendix I: Map of water extent in wet conditions (post flood) derived from Sentinel 2 image (13 February, 2019)**

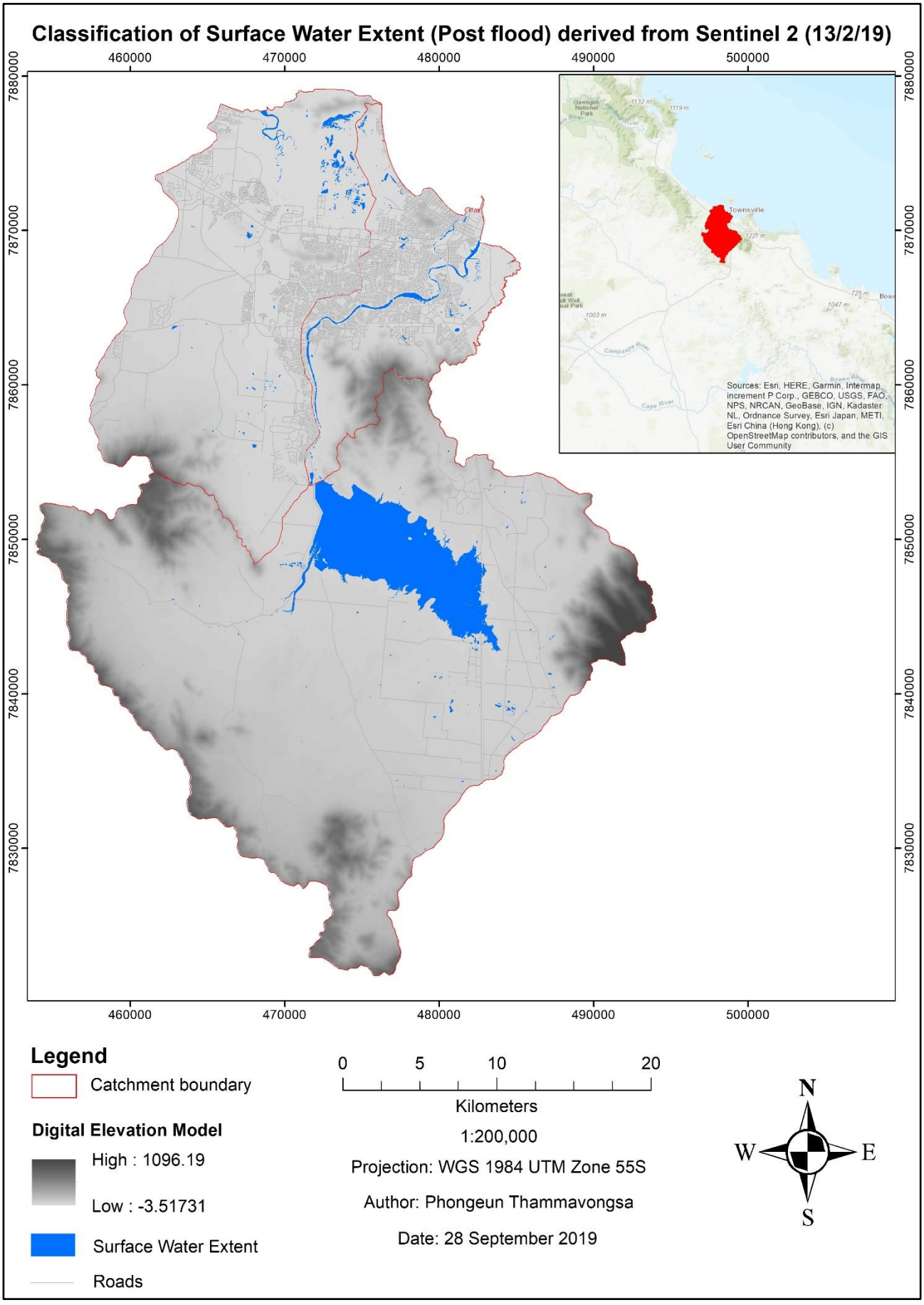

**Appendix J: Map of flood water extent (during flood) derived from Sentinel 1 image (31 January, 2019)**

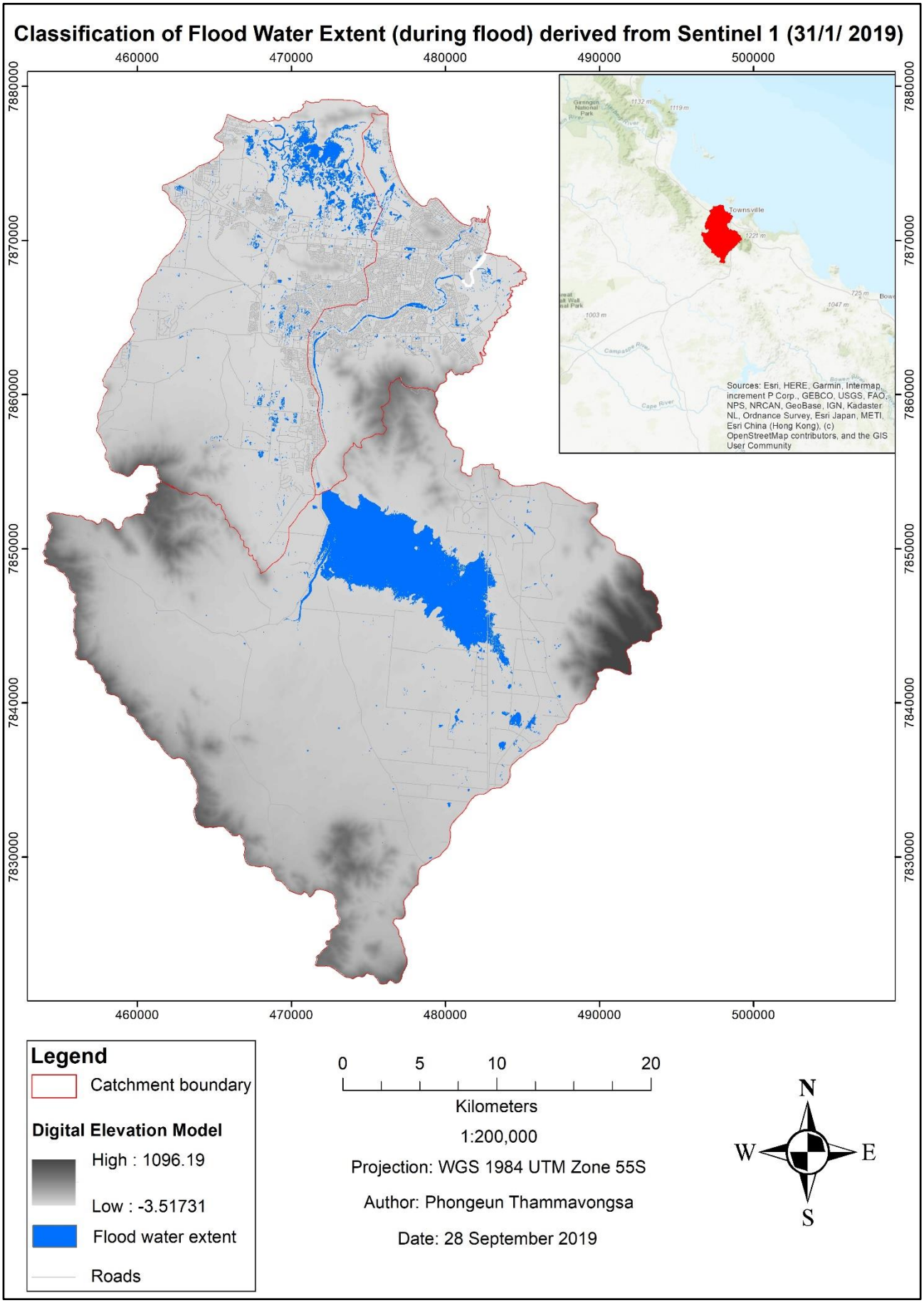

**Appendix K: Map of flood water extent (during flood) derived from Sentinel 1 image (at 5:44 A.M. on 06 February, 2019)**

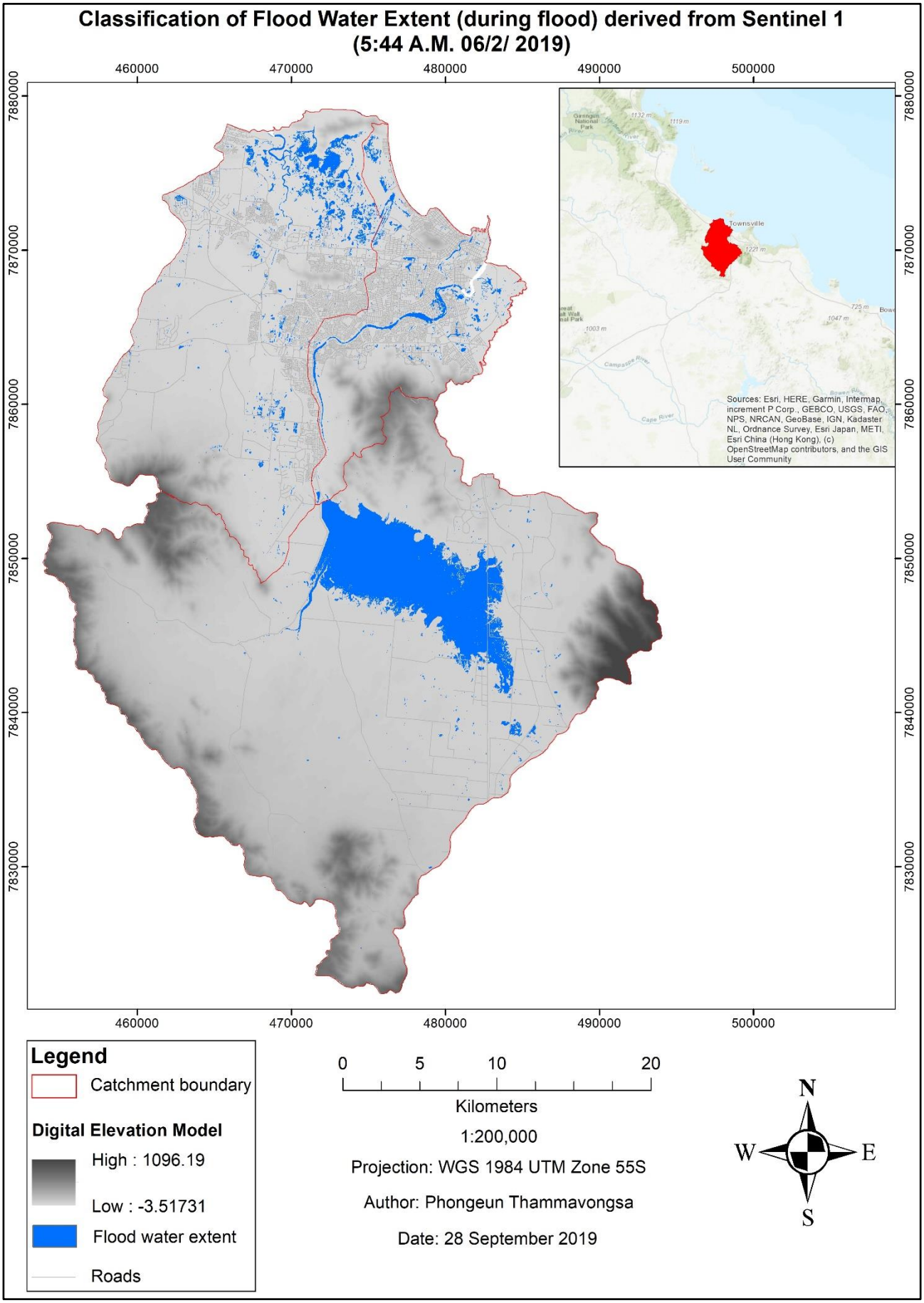

**Appendix L: Map of flood water extent (during flood) derived from Sentinel 1 image (at 18:43 P.M. on 06 February, 2019)**

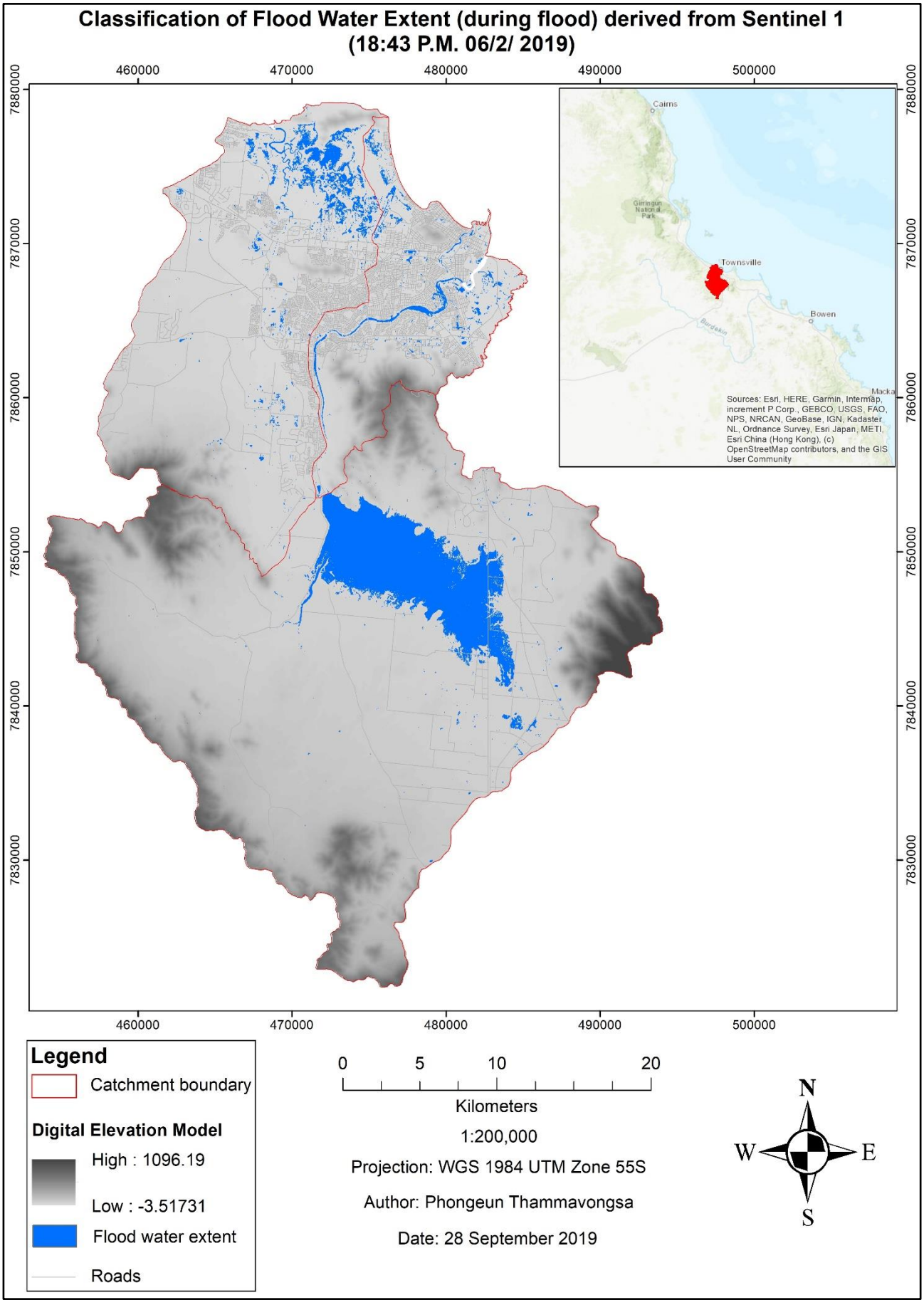

**Appendix M: Map of surface water extent (post flood) derived from Sentinel 1 image (at 5:44 A.M. on 12 February, 2019)**

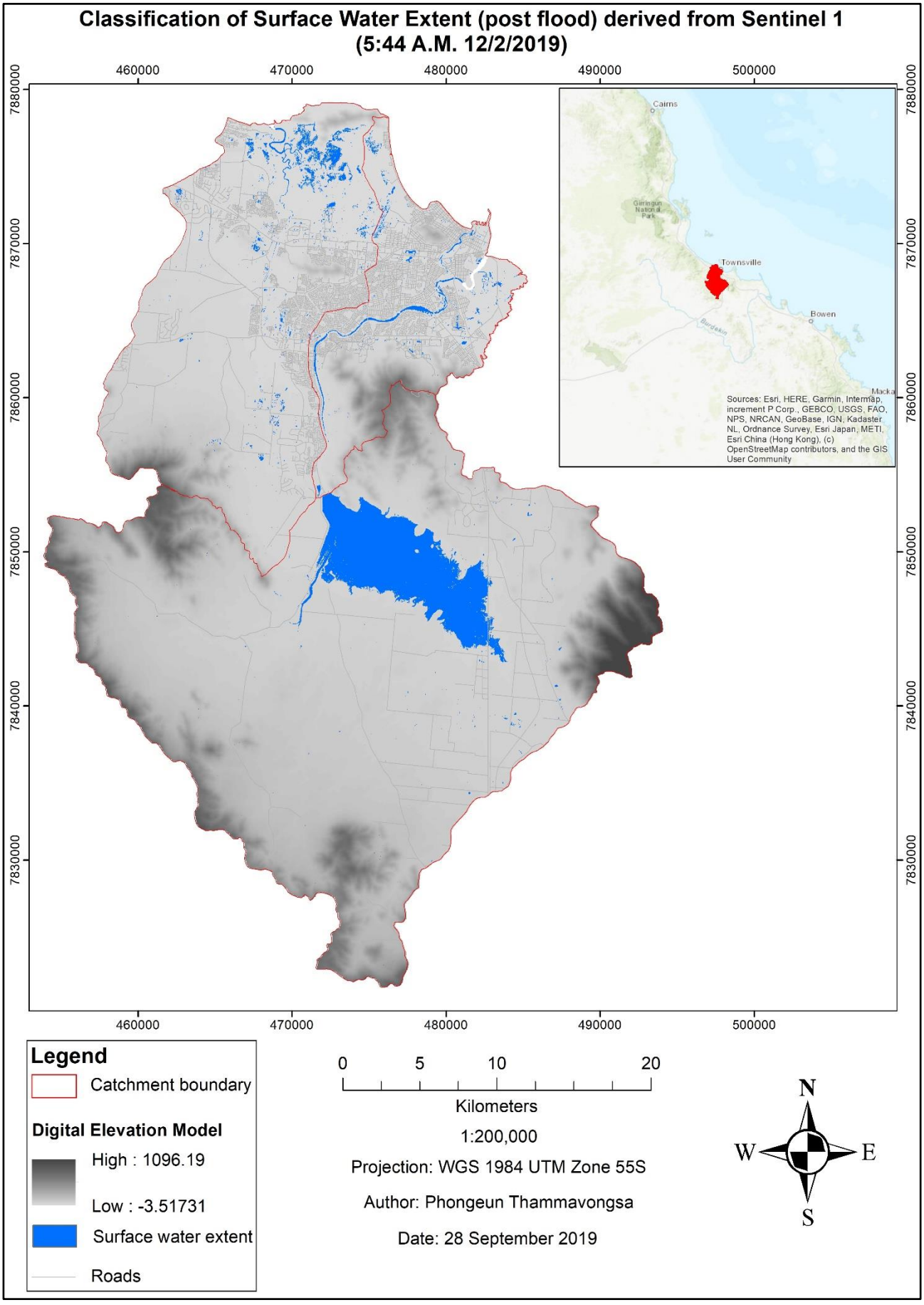

**Appendix N: Map of surface water extent (post flood) derived from Sentinel 1 image (at 18:42 P.M. on 12 February, 2019)**

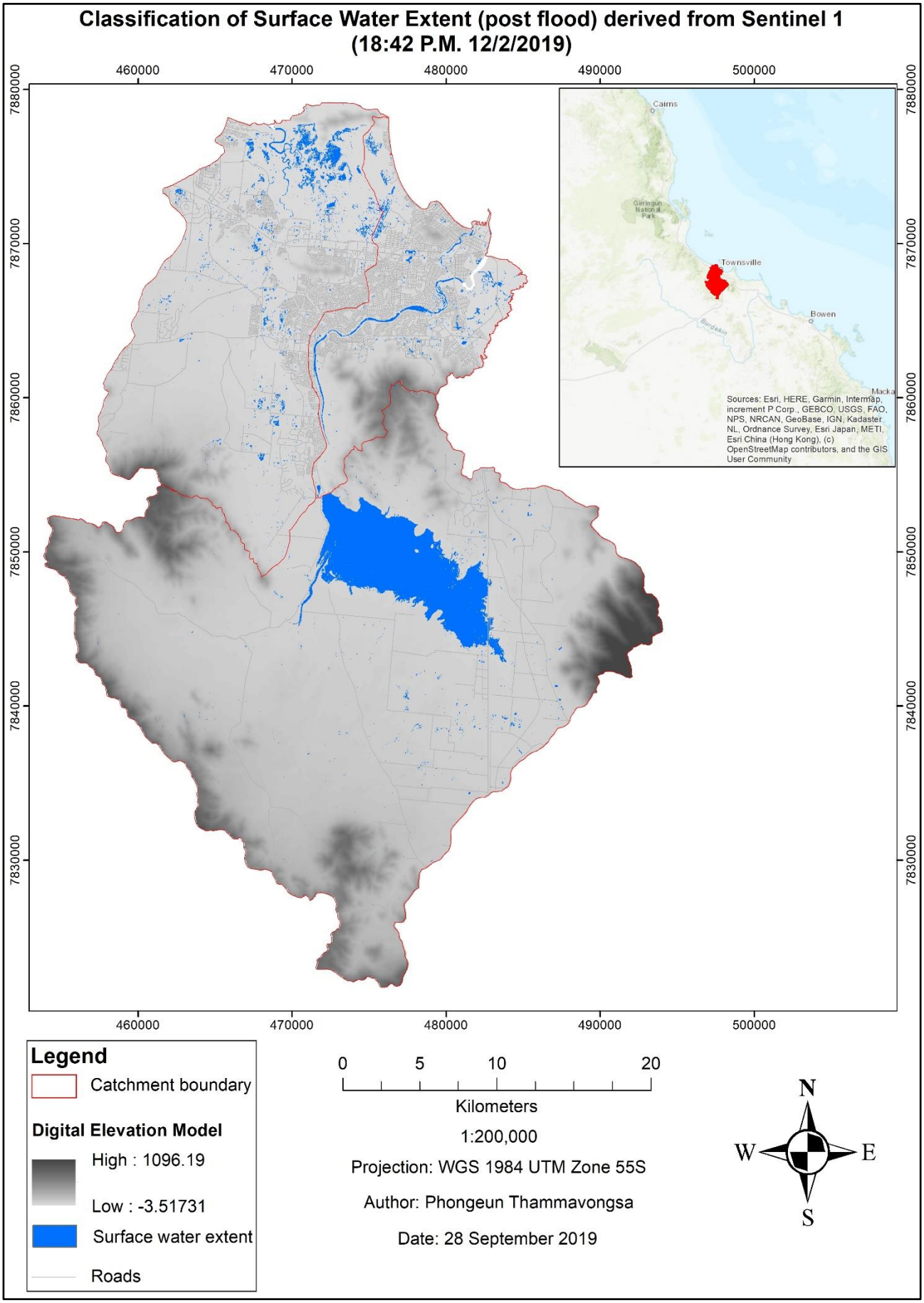

**Appendix O: Map of high spatial resolution of Aerial Base Imagery (derived from Google Earth Engine 2019)**

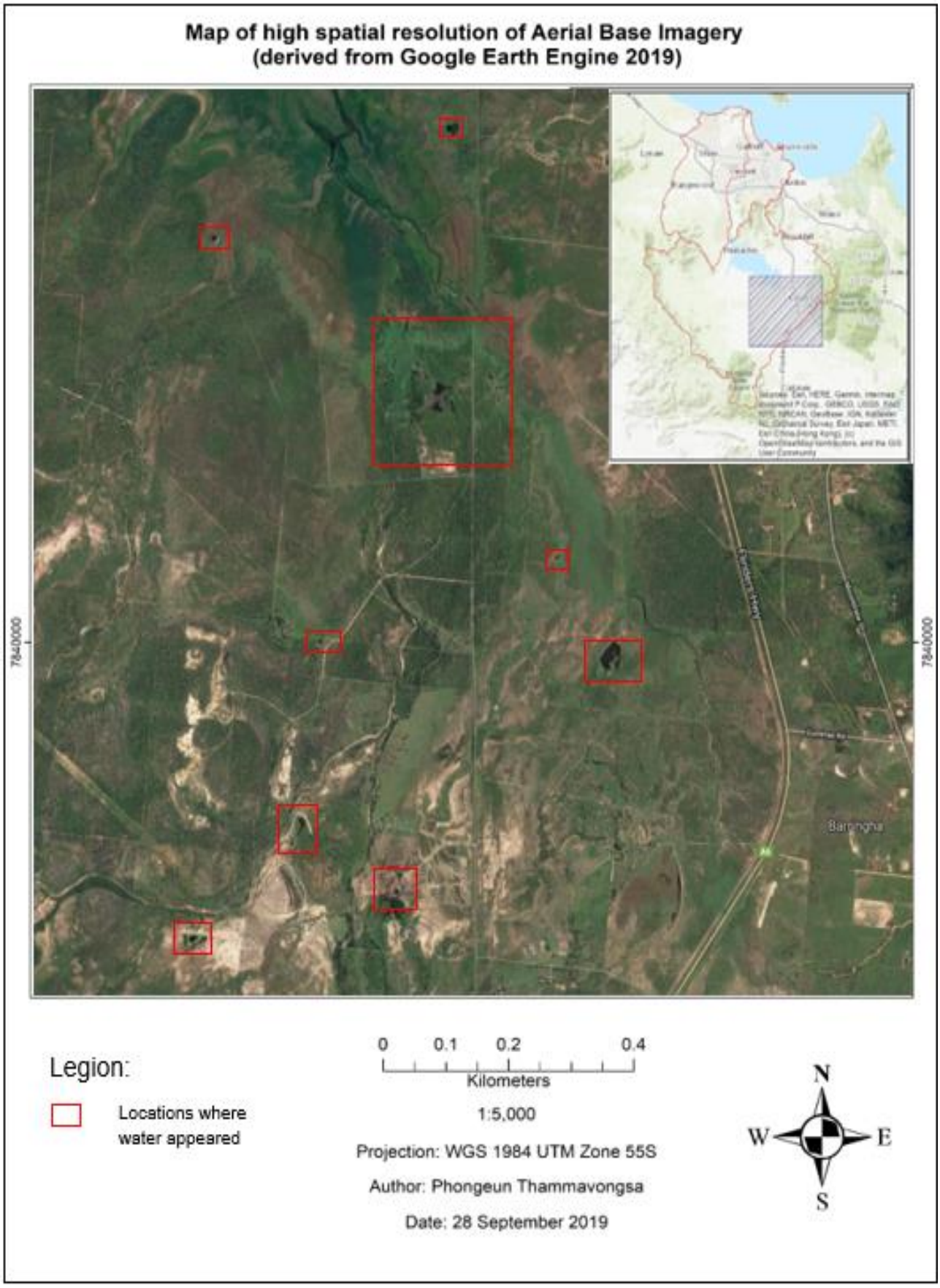

# REFERENCES


Abbaspour, KC, Yang, J, Maximov, I, Siber, R, Bogner, K, Mieleitner, J, Zobrist, J & Srinivasan, R 2007, 'Modelling hydrology and water quality in the pre-alpine/alpine Thur watershed using SWAT', *Journal of Hydrology*, vol. 333, no. 2-4, pp. 413-30.

ABC News 2019, *Townsville dam spillway gates open fully, with flood zone facing further inundation*, ABC News, viewed 2 May 2019, <https://www.abc.net.au/news/2019-02-03/townsville-flooding-catastrophe-dam-spillway-gates-fully-open/10774312>.

Adhikari Pradeep, Hong, Y, Douglas, KR, Kirschbaum, DB, Gourley, J, Adler, R & Brakenridge, GR 2010, 'A digitized global flood inventory (1998–2008): compilation and preliminary results', *Natural hazards*, vol. 55, no. 2, pp. 405-22.

Ali, G, Birkel, C, Tetzlaff, D, Soulsby, C, McDonnell, JJ & Tarolli, P 2014, 'A comparison of wetness indices for the prediction of observed connected saturated areas under contrasting conditions', *Earth Surface Processes and Landforms*, vol. 39, no. 3, pp. 399-413.

Alsdorf, DE, Rodríguez, E & Lettenmaier, DP 2007, 'Measuring surface water from space', *Reviews of Geophysics*, vol. 45, no. 2.

Anderson, JR 1976, *A land use and land cover classification system for use with remote sensor data*, vol. 964, US Government Printing Office.

Apan, A, Keogh, D, King, D, Thomas, M, Mushtaq, S & Baddiley, P 2010, 'The 2008 floods in Queensland: a case study of vulnerability, resilience and adaptive capacity'.

Ariza, A, Robredo Irizar, M & Bayer, S 2018, 'Empirical line model for the atmospheric correction of sentinel-2A MSI images in the Caribbean Islands', *European Journal of Remote Sensing*, vol. 51, no. 1, pp. 765-76.

Arnold, JG, Moriasi, DN, Gassman, PW, Abbaspour, KC, White, MJ, Srinivasan, R, Santhi, C, Harmel, R, Van Griensven, A & Van Liew, MW 2012, 'SWAT: Model use, calibration, and validation', *Transactions of the ASABE*, vol. 55, no. 4, pp. 1491-508.

Australian Bureau of Statistics 2019, *2016 community profile: Townsville*, Australian Bureau of Statistics, viewed 30 April 2019, <https://quickstats.censusdata.abs.gov.au/census_services/getproduct/census/2016/communityprofile/3016>.

Baghdadi, N, Bernier, M, Gauthier, R & Neeson, I 2001, 'Evaluation of C-band SAR data for wetlands mapping', *International Journal of Remote Sensing*, vol. 22, no. 1, pp. 71-88.

Baillarin, S, Meygret, A, Dechoz, C, Petrucci, B, Lacherade, S, Trémas, T, Isola, C, Martimort, P & Spoto, F 2012, 'Sentinel-2 level 1 products and image processing performances', in *2012 IEEE international geoscience and remote sensing symposium*, pp. 7003-6.

Bales, J & Wagner, C 2009, 'Sources of uncertainty in flood inundation maps', *Journal of Flood Risk Management*, vol. 2, no. 2, pp. 139-47.

Baraldi, A & Parmiggiani, F 1995, 'A refined Gamma MAP SAR speckle filter with improved geometrical adaptivity', *IEEE Transactions on Geoscience and Remote Sensing*, vol. 33, no. 5, pp. 1245-57.

Barneveld, H, Silander, J, Sane, M & Malnes, E 2008, 'Application of satellite data for improved flood forecasting and mapping', in *4th International Symposium on Flood Defence: Managing Flood Risk, Reliability and Vulnerability, Toronto, Ontario, Canada*, pp. 77-1.

Bates, PD 2012, 'Integrating remote sensing data with flood inundation models: how far have we got?', *Hydrological Processes*, vol. 26, no. 16, pp. 2515-21.

Beven, KJ & Kirkby, MJ 1979, 'A physically based, variable contributing area model of basin hydrology/Un modèle à base physique de zone d'appel variable de l'hydrologie du bassin versant', *Hydrological Sciences Journal*, vol. 24, no. 1, pp. 43-69.

Biggin, D 1996, 'A comparison of ERS-1 satellite radar and aerial photography for river flood mapping', *Water and Environment Journal*, vol. 10, no. 1, pp. 59-64.

Blacknell, D, Freeman, A, Quegan, S, Ward, IA, Finley, I, Oliver, CJ, White, RG & Wood, JW 1989, 'Geometric accuracy in airborne SAR images', *IEEE Transactions on Aerospace and Electronic Systems*, vol. 25, no. 2, pp. 241-58.

BMT 2019, *Independent review of Ross river flooding, February 2019*, 30 July 2019, <https://www.igem.qld.gov.au/reports-and-publications/reports/Documents/IGEM%20MTRF%20-%20BMT%20hydrology%20report%2012062019.pdf>.

Boettinger, J, Ramsey, R, Bodily, J, Cole, N, Kienast-Brown, S, Nield, S, Saunders, A & Stum, A 2008, 'Landsat spectral data for digital soil mapping', in *Digital soil mapping with limited data*, Springer, pp. 193-202.

Brisco, B, Short, N, Sanden, Jvd, Landry, R & Raymond, D 2009, 'A semi-automated tool for surface water mapping with RADARSAT-1', *Canadian Journal of Remote Sensing*, vol. 35, no. 4, pp. 336-44.

Brivio, P, Colombo, R, Maggi, M & Tomasoni, R 2002, 'Integration of remote sensing data and GIS for accurate mapping of flooded areas', *International Journal of Remote Sensing*, vol. 23, no. 3, pp. 429-41.

Brown, JD, Spencer, T & Moeller, I 2007, 'Modeling storm surge flooding of an urban area with particular reference to modeling uncertainties: A case study of Canvey Island, United Kingdom', *Water Resources Research*, vol. 43, no. 6.

Brunner, GW 2010, *HEC-RAS river analysis system user's manual version 4.1*, Davis CA.

Buffin-Bélanger, T, Biron, PM, Larocque, M, Demers, S, Olsen, T, Choné, G, Ouellet, M-A, Cloutier, C-A, Desjarlais, C & Eyquem, J 2015, 'Freedom space for rivers: An economically viable river management concept in a changing climate', *Geomorphology*, vol. 251, pp. 137-48.

Bureau of Meteorology 2019a, *Climate statistics for Australian locations*, viewed 3 May 2019, <http://www.bom.gov.au/climate/averages/tables/cw_032040.shtml>.

—— 2019b, *Special climate statement 69: an extended period of heavy rainfall and flooding in tropical Queensland*, Australian Government: Bureau of Meteorology, viewed 6 June 2019, <http://www.bom.gov.au/climate/current/statements/scs69.pdf>.

—— 2019c, *Townsville, Queensland January 2019 daily weather observations*, Australian Government: Bureau of Meteorology, viewed 10 May 2019, <http://www.bom.gov.au/climate/dwo/201901/html/IDCJDW4128.201901.shtml>.

Campbell, JB & Wynne, RH 2011, *Introduction to remote sensing*, Guilford Press.

Campos, JC, Sillero, N & Brito, JC 2012, 'Normalized difference water indexes have dissimilar performances in detecting seasonal and permanent water in the Sahara–Sahel transition zone', *Journal of Hydrology*, vol. 464, pp. 438-46.

Chatterjee, C, Förster, S & Bronstert, A 2008, 'Comparison of hydrodynamic models of different complexities to model floods with emergency storage areas', *Hydrological Processes: An International Journal*, vol. 22, no. 24, pp. 4695-709.

Chini, M, Pelich, R, Pulvirenti, L, Pierdicca, N, Hostache, R & Matgen, P 2019, 'Sentinel-1 InSAR Coherence to Detect Floodwater in Urban Areas: Houston and Hurricane Harvey as A Test Case', *Remote Sensing*, vol. 11, no. 2, p. 107.

City of Townsville 2019a, *Flood Mapping Service*, viewed 30 April 2019, <https://www.townsville.qld.gov.au/building-planning-and-projects/mapping-services/flood-mapping-service>.

—— 2019b, *Ross river flood study: base-line flooding assessment*, viewed 2 May 2019, <https://www.townsville.qld.gov.au/about-council/news-and-publications/reports-drawings-and-plans/engineering-reports>.

—— 2019c, *Map of potential inundated properties*, viewed 10 May 2019, <https://www.townsville.qld.gov.au/about-council/news-and-publications/media-releases/2019/february/map-of-potential-inundated-properties>.

—— 2019d, *Towsville floodplain management strategy community survey* viewed 16 May 2019, <https://www.townsville.qld.gov.au/__data/assets/pdf_file/0028/8857/CommunitySurvey_Report_v4_With-Appendices.pdf>.

Clement, M, Kilsby, C & Moore, P 2018, 'Multi-temporal synthetic aperture radar flood mapping using change detection', *Journal of Flood Risk Management*, vol. 11, no. 2, pp. 152-68.

Coates, L 1999, 'Flood fatalities in Australia, 1788-1996', *Australian Geographer*, vol. 30, no. 3, pp. 391-408.

CRED/UNISDR 2016, *Poverty and death: Disaster mortality 1996–2015*, Centre for Research on the Epidemiology of Disasters Brussels, <https://www.unisdr.org/we/inform/publications/50589>.

D'Oria, M, Mignosa, P & Tanda, MG 2015, 'An inverse method to estimate the flow through a levee breach', *Advances in water resources*, vol. 82, pp. 166-75.

Devia, GK, Ganasri, B & Dwarakish, G 2015, 'A review on hydrological models', *Aquatic Procedia*, vol. 4, pp. 1001-7.

Dhodhi, MK, Saghri, JA, Ahmad, I & Ul-Mustafa, R 1999, 'D-ISODATA: A distributed algorithm for unsupervised classification of remotely sensed data on network of workstations', *Journal of Parallel and Distributed Computing*, vol. 59, no. 2, pp. 280-301.

Dianderas, E, Rojas, K & Kemper, G 2014, 'Identification and cadastral registration of water bodies through multispectral image processing with multi-layer Perceptron Neural Network', in *2014 XIX Symposium on Image, Signal Processing and Artificial Vision*, pp. 1-5.

Doxaran, D, Froidefond, J-M, Lavender, S & Castaing, P 2002, 'Spectral signature of highly turbid waters: Application with SPOT data to quantify suspended particulate matter concentrations', *Remote Sensing of Environment*, vol. 81, no. 1, pp. 149-61.

Drusch, M, Del Bello, U, Carlier, S, Colin, O, Fernandez, V, Gascon, F, Hoersch, B, Isola, C, Laberinti, P & Martimort, P 2012, 'Sentinel-2: ESA's optical high-resolution mission for GMES operational services', *Remote Sensing of Environment*, vol. 120, pp. 25-36.

Du, Y, Zhang, Y, Ling, F, Wang, Q, Li, W & Li, X 2016, 'Water bodies' mapping from Sentinel-2 imagery with modified normalized difference water index at 10-m spatial resolution produced by sharpening the SWIR band', *Remote Sensing*, vol. 8, no. 4, p. 354.

Dutch, RS 2019, 'Space: Exploration, Environments and Earth', *Genesis*, vol. 1, pp. 1-10.

ERDAS 1999, 'ERDAS field guide: the spectral enhancement', no. fifth edition, pp. 163-8.

Few, R 2003, 'Flooding, vulnerability and coping strategies: local responses to a global threat', *Progress in Development Studies*, vol. 3, no. 1, pp. 43-58.

Feyisa, GL, Meilby, H, Fensholt, R & Proud, SR 2014, 'Automated Water Extraction Index: A new technique for surface water mapping using Landsat imagery', *Remote Sensing of Environment*, vol. 140, pp. 23-35.

Fisher, A, Flood, N & Danaher, T 2016, 'Comparing Landsat water index methods for automated water classification in eastern Australia', *Remote Sensing of Environment*, vol. 175, pp. 167-82.

Foody, GM 2002, 'Status of land cover classification accuracy assessment', *Remote Sensing of Environment*, vol. 80, no. 1, pp. 185-201.

Gascon, F, Bouzinac, C, Thépaut, O, Jung, M, Francesconi, B, Louis, J, Lonjou, V, Lafrance, B, Massera, S & Gaudel-Vacaresse, A 2017, 'Copernicus Sentinel-2A calibration and products validation status', *Remote Sensing*, vol. 9, no. 6, p. 584.

Gatti, A & Bertolini, A 2013, 'Sentinel-2 products specification document', *Available online (accessed February 23, 2015) https://earth. esa. int/documents/247904/685211/Sentinel-2+ Products+ Specification+ Document*.

Geoscience Australian 2019, *Water observation from space*, viewed 15 June 2019, <http://www.ga.gov.au/dea/products#wofs>.

Giordan, D, Notti, D, Villa, A, Zucca, F, Calò, F, Pepe, A, Dutto, F, Pari, P, Baldo, M & Allasia, P 2018, 'Low cost, multiscale and multi-sensor application for flooded area mapping', *Natural Hazards and Earth System Sciences*, vol. 18, no. 5, p. 1493.

Giustarini, L, Hostache, R, Matgen, P, Schumann, GJP, Bates, PD & Mason, DC 2013, 'A Change Detection Approach to Flood Mapping in Urban Areas Using TerraSAR-X', *IEEE Transactions on Geoscience and Remote Sensing*, vol. 51, no. 4, pp. 2417-30.

Godschalk, DR 2003, 'Urban hazard mitigation: creating resilient cities', *Natural hazards review*, vol. 4, no. 3, pp. 136-43.

Gonçalves, H, Gonçalves, JA & Corte-Real, L 2009, 'Measures for an objective evaluation of the geometric correction process quality', *IEEE Geoscience and Remote Sensing Letters*, vol. 6, no. 2, pp. 292-6.

Grimaldi, S, Li, Y, Pauwels, VR & Walker, JP 2016, 'Remote sensing-derived water extent and level to constrain hydraulic flood forecasting models: Opportunities and challenges', *Surveys in Geophysics*, vol. 37, no. 5, pp. 977-1034.

Hammond, MJ, Chen, AS, Djordjević, S, Butler, D & Mark, O 2015, 'Urban flood impact assessment: A state-of-the-art review', *Urban Water Journal*, vol. 12, no. 1, pp. 14-29.

Henry, JB, Chastanet, P, Fellah, K & Desnos, YL 2006, 'Envisat multi-polarized ASAR data for flood mapping', *International Journal of Remote Sensing*, vol. 27, no. 10, pp. 1921-9.

Horritt, M, Mason, D & Luckman, A 2001, 'Flood boundary delineation from synthetic aperture radar imagery using a statistical active contour model', *International Journal of Remote Sensing*, vol. 22, no. 13, pp. 2489-507.

Houser, PR, Shuttleworth, WJ, Famiglietti, JS, Gupta, HV, Syed, KH & Goodrich, DC 1998, 'Integration of soil moisture remote sensing and hydrologic modeling using data assimilation', *Water Resources Research*, vol. 34, no. 12, pp. 3405-20.

Ishikawa, H, Oku, Y, Kim, S, Takemi, T & Yoshino, J 2013, 'Estimation of a possible maximum flood event in the Tone River basin, Japan caused by a tropical cyclone', *Hydrological Processes*, vol. 27, no. 23, pp. 3292-300.

Jain, SK & Singh, VP 2003, *Water resources systems planning and management*, vol. 51, Elsevier.

Jamali, B, Löwe, R, Bach, PM, Urich, C, Arnbjerg-Nielsen, K & Deletic, A 2018, 'A rapid urban flood inundation and damage assessment model', *Journal of Hydrology*, vol. 564, pp. 1085-98.

Joseph, G 2005, *Fundamentals of remote sensing*, Universities Press.

Jung, Y & Merwade, V 2011, 'Uncertainty quantification in flood inundation mapping using generalized likelihood uncertainty estimate and sensitivity analysis', *Journal of Hydrologic Engineering*, vol. 17, no. 4, pp. 507-20.

Kauffeldt, A, Wetterhall, F, Pappenberger, F, Salamon, P & Thielen, J 2016, 'Technical review of large-scale hydrological models for implementation in operational flood forecasting schemes on continental level', *Environmental Modelling & Software*, vol. 75, pp. 68-76.

Khan, SI, Hong, Y, Wang, J, Yilmaz, KK, Gourley, JJ, Adler, RF, Brakenridge, GR, Policelli, F, Habib, S & Irwin, D 2011, 'Satellite remote sensing and hydrologic modeling for flood inundation mapping in Lake Victoria basin: Implications for hydrologic prediction in ungauged basins', *IEEE Transactions on Geoscience and Remote Sensing*, vol. 49, no. 1, pp. 85-95.

Kron, W 2005, 'Flood risk= hazard• values• vulnerability', *Water International*, vol. 30, no. 1, pp. 58-68.

Lee, J-S 1980, 'Digital image enhancement and noise filtering by use of local statistics', *IEEE Transactions on Pattern Analysis & Machine Intelligence*, no. 2, pp. 165-8.

Levy, JK, Hartmann, J, Li, KW, An, Y & Asgary, A 2007, 'Multi-criteria decision support systems for flood hazard mitigation and emergency response in urban watersheds 1', *JAWRA Journal of the American Water Resources Association*, vol. 43, no. 2, pp. 346-58.

Li, W, Du, Z, Ling, F, Zhou, D, Wang, H, Gui, Y, Sun, B & Zhang, X 2013, 'A comparison of land surface water mapping using the normalized difference water index from TM, ETM+ and ALI', *Remote Sensing*, vol. 5, no. 11, pp. 5530-49.

Liu, J, Xu, Z, Chen, F, Chen, F & Zhang, L 2019, 'Flood Hazard Mapping and Assessment on the Angkor World Heritage Site, Cambodia', *Remote Sensing*, vol. 11, no. 1, p. 98.

Long, S, Fatoyinbo, TE & Policelli, F 2014, 'Flood extent mapping for Namibia using change detection and thresholding with SAR', *Environmental Research Letters*, vol. 9, no. 3, p. 035002.

Loughlin, W 1991, 'Principal component analysis for alteration mapping', *Photogrammetric Engineering and Remote Sensing*, vol. 57, no. 9, pp. 1163-9.

Louis, J, Debaecker, V, Pflug, B, Main-Knorn, M, Bieniarz, J, Mueller-Wilm, U, Cadau, E & Gascon, F 2016, 'Sentinel-2 sen2cor: L2a processor for users', in *Proceedings of the Living Planet Symposium, Prague, Czech Republic*, pp. 9-13.

Loveland, TR & Dwyer, JL 2012, 'Landsat: Building a strong future', *Remote Sensing of Environment*, vol. 122, pp. 22-9.

Lu, D, Mausel, P, Brondizio, E & Moran, E 2004, 'Change detection techniques', *International Journal of Remote Sensing*, vol. 25, no. 12, pp. 2365-401.

Lu, D & Weng, Q 2007, 'A survey of image classification methods and techniques for improving classification performance', *International Journal of Remote Sensing*, vol. 28, no. 5, pp. 823-70.

Lu, S, Wu, B, Yan, N & Wang, H 2011, 'Water body mapping method with HJ-1A/B satellite imagery', *International Journal of Applied Earth Observation and Geoinformation*, vol. 13, no. 3, pp. 428-34.

Malenovský, Z, Rott, H, Cihlar, J, Schaepman, ME, García-Santos, G, Fernandes, R & Berger, M 2012, 'Sentinels for science: Potential of Sentinel-1,-2, and-3 missions for scientific observations of ocean, cryosphere, and land', *Remote Sensing of Environment*, vol. 120, pp. 91-101.

Markert, KN, Chishtie, F, Anderson, ER, Saah, D & Griffin, RE 2018, 'On the merging of optical and SAR satellite imagery for surface water mapping applications', *Results in Physics*, vol. 9, pp. 275-7.

Marti, C, Belen, Lopez-Martinez, C, Dolz-Ripolles, J & Bladè-Castellet, E 2010, 'ASAR polarimetric, multi-incidence angle and multitemporal characterization of Doñana wetlands for flood extent monitoring', *Remote Sensing of Environment*, vol. 114, no. 11, pp. 2802-15.

Martinis, S, Twele, A & Voigt, S 2009, 'Towards operational near real-time flood detection using a split-based automatic thresholding procedure on high resolution TerraSAR-X data', *Natural Hazards and Earth System Sciences*, vol. 9, no. 2, pp. 303-14.

Mason, D, Speck, R, Schumann, G, Neal, J & Bates, P 2008, 'Using TerraSAR-X data for improved urban flood model validation', in *Proceedings of the 3rd TerraSAR-X Science Team Meeting, DLR Oberpfaffenhofen, Germany*, pp. 25-6.

Matgen, P, Schumann, G, Henry, JB, Hoffmann, L & Pfister, L 2007, 'Integration of SAR-derived river inundation areas, high-precision topographic data and a river flow model toward near real-time flood management', *International Journal of Applied Earth Observations and Geoinformation*, vol. 9, no. 3, pp. 247-63.

Matthew, MW, Adler-Golden, SM, Berk, A, Felde, G, Anderson, GP, Gorodetzky, D, Paswaters, S & Shippert, M 2002, 'Atmospheric correction of spectral imagery: evaluation of the FLAASH algorithm with AVIRIS data', in *Applied Imagery Pattern Recognition Workshop, 2002. Proceedings.*, pp. 157-63.

McFeeters, SK 1996, 'The use of the Normalized Difference Water Index (NDWI) in the delineation of open water features', *International Journal of Remote Sensing*, vol. 17, no. 7, pp. 1425-32.

MIKE11, D 2015, 'A Modelling System for Rivers and Channels—Reference Manual', *DHI: Hørsholm, Denmark*.

Mishra, D, Narumalani, S, Rundquist, D & Lawson, M 2006, 'Benthic habitat mapping in tropical marine environments using QuickBird multispectral data', *Photogrammetric Engineering & Remote Sensing*, vol. 72, no. 9, pp. 1037-48.

Moradkhani, H & Sorooshian, S 2009, 'General review of rainfall-runoff modeling: model calibration, data assimilation, and uncertainty analysis', in *Hydrological modelling and the water cycle*, Springer, pp. 1-24.

Mueller, N, Lewis, A, Roberts, D, Ring, S, Melrose, R, Sixsmith, J, Lymburner, L, McIntyre, A, Tan, P & Curnow, S 2016, 'Water observations from space: Mapping surface water from 25 years of Landsat imagery across Australia', *Remote Sensing of Environment*, vol. 174, pp. 341-52.

Muinonen, E 2018, 'Optical data-driven multi-source forest inventory setups for boreal and tropical forests', *Dissertationes Forestales*, no. 256.

Müller-Wilm, U, Devignot, O & Pessiot, L 2016, *Sen2Cor Configuration and User Manual, Ref*, S2-PDGS-MPC-L2ASUM-V2. 3, Telespazio VEGA Deutschland GmbH: Darmstadt, Germany.

Muller, SJ 2017, 'Indirect soil salinity detection in irregated areas using earth observation methods', Stellenbosch: Stellenbosch University.

Musa, Z, Popescu, I & Mynett, A 2015, 'A review of applications of satellite SAR, optical, altimetry and DEM data for surface water modelling, mapping and parameter estimation', *Hydrology and Earth System Sciences*, vol. 19, no. 9, pp. 3755-69.

NASA 2019, *NASA-ISRO Synthetic Aperture Radar*, viewed 20 August 2019, <https://www.jpl.nasa.gov/missions/nasa-isro-synthetic-aperture-radar-nisar/>.

Nazeer, M, Nichol, JE & Yung, Y-K 2014, 'Evaluation of atmospheric correction models and Landsat surface reflectance product in an urban coastal environment', *International Journal of Remote Sensing*, vol. 35, no. 16, pp. 6271-91.

Notti, D, Giordan, D, Caló, F, Pepe, A, Zucca, F & Galve, J 2018, 'Potential and Limitations of Open Satellite Data for Flood Mapping', *Remote Sensing*, vol. 10, no. 11, p. 1673.

Ouled, S, Moslem, Hammami, I, Foucher, S & Lepage, R 2018, 'Flood extent mapping from time-series SAR images based on texture analysis and data fusion', *Remote Sensing*, vol. 10, no. 2, p. 237.

Patro, S, Chatterjee, C, Mohanty, S, Singh, R & Raghuwanshi, N 2009, 'Flood inundation modeling using MIKE FLOOD and remote sensing data', *Journal of the Indian Society of Remote Sensing*, vol. 37, no. 1, pp. 107-18.

Pearson, AJ & Pizzuto, J 2015, 'Bedload transport over run-of-river dams, Delaware, USA', *Geomorphology*, vol. 248, pp. 382-95.

Pekel, J-F, Cottam, A, Gorelick, N & Belward, AS 2016, 'High-resolution mapping of global surface water and its long-term changes', *Nature*, vol. 540, no. 7633, p. 418.

Pelling, M, Maskrey, A, Ruiz, P, Hall, P, Peduzzi, P, Dao, Q-H, Mouton, F, Herold, C & Kluser, S 2004, 'Reducing disaster risk: a challenge for development'.

Peña, F & Nardi, F 2018, 'Floodplain terrain analysis for coarse resolution 2D flood modeling', *Hydrology*, vol. 5, no. 4, p. 52.

Pierdicca, N, Pulvirenti, L & Chini, M 2018, 'Flood mapping in vegetated and urban areas and other challenges: models and methods', in *Flood Monitoring through Remote Sensing*, Springer, pp. 135-79.

Pourali, S, Arrowsmith, C, Chrisman, N, Matkan, A & Mitchell, D 2016, 'Topography wetness index application in flood-risk-based land use planning', *Applied Spatial Analysis and Policy*, vol. 9, no. 1, pp. 39-54.

Pun, T 1980, 'A new method for grey-level picture thresholding using the entropy of the histogram', *Signal processing*, vol. 2, no. 3, pp. 223-37.

Quirogaa, VM, Kurea, S, Udoa, K & Manoa, A 2016, 'Application of 2D numerical simulation for the analysis of the February 2014 Bolivian Amazonia flood: Application of the new HEC-RAS version 5', *Ribagua*, vol. 3, no. 1, pp. 25-33.

Raaijmakers, R, Krywkow, J & van der Veen, A 2008, 'Flood risk perceptions and spatial multi-criteria analysis: an exploratory research for hazard mitigation', *Natural hazards*, vol. 46, no. 3, pp. 307-22.

Rast, M, Johannessen, J & Mauser, W 2014, 'Review of understanding of Earth's hydrological cycle: Observations, theory and modelling', *Surveys in Geophysics*, vol. 35, no. 3, pp. 491-513.

Santos, JR, Freitas, CC, Araujo, LS, Dutra, LV, Mura, JC, Gama, FF, Soler, LS & Sant'Anna, SJ 2003, 'Airborne P-band SAR applied to the aboveground biomass studies in the Brazilian tropical rainforest', *Remote Sensing of Environment*, vol. 87, no. 4, pp. 482-93.

Schlaffer, S, Matgen, P, Hollaus, M & Wagner, W 2015, 'Flood detection from multi-temporal SAR data using harmonic analysis and change detection', *International Journal of Applied Earth Observation and Geoinformation*, vol. 38, pp. 15-24.

Schmugge, TJ, Kustas, WP, Ritchie, JC, Jackson, TJ & Rango, A 2002, 'Remote sensing in hydrology', *Advances in water resources*, vol. 25, no. 8-12, pp. 1367-85.

Schumann, G, Hostache, R, Puech, C, Hoffmann, L, Matgen, P, Pappenberger, F & Pfister, L 2007, 'High-resolution 3-D flood information from radar imagery for flood hazard management', *IEEE Transactions on Geoscience and Remote Sensing*, vol. 45, no. 6, pp. 1715-25.

Schumann, G, Neal, JC, Mason, DC & Bates, PD 2011, 'The accuracy of sequential aerial photography and SAR data for observing urban flood dynamics, a case study of the UK summer 2007 floods', *Remote Sensing of Environment*, vol. 115, no. 10, pp. 2536-46.

Shen, H, Perrie, W, He, Y & Liu, G 2013, 'Wind speed retrieval from VH dual-polarization RADARSAT-2 SAR images', *IEEE Transactions on Geoscience and Remote Sensing*, vol. 52, no. 9, pp. 5820-6.

Shi, W & Wang, M 2014, 'Ocean reflectance spectra at the red, near-infrared, and shortwave infrared from highly turbid waters: A study in the Bohai Sea, Yellow Sea, and East China Sea', *Limnology and Oceanography*, vol. 59, no. 2, pp. 427-44.

Small, D & Schubert, A 2008, 'Guide to ASAR geocoding', *ESA-ESRIN Technical Note RSL-ASAR-GC-AD*, vol. 1, p. 36.

Team, P 2018, 'Planet Imagery Product Specifications', *Planet Team: San Francisco, CA, USA*.

Teng, J, Jakeman, AJ, Vaze, J, Croke, BF, Dutta, D & Kim, S 2017, 'Flood inundation modelling: A review of methods, recent advances and uncertainty analysis', *Environmental Modelling & Software*, vol. 90, pp. 201-16.

Torres, R, Snoeij, P, Geudtner, D, Bibby, D, Davidson, M, Attema, E, Potin, P, Rommen, B, Floury, N & Brown, M 2012, 'GMES Sentinel-1 mission', *Remote Sensing of Environment*, vol. 120, pp. 9-24.

Toutin, T 2004, 'Geometric processing of remote sensing images: models, algorithms and methods', *International Journal of Remote Sensing*, vol. 25, no. 10, pp. 1893-924.

Townsville Bulletin 2019, *Townsville flood: decision made to release gated water, flooding Townsville suburbs*, Townsville Bulletin, viewed 30 April 2019, <https://www.townsvillebulletin.com.au/news/townsville/townsville-flood-decision-made-to-release-gated-water-flooding-townsville-suburbs/news-story/3c6971e82fa60770f5a6a3abfd430655>.

Tsyganskaya, V, Martinis, S, Marzahn, P & Ludwig, R 2018, 'SAR-based detection of flooded vegetation–a review of characteristics and approaches', *International Journal of Remote Sensing*, vol. 39, no. 8, pp. 2255-93.

Twele, A, Cao, W, Plank, S & Martinis, S 2016, 'Sentinel-1-based flood mapping: a fully automated processing chain', *International Journal of Remote Sensing*, vol. 37, no. 13, pp. 2990-3004.

Van Zyl, JJ, Zebker, HA & Elachi, C 1987, 'Imaging radar polarization signatures: Theory and observation', *Radio science*, vol. 22, no. 04, pp. 529-43.

Wang, J, Ge, Y, Heuvelink, GB, Zhou, C & Brus, D 2012, 'Effect of the sampling design of ground control points on the geometric correction of remotely sensed imagery', *International Journal of Applied Earth Observation and Geoinformation*, vol. 18, pp. 91-100.

Warren, I & Bach, HK 1992, 'MIKE 21: a modelling system for estuaries, coastal waters and seas', *Environmental Software*, vol. 7, no. 4, pp. 229-40.

Watson, RT, Zinyowera, MC, Moss, RH & Dokken, DJ 1998, 'The regional impacts of climate change', *IPCC, Geneva*.

Westerhoff, R, Kleuskens, M, Winsemius, H, Huizinga, H, Brakenridge, G & Bishop, C 2013, 'Automated global water mapping based on wide-swath orbital synthetic-aperture radar', *Hydrology & Earth System Sciences*, vol. 17, no. 1.

Wheater, H, Sorooshian, S & Sharma, KD 2007, *Hydrological modelling in arid and semi-arid areas*, Cambridge University Press.

Xie, H, Luo, X, Xu, X, Pan, H & Tong, X 2016, 'Automated subpixel surface water mapping from heterogeneous urban environments using Landsat 8 OLI imagery', *Remote Sensing*, vol. 8, no. 7, p. 584.

Xu, H 2006, 'Modification of normalised difference water index (NDWI) to enhance open water features in remotely sensed imagery', *International Journal of Remote Sensing*, vol. 27, no. 14, pp. 3025-33.

Xue, Y, Li, Y, Guang, J, Zhang, X & Guo, J 2008, 'Small satellite remote sensing and applications–history, current and future', *International Journal of Remote Sensing*, vol. 29, no. 15, pp. 4339-72.

Yang, X, Zhao, S, Qin, X, Zhao, N & Liang, L 2017, 'Mapping of urban surface water bodies from Sentinel-2 MSI imagery at 10 m resolution via NDWI-based image sharpening', *Remote Sensing*, vol. 9, no. 6, p. 596.

Yu, Z, Quiring, S, Bales, R, Doswell, C, Nkemdirim, L & Tchakerian, V 2015, 'HYDROLOGY, FLOODS AND DROUGHTS| Modeling and Prediction'.

Yusuf, FR, Santoso, KB, Ningam, MUL, Kamal, M & Wicaksono, P 2018, 'Evaluation of atmospheric correction models and Landsat surface reflectance product in Daerah Istimewa Yogyakarta, Indonesia', in *IOP Conference Series: Earth and Environmental Science*, vol. 169, p. 012004.

Zhou, X, Zeng, Q, Jiao, J, Wang, Q & Gao, S 2012, 'Geometric calibration and geolocation of airborne SAR images', in *2012 IEEE International Geoscience and Remote Sensing Symposium*, pp. 4513-6.

Zhu, Z, Oberg, N, Morales, VM, Quijano, JC, Landry, BJ & Garcia, MH 2016, 'Integrated urban hydrologic and hydraulic modelling in Chicago, Illinois', *Environmental Modelling & Software*, vol. 77, pp. 63-70.

Zhu, Z, Wang, S & Woodcock, CE 2015, 'Improvement and expansion of the Fmask algorithm: Cloud, cloud shadow, and snow detection for Landsats 4–7, 8, and Sentinel 2 images', *Remote Sensing of Environment*, vol. 159, pp. 269-77.